Review

OPEN ACCESS
International Journal of Modern Physics A
Vol. 37, No. 13 (2022) 2230004 (108 pages)

DOI: 10.1142/S0217751X22300046

World Scientific
www.worldscientific.com

Feasibility of crystal-assisted collimation in the CERN accelerator complex

W. Scandale,[2,5,*] G. Arduini,[1] R. Assmann,[1] C. Bracco,[1] M. Butcher,[1] F. Cerutti,[1] M. D'Andrea,[1] L. S. Esposito,[1] M. Garattini,[1] S. Gilardoni,[1] E. Laface,[1] L. Lari,[1] R. Losito,[1] A. Masi,[1] E. Metral,[1] D. Mirarchi,[1] S. Montesano,[1] S. Petrucci,[1] V. Previtali,[1] S. Redaelli,[1] R. Rossi,[1,†] P. Schoofs,[1] M. Silari,[1] L. Tlustos,[1] L. Burmistrov,[3] A. Natochii,[1,3,‡] S. Dubos,[3] V. Puill,[3] A. Stocchi,[3] E. Bagli,[7] L. Bandiera,[7] E. Baricordi,[7] P. Dalpiaz,[7] M. Fiorini,[7] V. Guidi,[7] A. Mazzolari,[7] D. Vincenzi,[7] F. Addesa,[1,5] G. Cavoto,[5] F. Iacoangeli,[5] L. Ludovici,[5] R. Santacesaria,[5] P. Valente,[5] F. Galluccio,[6] E. Vallazza,[8] D. Bolognini,[10,11] L. Foggetta,[10,11] S. Hasan,[10,11] D. Lietti,[10,11] V. Mascagna,[10,11] A. Mattera,[10,11] M. Prest,[10,11] G. Ambrosi,[12] P. Azzarello,[12] B. Bertucci,[12] M. Ionica,[12] R. Battiston,[13,14] P. Zuccon,[13,14] W. J. Burger,[15,16] A. Carnera,[9] G. Della Mea,[9] A. Lombardi,[9] D. De Salvador,[9] R. Milan,[9] A. Vomiero,[9] G. Claps,[4] S. Dabagov,[4] F. Murtas,[1,4] A. D. Kovalenko,[17] A. M. Taratin,[17] V. V. Uzhinskiy,[17] G. I. Smirnov,[1,17] A. S. Denisov,[18] Yu. A. Gavrikov,[18] Yu. M. Ivanov,[18] L. P. Lapina,[18] L. G. Malyarenko,[18] V. V. Skorobogatov,[18] V. M. Suvorov,[18] S. A. Vavilov,[18] A. G. Afonin,[19] Yu. A. Chesnokov,[19] A. A. Durum,[19] V. A. Maisheev,[19] Yu. E. Sandomirskij,[19] A. A. Yanovich,[19] I. A. Yazynin,[19] T. Markiewicz,[21] M. Oriunno,[21] U. Wienands,[22] N. Mokhov,[20] D. Still,[20] G. Auzinger,[2] J. Borg,[2] W. Ferguson,[2] J. Fulcher,[2] T. James,[2] G. Hall,[2] M. Pesaresi,[2] M. Raymond,[2] A. Rose,[2] M. Ryan,[2] and O. Zorba[2]
(The UA9 Collaboration)

[1]*CERN, European Organization for Nuclear Research, CH-1211 Geneva 23, Switzerland*
[2]*Imperial College, London, UK*
[3]*Laboratoire de l'Accélerateur Linéaire (LAL), Université Paris-Sud, Orsay, France*
[4]*INFN, Laboratori Nazionali di Frascati, Via Fermi, 40 00044 Frascati (Roma), Italy*
[5]*INFN Sezione di Roma, Piazzale Aldo Moro 2, 00185 Rome, Italy*
[6]*INFN Sezione di Napoli, Complesso Universitario di Monte Sant'Angelo, Via Cintia, 80126 Napoli, Italy*
[7]*INFN Sezione di Ferrara and Dipartimento di Fisica e Scienze della Terra, Università di Ferrara, Via Saragat 1 Blocco C, 44121 Ferrara, Italy*
[8]*INFN Sezione di Trieste, Via Valerio 2, 34127 Trieste, Italy*
[9]*INFN Laboratori Nazionali di Legnaro, Viale Università 2, 35020 Legnaro (PD), Italy*
[10]*Università dell'Insubria, Via Valleggio 11, 22100 Como, Italy*
[11]*INFN sezione di Milano Bicocca, Piazza della Scienza 3, 20128 Milano, Italy*

*,†Corresponding authors.
‡On leave from Taras Shevchenko National University of Kyiv, 60 Volodymyrska Street, 01033 Kyiv, Ukraine.

[12] *INFN Sezione di Perugia and Università degli Studi di Perugia, Dipartimento di Fisica, Via Pascoli, 06123 Perugia, Italy*
[13] *Dipartimento di Fisica, Università di Trento, Via Sommarive 14, 38123 Povo, Italy*
[14] *INFN-TIFPA, Via Sommarive 14, 38123 Povo, Italy*
[15] *Centro Ricerche Enrico Fermi, Via Panisperna 89A 00184 Roma, Italy*
[16] *INFN-TIFPA, Via Sommarive 14, 38123 Trento, Italy*
[17] *Joint Institute for Nuclear Research, Joliot-Curie 6, 141980 Dubna, Russia*
[18] *Petersburg Nuclear Physics Institute in National Research Centre "Kurchatov Institute", 188300 Gatchina, Russia*
[19] *Institute for High Energy Physics (IHEP), National Research Centre Kurchatov Institute, Protvino, Moscow region, 142281 Russia*
[20] *Fermi National Accelerator Laboratory, P.O. Box 0500, Batavia, Il 60510-0500, USA*
[21] *SLAC National Accelerator Laboratory, 2575 Sand Hill Road, Menlo Park, CA 94025, USA*
[22] *Argonne National Laboratory, 9700 S Cass Ave, Lemont, IL 60439, USA*
* *walter.scandale@cern.ch*
† *roberto.rossi@cern.ch*

Received 22 November 2021
Accepted 27 February 2022
Accepted 15 March 2022
Published 27 May 2022

Bent silicon crystals mounted on high-accuracy angular actuators were installed in the CERN Super Proton Synchrotron (SPS) and extensively tested to assess the feasibility of crystal-assisted collimation in circular hadron colliders. The adopted layout was exploited and regularly upgraded for about a decade by the UA9 Collaboration. The investigations provided the compelling evidence of a strong reduction of beam losses induced by nuclear inelastic interactions in the aligned crystals in comparison with amorphous orientation. A conceptually similar device, installed in the betatron cleaning insertion of CERN Large Hadron Collider (LHC), was operated through the complete acceleration and storage cycle and demonstrated a large reduction of the background leaking from the collimation region and radiated into the cold sections of the accelerator and the experimental detectors. The implemented layout and the relevant results of the beam tests performed in the SPS and in the LHC with stored proton and ion beams are extensively discussed.

Keywords: Charged particle channeling; bent crystal; crystal-assisted collimation.

PACS numbers: 41.85.Si, 61.85.+p, 29.20.db, 29.27.−a, 41.75.Lx

Contents

1. Introduction

Sophisticated collimation systems are installed in high-energy high-intensity hadron colliders to safely intercept beam halo, to reduce background in experimental detectors and to minimize risk of damaging magnets by an excessive energy deposit into their superconducting coils. Channeling of high-energy particles in bent crystals, discovered by Tsyganov,[1] can be exploited to assist collimation and possibly improve its efficiency. A bent crystal inserted in the beam periphery, properly oriented

to capture a fraction of the halo particles in planar channeling states, imparts to the trajectory of channeled particles a deflection equal to its bending angle θ_b. Two aspects of such process are of particular interest for collimation.[2] The angle θ_b can be much larger than that imparted by multiple Coulomb scattering (MCS) in repeated passages of halo particles through an amorphous primary scatterer, hence the channeled halo should encounter the secondary absorber at much larger impact parameter and angle and be more effectively intercepted. Moreover, nuclear interaction and diffractive scattering probability, particularly low for particles in channeling states, should result in considerably less intense background flux eventually escaping from cleaning area.[3,4]

Channeling in a bent crystal is discussed in Refs. 5–7. The angular acceptance for channeling is proportional to the critical angle $\theta_c = \sqrt{2U_{max}/pv}$, where U_{max} is the potential well between two crystalline planes (~ 20 eV for Si (110) planes), p and v are the particle momentum and velocity respectively. With the increase of beam energy E the critical angle reduces as $\theta_c \propto E^{-1/2}$. To orient the crystal an angular actuator of adequate accuracy is required for application with high beam energy.

Attempts to demonstrate feasibility of crystal-assisted collimation in circular accelerators were first performed at RHIC at BNL[8–10] and later at the Tevatron at FNAL, using the T980 experimental setup.[11,12] Although significant, the results were not conclusive. At RHIC, the shape of betatron functions measured in the collimation insertion was considerably different from the nominal one. Because of this, the interplay of the synchro-betatron oscillations at the crystal entrance produced an excessive variation of the impact angle with two adverse consequences. The crystal acceptance for channeling was considerably reduced, while the trajectories of the deflected particles in channeling states could never be properly directed onto the secondary absorber. At the Tevatron, the accuracy of angular actuator was insufficient to obtain, in a reproducible manner, the channeling efficiency and the steering accuracy required to efficiently deflect the halo onto the secondary absorber. Neither the improvement of the angular actuator nor the replacement of the crystal by a new generation of multi-strip ones, insufficiently investigated at that time,[13,14] could provide any efficient collimation scenario.

Crystal-based extraction is another relevant field of investigation very similar to crystal-assisted collimation, in which halo-beam channeled in a bent crystal is deflected toward the extraction channel of a circular accelerator. In the RD22 program, proton beams of 120 GeV were extracted from the SPS using 3 cm long crystal with bending angle $\theta_b = 8.1$ mrad, by which, at that time, the record extraction efficiency of about 10% was obtained.[15] Moreover, the multi-turn extraction mechanism, by which particles not in channeling states at the first impact on the crystal could be eventually channeled and deflected in successive crystal encounters, was observed for the first time.[16] At the Tevatron, crystal-assisted extraction was obtained and its compatibility with the collider operation demonstrated in the E853 experiment.[17,18] The strongly nonlinear beam–beam interaction

resulting from the high-luminosity proton–antiproton collisions produced fast diffusion of large-emittance particles onto the oriented bent crystal and continuously sustained their controlled extraction into the magnetic channel dedicated to beam dump.[19] Extraction assisted by a short crystal of 2 mm length[20] was investigated in U70 synchrotron at IHEP-Protvino, using 70 GeV beams of 10^{12} protons. An extraction efficiency exceeding 85% was recorded in pulsed mode operation for a spill of 2 s length.[21,22]

In this paper, the feasibility of crystal-assisted collimation in the CERN accelerator complex is revisited, the key technological aspects are recalled and the main experimental results recorded in the SPS[23–28] and in LHC[29] are summarized.

2. Crystals for the SPS and the LHC

The crystals selected for collimation studies at CERN are at the forefront of present technology. Their features, resulting from three decades of research and development at PNPI-Gatchina, IHEP-Protvino and INFN-Ferrara, are summarized in App. A.

2.1. *Crystal test and characterization*

The UA9 Collaboration deployed a large effort in investigating interactions of high-energy particles with bent crystals, exploiting micro-beams of small dimension and ultra-low divergence, produced in the H8 beam line of the SPS North Area. An exhaustive overview of the studies, performed with various species of particles at different beam energies, is reported in Ref. 30. The conceptual detector setup was essentially made of three elements: a high-resolution angular actuator on which the crystal and its holder were mounted and oriented, a two-arm telescope to identify the particle trajectories upstream and downstream the crystal and a trigger to activate the front-end electronics at the passage of each particle.

Two different detectors were implemented one after the other and exploited to perform crystal studies in H8. The first one, more than 70 m long, fully asymmetric with respect to the crystal location, was making use of a telescope with short incoming arm to define the particle impact point on the crystal, and very long outgoing arm, of about 65 m, for the precise determination of the particle direction after the interaction with the crystal.[31] A position-sensitive gas chamber located at the end of the outgoing arm, about 70 m downstream the crystal, was utilized for the fast identification of the optimal channeling orientation with the highest possible beam intensity, up to 10^7 particles per pulse. The setup configuration was repeatedly changed over the couple of years of its exploitation, as reported in Ref. 32. In particular, more symmetrical telescope arms were implemented and double-sided sensors introduced instead of single-sided ones of the initial configuration, to improve and extend the identification of incoming and outgoing particle trajectories in 2D, at the cost of increasing the MCS perturbation due to the sensor traversal.

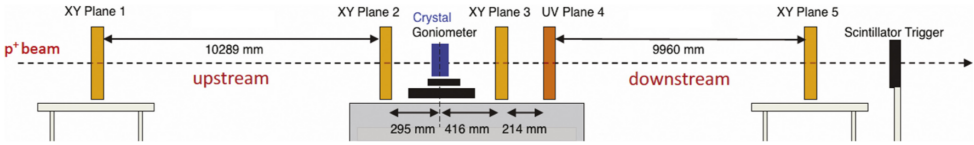

Fig. 1. Schematic overview of the UA9 setup in the H8 line of the SPS North Area.

The second setup, twice as fast as the previous one, was more compact and symmetric for a more balanced determination of incoming and outgoing particle trajectory. Moreover, it contained a redundant number of sensors for a more efficient identification of single particle events and rejection of spurious multi-tracks, and for a more reliable reconstruction of outgoing trajectories.[33] In use for the last decade with the stable configuration schematically shown in Fig. 1, such setup was also exploited to systematically test and characterize all crystals installed in SPS and LHC for crystal-assisted collimation.[34,35]

The charged particle telescope was optimized for data taking at high rates of crystal-proton interactions at 400 GeV. Ten planes of silicon microstrip sensors were arranged as five contiguous pairs, each measuring two orthogonal coordinates, over an active area of 3.8×3.8 cm^2. The telescope was approximately 10 m long in each arm, to provide excellent angular and spatial resolution for measuring the trajectories of incident and outgoing particles, while keeping electronics interconnections sufficiently compact for optimal data synchronization. The incoming arm contained two, and the outgoing arm three pairs of single-sided sensors. Plane 4, the UV one in Fig. 1, was rotated by 45°, to resolve ambiguities in reconstruction from multiple outgoing tracks. Events were triggered on the coincidence of signals from the pair of plastic scintillation detectors downstream of the telescope. The angular resolution was 2.8 μrad in the incoming arm, and 5.2 μrad on the angular difference of trajectories in the two arms, with performance limited by MCS in the sensor layers, while the position resolution of the sensors closest to the crystal determined the resolution of 6.9 μm in both planes of the impact parameter at the crystal entry face. The ten sensors, each one a single-sided silicon strip detector 320 μm thick, consisted of 639 strips with 60 μm readout pitch; the 7 μm spatial resolution was achieved by means of charge sharing and a floating intermediate strip. They were instrumented by a system based on the CMS Tracker electronic readout chain, including analog signal readout for optimal spatial resolution. The system was based on modified CMS software and hardware to provide a data acquisition capable of peak trigger rates of at least 7 kHz.

The bent crystal was mounted on a four-stage goniometer, industrially produced, installed on a very stable granite table between the two arms of the telescope, as shown in Fig. 2. The four motion units, two linear and two angular, were conceived to freely adjust the position and orientation of the crystal with respect to the particle trajectories. With the horizontal and the vertical actuators, the crystal could be aligned to the beam line with an accuracy of 1.5 μm, within a range of

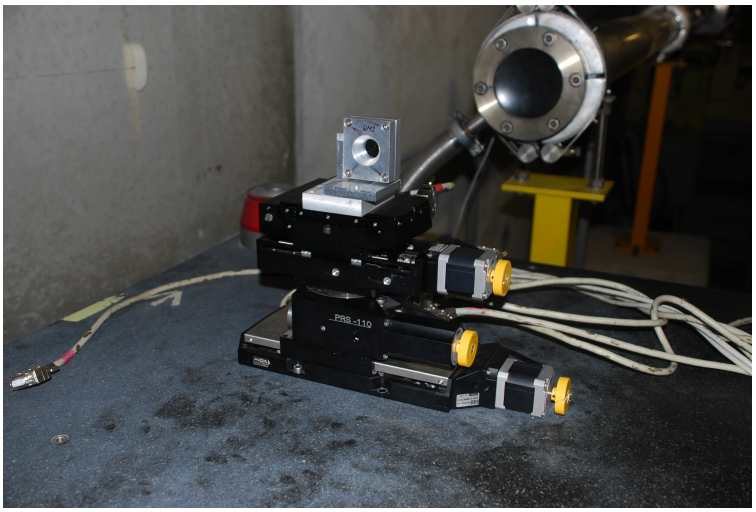

Fig. 2. The UA9 goniometer on a granite table of the H8 beam line. A crystal is mounted on two linear and two rotational stages.

about 10 cm. The upper rotational stage, hosting the crystal-holder ensemble, was used to rotate it around the vertical axis and align the crystal plane with the beam axis with an accuracy of 2 μrad. The other angular stage was used to rotate the crystal around the horizontal axis (cradle) and align the crystallographic axis with the beam, for axial channeling studies. The remote control of the goniometer, integrated into the data acquisition system of the experiment, continuously provided information on crystal position and orientation. A laser system, with optical reflectors and light splitters, was used to perform the preliminary alignment of crystal relative to the beam direction within a range of 100 μrad.

The recorded data were used to determine the kinematics of each event, through a procedure imposing simple fitting constraints. The incoming and the outgoing tracks, computed independently of each other, were assumed to pass through the points measured by the first two and the last three planes of the telescope, respectively. By imposing the same impact point d_0 at the crystal entry face, the particle trajectory along the whole detector could be determined. The fitting procedure provided information on incoming and outgoing angles, θ_{in} and θ_{out}, respectively, on the coordinates of the impact parameter d_0 with crystal, at $s = 0$, the origin of the longitudinal axis, and on the deflection angle $\Delta\theta = \theta_{\text{in}} - \theta_{\text{out}}$ imparted during crystal traversal, in each plane.

Before each crystal test, the incoming beam parameters and the detector resolution were measured in a dedicated alignment run, with the crystal retracted far from the beam line and the straight particle trajectories perturbed only by interactions with the telescope planes and the residual air molecules. From the recorded distributions of d_0 and θ_{in}, the expected beam shape and divergence at the crystal

entry face, in the horizontal and the vertical planes, were provided, while, from the distribution of $\Delta\theta$, the measured value of the angular resolution of the telescope was obtained. Beam parameters, recorded for several runs, were varying in the ranges: $\sigma_x \in [1.0, 1.3]$ mm, $\sigma_y \in [0.7, 1.0]$ mm, $\sigma_{x'} \in [9.1, 11.9]$ μrad and $\sigma_{y'} \in [5.8, 9.0]$ μrad. The telescope resolution was steadily close to 5.2 μrad in both planes, a value also confirmed by numerical simulations of MCS effects in the setup. Occasionally occurring deviations of the recorded resolution from that value indicated the presence of forgotten obstacles, air leakages or other perturbations in the beam line.

Subsequent high-statistics runs were dedicated to collect large sets of data resulting from crystal-particle interactions. The test crystal was inserted into the beam line and a large number of events was recorded in fixed positions, in particular, in channeling and VR orientations and while performing angular scans at very low rotational speed. The data were processed offline to discard events with trajectories not impacting onto the crystal face (geometrical cuts were applied outside the impact parameter range where the beam profile was broadened by MCS during crystal traversal) or having the incoming horizontal angle diverging too far from the average beam direction (angular cuts excluded horizontal incident angles larger than θ_c). In addition, the effect of crystal torsion on trajectories intercepting the crystal outside the horizontal mid-plane was compensated numerically. In practice, the optimal orientation for channeling was recorded as a function of the vertical impact position and a linear interpolation of the latter versus the former variable was computed. For each trajectory, the value of $d_{0,y}$ was computed, the corresponding optimal angle for channeling estimated through linear interpolation, the difference of that value with the optimal angle for channeling at $d_{0,y} = 0$ was evaluated and the result was finally subtracted from the original value of $\theta_{\rm in}$. The procedure was systematically applied to correct the torsional artifacts from the channeling performance. Details on data processing and on torsion compensation are extensively discussed in Refs. 34 and 36.

Examples of data recorded in H8, on which geometrical and angular cuts and the numerical compensation of the torsion were applied, are shown in Fig. 3. Such data were used to establish crystal performance. The channeling efficiency was calculated as the ratio between the number of channeled particle (the ones within $\pm 3\sigma$ of the channeling peak) and the total number of particles impinging on the crystal within a given angular range. The nuclear dechanneling length $S^n_{\rm dec}$, predominant in short bent crystals,[37] was also computed for a given angular range. Using the data collected in optimal channeling orientation, a plot was produced of the particle density distribution as a function of $\Delta\theta_x$, the crystal-induced horizontal deflection. The $\pm 3\sigma$ borders of amorphous and channeling peaks were identified and an exponential fit of particle density was performed between them to evaluate the e-folding coefficient providing the $S^n_{\rm dec}$ estimate. Finally the volume reflection efficiency was evaluated as the fraction of particles deflected by an angle in the range $\in (2\theta_c, 3\theta_c)$, in which the VR process should be independent of the crystal

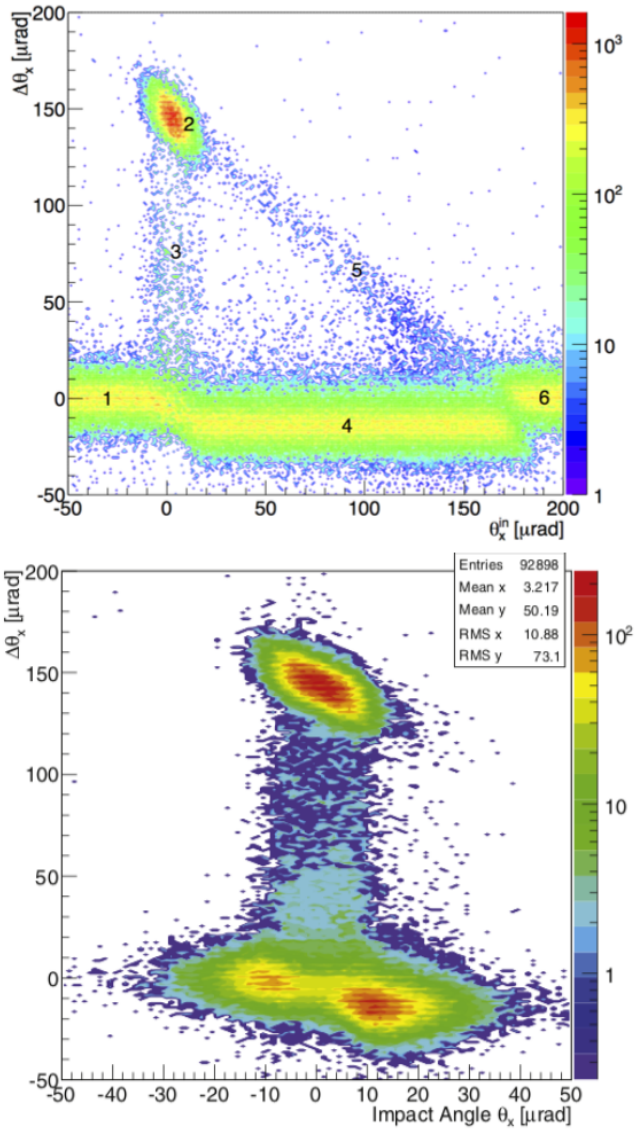

Fig. 3. Angular scan data (top); data recorded in optimal orientation for channeling and real crystal (bottom) — the deflection angle $\Delta\theta_x$ due to the crystal traversal is plotted as a function of the particle incoming angle $\theta_{x,\mathrm{in}}$.

characteristics. Ten crystals, seven strip and three QMs, were prepared for extensive tests in H8, the aim of which was to define and optimize the data-taking and the data-analysis methods and to provide a set of homogeneous data to be compared and to validate simulation codes for particle tracking during crystal traversal. An overview of the ten crystal parameters and performance is shown in Table 1.

Table 1. Parameters and performance of ten crystals used to define data-taking and post-processing procedures and validation of simulations.

H8 crystals	Origin	L [mm]	θ_b [μrad]	R_b [m]	Torsion [μrad/mm]	$\eta_{\rm ch}$ [%]	$S^n_{\rm dec}$ [mm]	$\theta_{\rm VR}$ [μrad]	$\eta_{\rm VR}$ [%]
STF38	INFN	1.89	221.23 ± 0.05	8.95 ± 0.01	-5.6 ± 0.4	32.9 ± 0.3	0.84 ± 0.04	-13.10 ± 0.01	79.3 ± 0.8
STF45	INFN	2.00	143.78 ± 0.07	13.91 ± 0.01	7.4 ± 0.6	54.0 ± 0.3	1.28 ± 0.09	-14.03 ± 0.12	88.8 ± 0.3
STF47	INFN	3.10	34.10 ± 0.02	90.90 ± 0.06	-2.5 ± 0.3	45.1 ± 0.2			
STF48	INFN	2.00	143.60 ± 0.02	13.89 ± 0.01	6.9 ± 0.3	41.0 ± 0.1	1.47 ± 0.08	-14.15 ± 0.05	76.8 ± 1.3
STF49	INFN	0.80	246.65 ± 0.03	3.24 ± 0.01	5.3 ± 0.3	34.6 ± 0.3	0.18 ± 0.01	-9.14 ± 0.23	91.9 ± 1.5
STF50	INFN	2.00	139.59 ± 0.01	14.33 ± 0.01	5.00 ± 0.4	45.2 ± 0.1	1.29 ± 0.08	-13.57 ± 0.03	76.0 ± 0.2
STF51	INFN	3.00	33.40 ± 0.01	89.82 ± 0.03	-1.1 ± 0.3	44.1 ± 0.1	1.29 ± 0.08	-14.41 ± 0.02	79.4 ± 0.5
QMP27	PNPI	1.77	108.13 ± 0.01	16.37 ± 0.01	1.4 ± 0.5	50.4 ± 0.2	1.35 ± 0.08	-12.85 ± 0.06	90.5 ± 1.5
QMP29	PNPI	6.00	33.95 ± 0.01	176.73 ± 0.02	-0.2 ± 0.2	56.2 ± 0.1		-13.82 ± 0.04	86.8 ± 1.1
QMP32	PNPI	0.96	170.69 ± 0.05	5.64 ± 0.01	-0.6 ± 0.6	40.9 ± 0.5	0.37 ± 0.04	-11.21 ± 0.32	88.2 ± 2.3

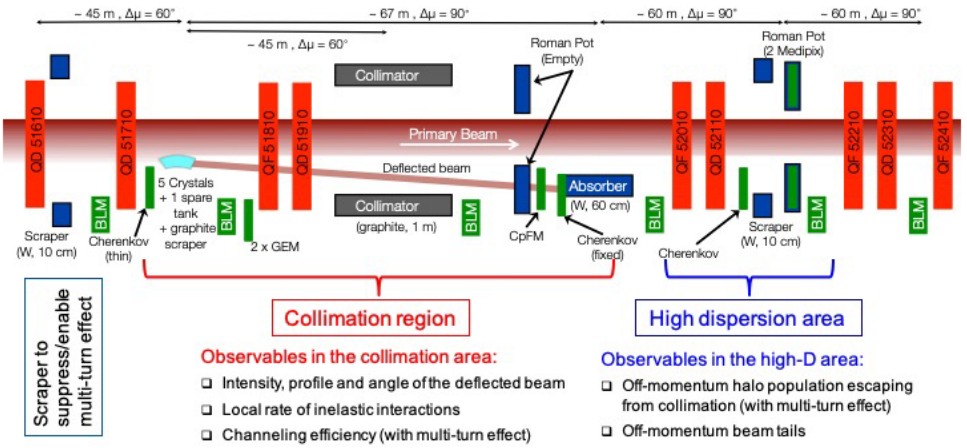

Fig. 4. Synoptic view of UA9 layout.

3. The UA9 Layout in the SPS

UA9 is a CERN-based experiment, approved in 2010, to study beam steering assisted by bent silicon crystals in the SPS.[38] Carried out by an international collaboration, the investigation is still operational. The layout was upgraded in 2017, to permit more complex beam manipulations in view of extending the discovery potential of hadron colliders to fixed-target experiments.[39,40] The original layout, on which crystal collimation was studied and most of the results were recorded, was composed of two sections. The former, the cleaning region, about 60 m long, was heavily instrumented for performance evaluation of the various cleaning options proposed. The latter, the high-dispersion (HD) region, about 120 m downstream the crystals, was equipped with additional detectors for recording off-momentum halo leakage. A synoptic view of the full layout is shown in Fig. 4.

3.1. *The cleaning region*

The UA9 cleaning region, housing the main components of the collimation setup, shown in Fig. 5, was installed in the long straight section LSS5 of the SPS. The primary collimator, sitting just upstream the quadrupole QF518, was followed at about 90° phase advance by the absorber, located just upstream the quadrupole QF520. In more detail, four silicon crystals (Cr1–Cr4) mounted on accurate angular actuators (Gonio1–Gonio4) were installed in two vacuum vessels both named IHEP goniometer, manufactured at the Institute for High Energy Physics in Protvino, Russia. The two vacuum tanks were installed in sequence. Each crystal could be independently operated as a primary halo deflector. About 45 m upstream the IHEP goniometers there was a tank, named TCXHW.51651, containing two horizontally movable tungsten jaws 10 cm long, by which the beam envelope could be shaped and the multi-turn channeling effect eventually controlled. Three tanks were

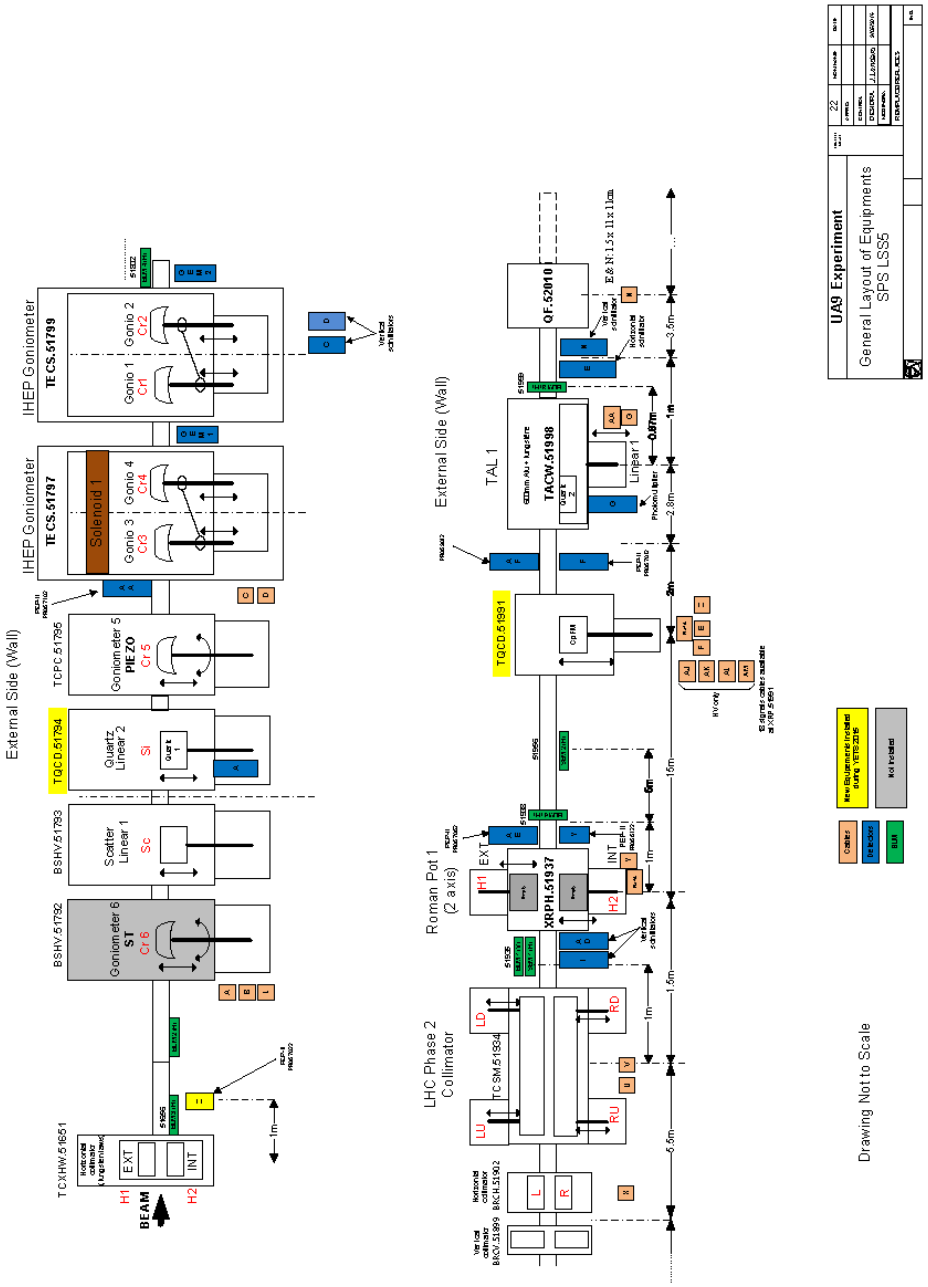

Fig. 5. Cleaning region of the UA9 layout.

located just upstream the first IHEP goniometer. The Scatter Linear 1 hosted a single-sided movable carbon bar 10 cm long, that could be used as primary amorphous collimator to compare its effect to that of the bent crystals. The Quartz Linear 2 tank contained a quartz bar that could be inserted in the vacuum pipe to detect Cherenkov signals induced by the passage of the halo beam. The Goniometer 5 Piezo, built as a prototype of the LHC angular actuator, precisely operated by a piezo-electric system, was used to check its functionality with beam before producing the final actuator series for LHC. The two IHEP Goniometer tanks were almost identical. However the first one was built with higher mechanical accuracy and its linear and angular crystal positioning was more reproducible. Moreover it was equipped with a solenoid to mitigate e-cloud effect, produced by high electron emissivity aluminum components in the vacuum pipe.[41] The LHC Phase 2 Collimator, originally built as a prototype for LHC and later reused in UA9, housed two horizontal bars 1 m long made of carbon. It was used as the reference element for beam-based alignment of the other movable devices. It could also provide information on the shape and the position of the deflected halo, by slow linear scans of the vacuum pipe from the fully retracted position to the beam periphery. The Roman Pot 1 with two horizontally movable pots housing Timepix sensors was located just downstream the LHC Collimator. Its function was to record the intensity and the 2D profile of the deflected beam. The CpFM was a Cherenkov-radiator quartz bar in a standalone vacuum tank. By sliding the bar into the vacuum pipe the intensity and the horizontal shape of the deflected particles could be recorded. The TAL1 was a 60 cm tungsten single-sided horizontally movable bar, contained in a vacuum tank, by which the particles deflected by the crystals could be intercepted and safely disposed. A Cherenkov detector was attached to the upstream side of the tungsten absorber to provide information on the number of particles hitting the bar. One crystal at a time was inserted at the edge of the circulating beam as the primary collimator. The nominal betatron functions of the cleaning region are shown in Table 2. The phase advance is relative to the position of the first crystal. Detectors sensitive to secondary particles produced by nuclear interactions of the deflected halo with obstacles in the vacuum pipe were installed downstream each UA9 movable device and were used for the setting up and optimization of the collimation configuration.

Table 2. Betatron functions of the crystal-collimation layout.

Element	s [m]	β_x [m]	β'_x	D_x [m]	D'_x	$\Delta\Phi_x$
Crystal	5181	82.1	−1.89	−0.77	−0.02	0.0
Collimator	5222	24.2	−0.78	−0.20	0.01	0.159
RP1	5224	28.2	−0.86	−0.19	0.01	0.175
Absorber	5244	87.7	−2.11	0.002	0.01	0.241

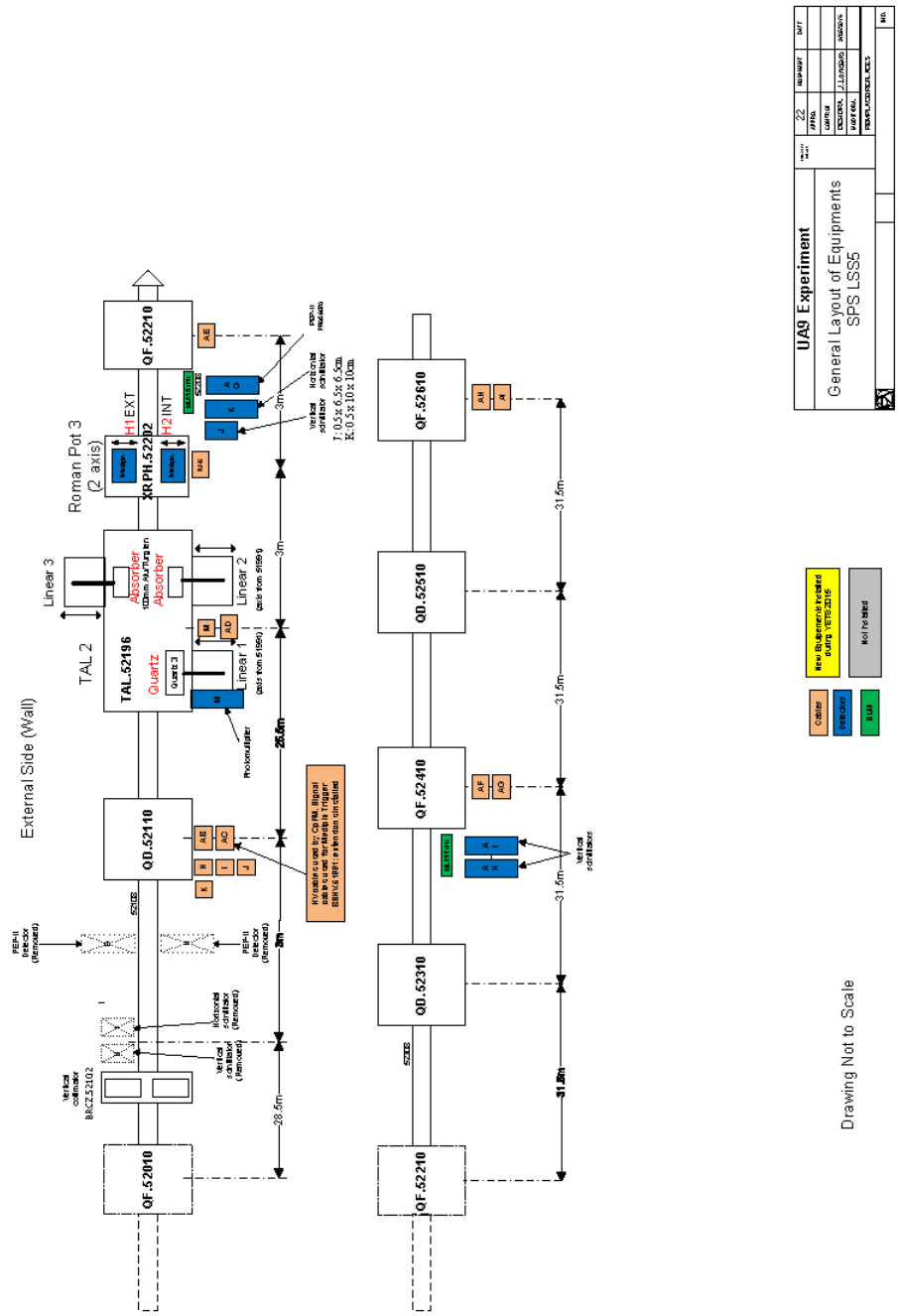

Fig. 6. High-dispersion region of UA9 layout.

3.2. *The high-dispersion region*

In the high-dispersion region, shown in Fig. 6, the dispersion function gradually rose from $D_x \approx 0$ m to a first maximum of ≈ 3.8 m, in the middle of the quadrupole QF522, followed by a second maximum of ≈ 4.6 m in the middle of QF524. Particles that had lost energy in a single diffractive scattering or in a nuclear interaction with the crystal, not intercepted by the TAL1, were shifted toward the inner side of the vacuum pipe as the dispersion function increased. The TAL2 vacuum vessel contained two horizontally movable bars, located on both sides of the circulating beam, each of them made of a 10 cm long tungsten inner core, with a 1 cm $\times$ 1 cm square section, merged in a C-shaped duralumin envelope of the same length. The bar on the inner side was used to intercept particles having lost energy, shifted toward the inside of the SPS circumference because of the large dispersion. Scintillation counters and Cherenkov detectors were installed downstream to record secondary showers produced by off-momentum particles intercepted by the TAL2, during the displacement from fully-retracted position to beam periphery.

Such a procedure could provide information on the spatial density distribution of the off-momentum particles and on the improved efficiency of crystal-assisted collimation system.

3.3. *Beam detectors*

During the crystal-collimation tests, the SPS beam instrumentation and other detectors developed *ad hoc* were used to continuously monitor the circulating beam parameters, the loss rate and the trajectories and shape of the deflected halo.

The Beam Current Transformer (BCT) was used to measure the intensity of the circulating beam. In the SPS there are two different types of BCTs. The fast BCT measures the intensity of a single bunch every five RF buckets, that is every 25 ns. The BCTDC measures the intensity of the entire beam every turn. Their information was combined to monitor the beam status during data taking and to normalize loss rate measurements during the offline analysis.

The Beam Position Monitor (BPM) provides information on the centroid position of the circulating beam. It was used to ensure that the circulating beam orbit was under control in each run. Moreover, a similar detector was mounted on the jaws of the LHC-type collimator to provide information on the distance of the beam centroid from the mid-point of the two jaws.[42] Its main use was to precisely monitor the orbit stability during data taking and eventually to correlate unwanted losses to possible orbit jitter.

The Timepix inserted in the Roman pots was a hybrid pixel detector developed by the CERN-based European Medipix2 Collaboration.[43] It consisted of a CMOS readout circuit (Timepix) bump-bonded to a 300 μm thick silicon pixel detector with a matrix of 256 $\times$ 256 square pixels of 55 μm pitch. Each cell in the matrix contained a charge-sensitive preamplifier, a single threshold discriminator, a time-based logic and a 14-bit pseudo-random counter with overflow control logic.[44] The

Timepix allowed to acquire data inside a configurable time window called shutter. When a particle generated a signal over a selected threshold, the pixel was triggered generating a hit signal. Every pixel could be configured independently in three different modes. In the Medipix counting mode, each pixel counted the number of hits inside the shutter. In the Time of Arrival (TOA) mode, each pixel counts the number of clock cycles from the first hit to the end of the shutter signal. Finally, in the Time over Threshold (TOT) mode, each pixel counted the number of clock cycles with an over-threshold signal inside the shutter. The three modalities were used to optimize the signal-to-noise ratio.

The plastic scintillators coupled to a Photomultiplier Tube (PMT) and the BLMs were used to measure losses generated during a particular sequence of operations (i.e. angular scans, linear scans, etc.).

The CpFM detector was conceived to count the deflected flux of protons and ions.[45–48] The CpFM consisted of two fused silica radiators with an i-shape ($5 \times 10 \times 300$ mm^3) intercepting particles inside the beam pipe and creating Cherenkov light. The bars were coupled to a bundle of quartz fibers guiding the light onto two PMTs. The vacuum-air interface was realized by a quartz u-port. The PMTs were read by an ultra-fast analog memory, the WaveCatcher, able to store up to 2.4 μs of data, with a sampling frequency of 400 MHz. A motorized bellow allowed to move the radiators from the fully retracted position (10 cm from the beam) up to the primary beam periphery. One of the two bars was 5 mm closer to the beam and was meant to intercept the flux of protons to be measured. The other bar, when retracted from the beam to be measured, provided a measurement of the background. The resolution of the CpFM for 100 incoming charges was assessed at 15%. The detector was used with both protons and Pb ions. The online and offline optimization of the operational setup of the readout chain (PMT gain, WaveCatcher setup, trigger setup) changed considerably in the case of protons or ions, as well in the analysis of the signal of the detector in terms of amplitude and time distribution. The CpFM was used for linear scans. Slowly moving the CpFM toward the channeled beam it was possible to obtain the integrated channeled beam profile. Because of some problems in the collection of the light at the vacuum-air interface, it was very hard to convert the amplitude of the CpFM signal into the number of protons.

3.4. *The angular actuator*

The IHEP goniometer was conceived and built to support simultaneously two crystals and to operate each of them independently of the other. The scheme adopted is shown in Fig. 7, where a QM-type crystal is in the upstream position and a strip-type in the downstream position. Each crystal could be moved along the horizontal direction and oriented with respect to the beam trajectory by using two linear transverse mechanisms, operated by two independent driving motors. Each motor drive allowed the crystal to be positioned in a range of about 100 mm. At the maximal drive elongation from the fully-retracted position, the crystal position

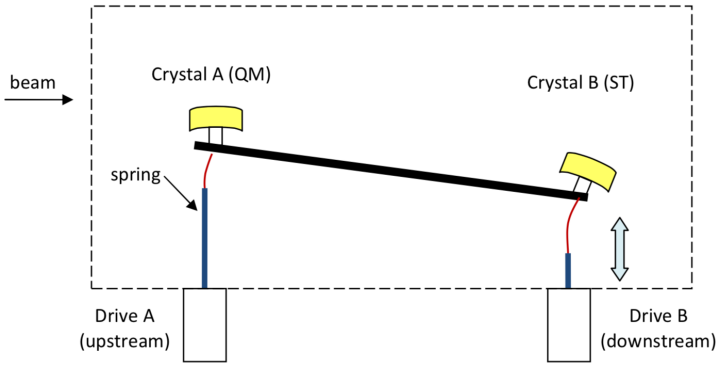

Fig. 7. The IHEP-goniometer kinematics. The scheme shows the Crystal A (upstream) alignment: the position is controlled by an equal, synchronous motion of the Drive A and B; the angle by the Drive B, only.

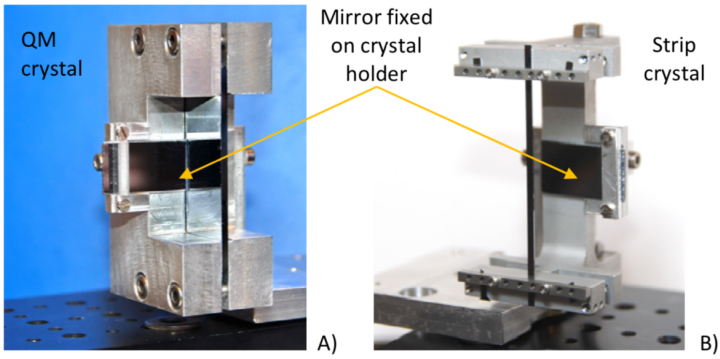

Fig. 8. Mirrors required to orient the crystal in the accelerator.

exceeded by 2 mm the center of the vacuum pipe to permit approach to the beam periphery even in the presence of a local closed orbit distortion. The distance separating the two crystals was 500 mm to obtain sufficient lever arm for retraction of the crystal not in use.

To avoid excessive mechanical flexural stress of the springs at the extremities of the bar connecting the two crystals, the difference of the horizontal positions of the two drives was limited to 35 mm, in all conditions. A mirror attached to the holder of each crystal, as shown in Fig. 8, accurately pre-aligned to the surface of the crystal, provided the optical reference for correct alignment in the SPS ring, based on laser, auto-collimator and contactless angular measurements. The calibration of the crystal A orientation as a function of the difference of the two drive positions is reported in Fig. 9, where the linear part of the crystal orientation variation (blue line) is obtained by interpolating the data (blue dots), collected by simply moving the drive B. In this example, the orientation of crystal A could be changed in a

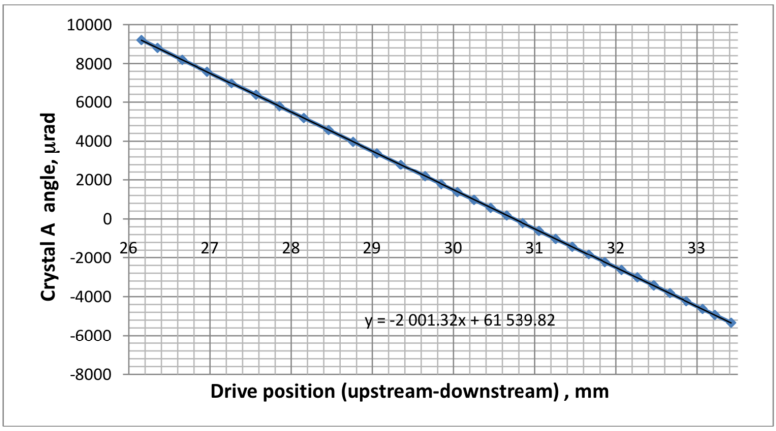

Fig. 9. (Color online) Angular orientation of the crystal A as a function of the position difference Drive A–Drive B.

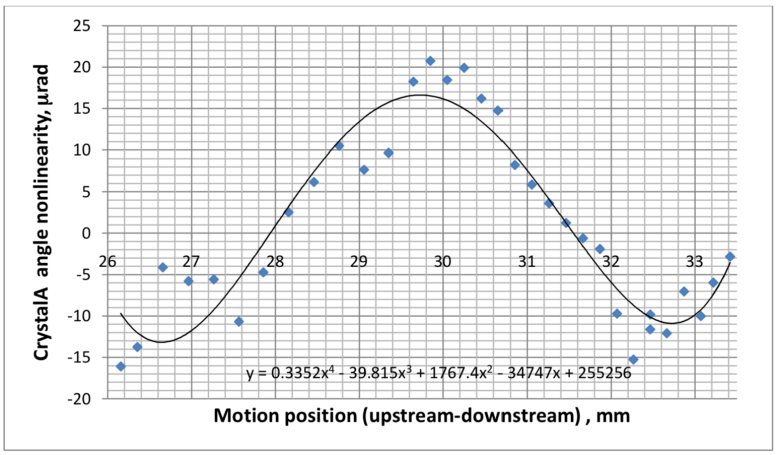

Fig. 10. Nonlinear variation of the angular orientation of the crystal A (obtained after the subtraction of the linear interpolation of Fig. 9) as a function of the position difference Drive A–Drive B.

range of more than 15 mrad, while the crystal B position was constantly behind that of crystal A by more than 26 mm. Figure 10 reports the nonlinear part of the orientation variation. The average trend (solid curve) was rather reproducible, provided the sequence of the drive displacements was rigorously the same, while the measured values were scattered around the average over a range of ± 10 μrad. Such an accuracy of the angular orientation was sufficient to guarantee the data consistency from run to run; however the procedures required to control the nonlinear average behavior of the system were tedious and time consuming.

4. Experimental Procedures for Crystal Collimation

Well-established procedures were systematically applied during the SPS runs dedicated to investigate the feasibility of crystal collimation. They were conceived to ensure reproducible beam conditions and layout configurations and to apply comparable methods of collecting experimental data and performing their analysis, for the entire duration of the study.

4.1. *Alignment*

Beam-based alignment of movable UA9 devices, associated to circulating beam radius measurement, is the procedure selected for optimal positioning of crystal and absorber and safer operation of Roman pot and CpFM during UA9 collimation tests.

At the beginning of each data-taking run, the beam emittance was measured and the *ad hoc* beam-based alignment procedure applied. The jaws of LHC Phase 2 Collimator were positioned in the periphery of the beam envelope to determine symmetric sharp edges of the desired width, typically at $\pm 6\sigma_x$, where σ_x is the RMS horizontal beam size, to which other UA9 movable devices could be aligned. Each device was displaced in small steps toward the beam center, until its position surpassed that of the jaws and the device became the first obstacle to circulating particles. Such critical position could be identified by the abrupt beam loss increase, recorded by BLM or scintillation counters downstream. The correct alignment was finally obtained by reversing the last forward steps of the movable device until the loss increase disappeared. Although time-consuming, such a procedure was mandatory to guarantee relative alignment of movable devices, with accuracy better than a tenth of mm, independently of possible variations of emittance or closed orbit from one run to another. Moreover, by the appropriate choice of the gap of collimator jaws, it was possible to position the crystal and the secondary absorber at an optimal distance from beam center, as required for the specific test underway.

4.2. *Angular scan and beam splitting operation*

Angular scan is the method to explore in detail the functional dependence of crystal-particle interaction rate on orientation of crystalline planes with respect to halo particle trajectory. Angular scan consists of slowly rotating the crystal with respect to the beam axis, while recording the loss rate downstream the crystal and the absorber with BLMs and scintillation counters. Loss rate is proportional to nuclear interaction rate in the crystal or the absorber, respectively. Its shape analysis allows identifying optimal channeling orientation, where loss rate is minimal, amorphous orientation, where loss rate is maximal and rather flattish, before and after the channeling valley and volume reflection range, where the losses exhibit a plateau of intermediate rate. Accurate profile recording imposes extremely slow rotational speed of the crystal and careful compensation of the e-folding descent

of the circulating intensity. In crystal channeling orientation, optimal halo spitting from the circulating beam occurs.

UA9 angular scans were generally performed at 1 to 5 μrad s^{-1} angular speed, with crystal and absorber transverse positions kept at constant distance from the beam axis. Absorber position was in general slightly behind crystal aperture, normalized through betatronic functions, to favor multi-turn capture into channeling states. Channeling orientation (CH) was identified through minimal rate of crystal inelastic interactions and maximal rate at the absorber, simultaneously recorded. In volume reflection (VR) orientation crystal loss rate decreased and absorber loss rate increased by smaller amount than in channeling orientation. The VR plateau was sometimes shaped with lousy edges that made difficult precise determination of crystal bending angle (that should be equal to the VR plateau length). Timepix or the CpFM, inserted in the deflected beam trajectory, allowed recording channeled particles flux and separation of halo deflected spot from beam periphery, correlated to crystal bending angle through the transport matrix from the crystal to the observation azimuth. To explore in great detail the time evolution of loss rate, angular scans were sometimes lasting very long, up to 20 min. In such cases, loss rate was affected by beam lifetime and radiation monitor counting was following e-folding reduction of circulating current.[49] To mitigate such correlation, a normalization procedure was systematically applied. The value of the circulating beam intensity recorded with BCT was interpolated with a third-order polynomial function and the loss rate was divided by the simultaneous value of the beam current obtained from the interpolation. While the closed orbit is generally stable within the error of the orbit pick-ups, sometimes, abrupt loss induced by power supply glitches and closed orbit change was recorded during long lasting angular scans. No way was found to compensate for it. Loss shape was finally plotted as a function of crystal orientation, normalized to the average loss value in amorphous orientation. The average ratio of amorphous to channeling rates, $R_{\rm loss} = \dot{N}_{\rm AM}/\dot{N}_{\rm CH}$, named loss reduction factor, was used to quantify crystal effectiveness as primary collimator. The angular scan procedure was providing information on the optimal orientation for channeling, with RMS uncertainty of ± 3 μrad due to goniometer nonlinearity and experimental errors (random and systematic), and on the value of θ_b, with a relative uncertainty typically of a few %. In channeling configuration, the crystal position was set with 5 μm accuracy and its orientation with 2.5 μrad RMS uncertainty, made possible by the accurate data post-processing. In such configuration, optimal separation of halo particles from the circulating beam, with the minimal beam loss regime and angular kick very close θ_b, was obtained. Optimal beam splitting regime was ensuring halo disposal onto the absorber, in the safest conditions. More recently, the layout in LSS5 was modified and beam slitting exploited to send halo onto an internal target or onto another internal crystal in view of investigating fixed-target operation modes.[50,51]

One of the first angular scans recorded in UA9, using the crystal STF9 (see description in Table A.1), is shown in Fig. 11.[24] The counting rate of the BLM

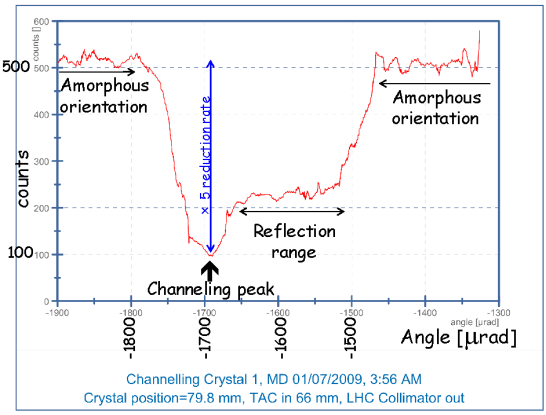

Fig. 11. An example of angular scan in UA9.

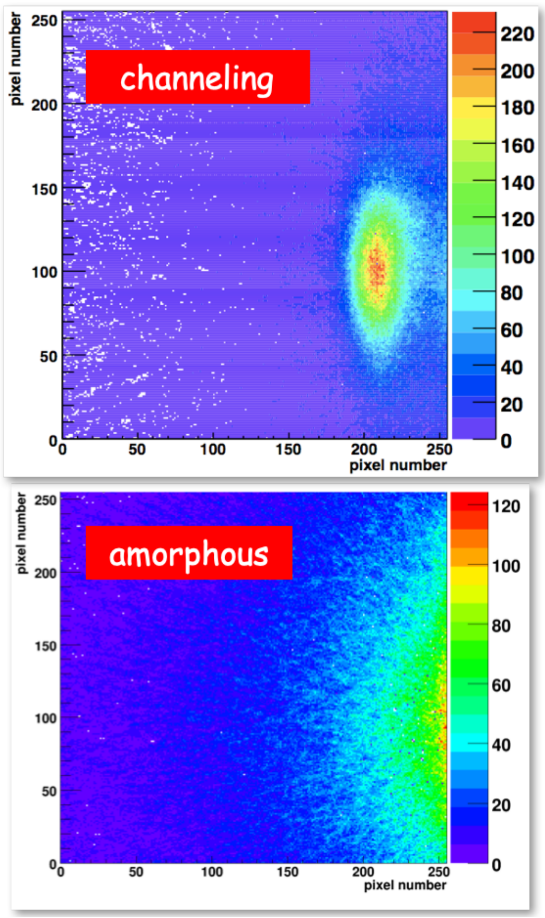

Fig. 12. An example of beam splitting in UA9.

downstream the crystal is plotted as a function of crystal angle. The scan duration was sufficiently short to assume constant circulating current and avoid normalization. Four distinct angular regions could be identified, in which different types of particle-crystal interactions were predominant. At the beginning and the end of the scan, the crystal was behaving as an amorphous target and the counting rate was 500 s^{-1}. In channeling, the counting rate reached the minimal value 100 s^{-1}, implying $R_{\rm loss} = 5$. In VR, the loss rate plateau was 220 s^{-1} slightly larger than the channeling peak. The VR angular range was ≈ 150 μrad, close to the value of θ_b in Table A.1.

An example of beam halo splitting recorded by the Timepix detector in Roman pot 1 during an angular scan is shown in Fig. 12.[24] In the top image, with crystal STF9 oriented and kept in optimal orientation for channeling, the deflected beam was well separated from the circulating beam periphery. In the bottom image, in amorphous orientation, only the background due to MCS was visible. Note that the color codes indicating the particle flux per pixel differ by about a factor of two in the two images.

4.3. *Linear scan*

Linear scan is very effective to measure beam splitting parameters and transverse distribution of particles traveling at large amplitude. It consists of moving a massive scatterer from the fully-retracted position, behind the vacuum pipe, to the beam periphery and simultaneously recording, with a BLM downstream, the rate of secondary particles generated by collisions with the incoming particles. The counting rate is proportional to the integrated halo density intercepted. Its derivative provides the particle density distribution along the axis of the scatterer motion, generally the horizontal one, for UA9. Drawbacks of linear scan are threefold: intercepted particle trajectory is strongly perturbed, intensity calibration is very cumbersome and beam periphery is lousily identified.

In channeling orientation, four regions with different populations, pictorially shown in Fig. 13, are expected. The first outermost region, drawn in black, reveals background composed of particles that had diffused to large amplitude. Its density, almost constant with x, should be accurately evaluated and subtracted from the measurements in the other regions. In the second region, drawn in blue, the loss rate increases abruptly as the jaw interacts with the channeled beam. The integrated counting rate could be fitted with an error function. The derivative of the counting rate should reproduce the Gaussian profile of charge distribution density and provides average and standard deviation of beam deflection at the scatterer azimuth. The area of the Gaussian distribution is proportional to the total number of channeled particles. In the third region, drawn in green, the particle density is essentially determined by the probability of dechanneling events, linearly increasing with the crystal length traversed. The angular kick imparted to a dechanneled particle also increases with the crystal length traversed before the dechanneling event.

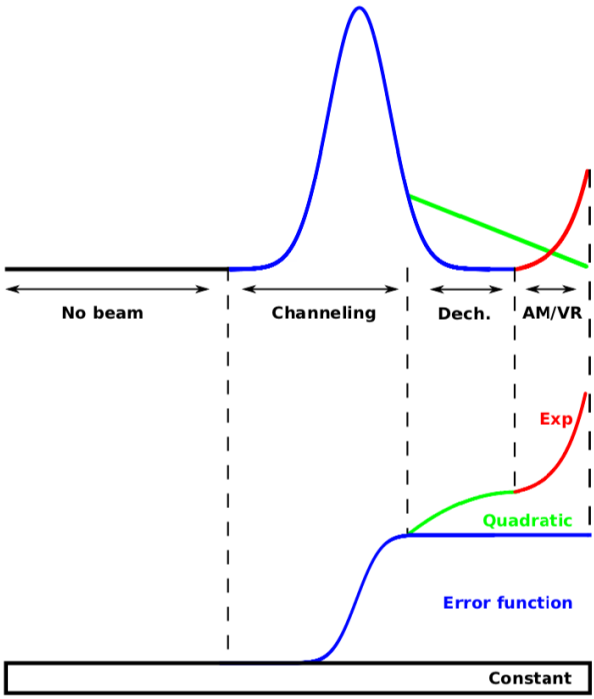

Fig. 13. (Color online) Pictorial view of the loss regimes during a linear scan in channeling configuration.

Because of this, dechanneled particle density is expected to increase linearly with distance from the beam periphery and integrated counting rate to decrease with the square of the distance. In the innermost region, drawn in red, contribution to losses is determined by amorphous scattering and volume reflection, whose probability is not zero even in channeling mode. Particle density should thus decrease exponentially with the distance from the beam, as the integrated counting rate.

In UA9, linear scan was rather regularly performed with crystal and absorber in cleaning configuration, with the secondary absorber generally at normalized aperture slightly larger than that of the crystal. The inner jaw of the LHC phase 2 collimator was used to scan the vacuum pipe and intercept the particles directly scattered or deflected by the crystal itself. Particles escaping from the secondary absorber generated the multi-turn halo that could perform one or a few revolutions before interacting again with the crystal or the absorber. In Fig. 14, one of the first linear scans performed in UA9 is shown. After the offset subtraction from the counting rate, the data were normalized to the rate recorded when the collimator was at the same normalized position of the crystal. Finally, the position values were transformed into crystal kick values through the corresponding linear transfer matrix. The blue dotted line represented the optimal error function interpolation of the experimental data. It provided channeling kick, deflection spread and channeling

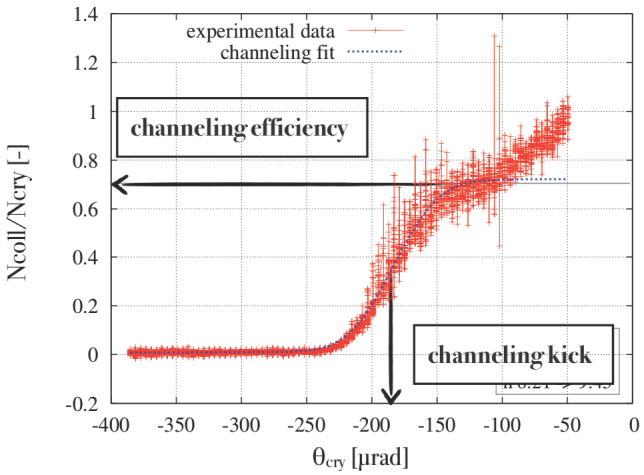

Fig. 14. (Color online) An example of linear scan in UA9.

efficiency. Linear scan method is described in detail in Ref. 52. Recently, the linear scan was operated using the CpFM as scanning collimator and, at the same time, as direct halo detector.[47,48] The results were in all respects similar to those in which scanning was made with the collimator jaw and detection with beam loss monitor.

5. Crystal Collimation in the SPS

The SPS studies performed in the last decade with high-energy protons and heavy ion beams in storage mode have demonstrated that crystal-assisted collimation is feasible in hadron colliders, with superior performance to that of a classical two-stage system based on amorphous primary collimators.[24–28] A number of advantages have been identified. The crystal-collimation setup is more compact, because ideally only two crystals are required, one for horizontal and the other for vertical channeling. Nuclear interactions are strongly reduced because halo particles are captured and deflected into channeling states. The disposal of halo particles is more effective because they encounter the secondary absorber well inside the lateral inner face. The contribution to accelerator impedance is minimal because the crystal length is shorter than that of the primary amorphous scatterer and because the secondary absorber is more distant from the circulating beam. Moreover, in principle only a single massive absorber per crystal would be needed. Even though, in practice, the presence of more than one secondary collimator may be required for reasons of phase space coverage and for machine protection purposes, the larger gaps that could be used should certainly lead to a significant impedance reduction.

In the following subsections, the main steps of the crystal-collimation demonstration in the SPS are recalled, in the perspective of extending the concepts and the experimental data already discussed in Ref. 30.

5.1. *The SPS operational conditions*

The SPS was available for UA9 experiments for two to five dedicated periods of 24 hours each year, starting from 2009. To mimic the behavior of a collider, a *storage operation mode* was applied. Particles were injected and accelerated up to a high-energy plateau, during which the magnetic field was kept constant and the radio-frequency cavities powered, in order to preserve the bunched beam structure for the entire plateau duration, typically of 2–10 h. The beam top-energy, of 120 GeV during the initial runs, was rapidly increased to 270 GeV.

In each proton fill, the injected current typically contained $0.8–1.7 \times 10^{11}$ particles in a single circulating bunch of 2–3 ns duration, confined in a bucket of 5 ns. The halo was produced by multiple Coulomb scattering (MCS) on residual gas in the pipe, by inherent electronic noise of the magnet and RF power supplies and sometimes by the effect of beam instabilities. The beam lifetime was of the order of 10–20 h. To enhance halo population, the lifetime was deliberately reduced to 0.2–2 h, by activating in reversed mode the transverse feedback system.[53] In a typical run, radially diffusing halo entered the edge of the crystal with a flux of about 100 protons per turn of 23 μs duration. The time structure of the halo protons of 2–3 ns every 23 μs was consistently reproduced in the beam detector signals. Instead, the intensity of heavy ion beams was much lower because of their lower production flux. Thus, the ion injection was operated in multi-bunch mode, with 12–20 bunches, each of about 1.5×10^8 particles.

The accelerator optics was the same for protons and ions. The betatron tunes were $Q_h = 26.13$ and $Q_v = 26.18$. The chromaticity was well compensated, slightly positive and close to zero. The physical emittance at 1σ, measured at each fill, was typically of the order of $\epsilon_h = \epsilon_v = 5 \times 10^{-9}$ m $\cdot$ rad.

In diffusing toward the crystal, the halo particles performed combined betatron and synchrotron oscillations. Taking into account that the dispersion function at the crystal azimuth was slightly different from zero (see Table 2), even in the stationary state, the value of impact angle of particles diffusing onto the crystal was modulated at the synchrotron frequency. The amplitude of such modulation was determined by the value of the grazing function $g = (D \times \beta'_x/\beta_x + D')$ computed at the crystal azimuth.[54] The crystal position in the SPS was such that the grazing function had the value $g = 1.2 \times 10^{-3}$ and the impact angle modulation amplitude was $\Delta x' \approx 1.3$ μrad, about an order of magnitude less than θ_c (≈ 10 μrad at 270 GeV and ≈ 15 μrad at 120 GeV). This condition ensured that crystal angular acceptance for channeling was only very slightly reduced by synchro-betatron motion.

5.2. *Observations during the initial exploratory runs*

The first UA9 runs performed in 2009/2010 in the SPS with proton beams of 120 GeV were dedicated to explore the necessary experimental procedures and, at the same time, to identify issues requiring improvement. Angular and linear scans were performed with the first series of four crystals, namely STF9, QMP15,

Table 3. Reduction of the loss rate in channeling orientation.

Crystal name	X_{cr} $[/\sigma_x]$	X_{asb} $[/\sigma_x]$	AM/CH loss ratio	θ_b [μrad]	$\delta\theta_b$ [μrad]	Multi-turn efficiency [%]
STF9	3.1	5.9	6.3 ± 1.3	155 ± 10	16 ± 1	90
QM15	6.0	7.0	3.6 ± 0.7	161 ± 10	20 ± 1	77
QM25	6.9	8.3	6.1 ± 0.3	165 ± 3	11 ± 1	83 ± 3
STF18	6.5	10.4	6.1 ± 0.3	173 ± 3	11 ± 1	75 ± 4

QMP25 and STF18. The extensive analysis of the recorded data is discussed in Refs. 52 and 55. In Table 3, the performance of the crystal-assisted collimation recorded in this period is shown with a single representative result selected for each crystal. In the first column the crystal name is given, followed by the horizontal position of the crystal and of the absorber, in units of the RMS horizontal beam size (σ_x). The fourth column indicates the ratio of the beam loss rates, recorded with the crystal in amorphous and in channeling orientation, respectively, the loss rates being measured by the BLM4-51802 or by the telescope of scintillation counters C–D downstream of the crystal, shown in Fig. 5. In the fifth and sixth columns, the crystal bending angle and its RMS variation measured with angular and/or linear scans are respectively indicated. In the last column, the multi-turn efficiency recorded in linear scan is shown.

Globally, these data indicate that the exploratory runs were immediately effective and successful. Moreover, the test of crystal STF9 provided information on two issues related to crystal alignment that could have impaired the crystal-collimation efficiency. The related observations drew attention to potentially detrimental configurations and suggested systematic checks and corrective actions to avoid them in the subsequent tests. The first negative effect was due to the inaccurate crystal orientation at the installation time and the second was related to the residual torsion of the crystal due to a skew component of the flexural stress imparted by the holder.

Finding optimal orientation for planar channeling is particularly difficult if one of the crystalline axes is almost aligned with the average beam direction. Indeed, in such condition, channeling orientations of the upright planes and of the skew planes are very close to each other and, during angular scan, it is very difficult to distinguish between them. To avoid this inconvenience, during final alignment performed in the SPS tunnel an angular shift of a few mrad around the horizontal transverse axis was imposed on all crystals, to guarantee sufficient inclination of the crystalline axis with respect to the geometrical reference of the beam axis in the vacuum tank. Unexpectedly, the alignment procedure of crystal STF9 was unsatisfactory and the crystalline axis (110) was almost parallel to the geometrical direction of the horizontal beam envelope. Because of this unwanted alignment configuration, planar channeling could be produced not only by the upright oriented (110) planes but also by other skew planes such as (100), (101), (011) and so on.

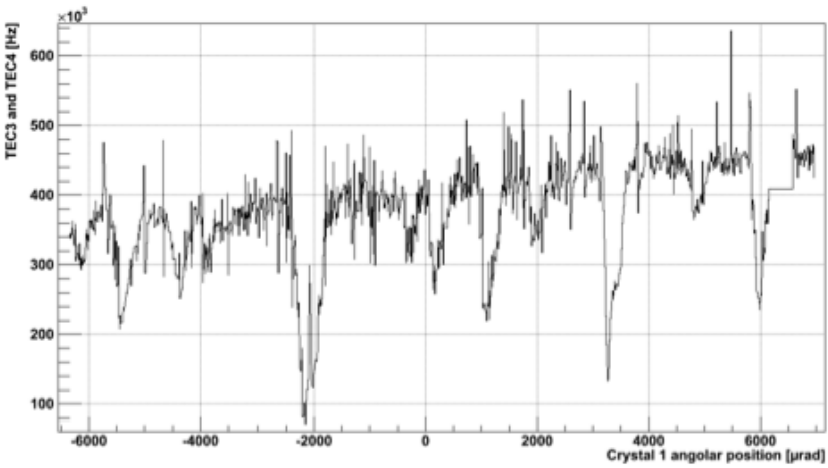

Fig. 15. Very large range angular scan of the crystal STF9.

This effect is visible in Fig. 15, in which a large range angular scan of the crystal STF9 was performed. The loss shape typical of the channeling effect is repeated several times. Such a feature made the crystal STF9 inappropriately oriented for collimation, even if the multi-turn efficiency was large. The orientation for the (110) planar channeling was finally identified in the range from -2200 to -1900 μrad, because of the larger loss reduction at the channeling peak.

In the optimal (110) planar channeling orientation, the deflected beam spot was recorded using the Timepix in Roman pot 1 (RP1) and the centroid was computed and plotted as a function of the crystal orientation. The deflected beam spot, shown in Fig. 16, was slightly tilted as a consequence of the residual torsion of the crystal.

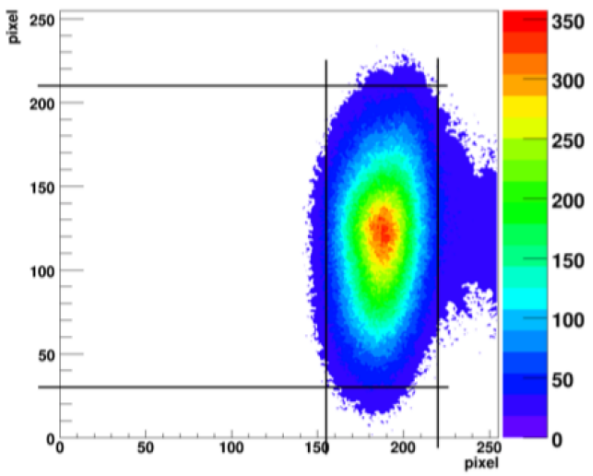

Fig. 16. Channeled beam by the crystal STF9.

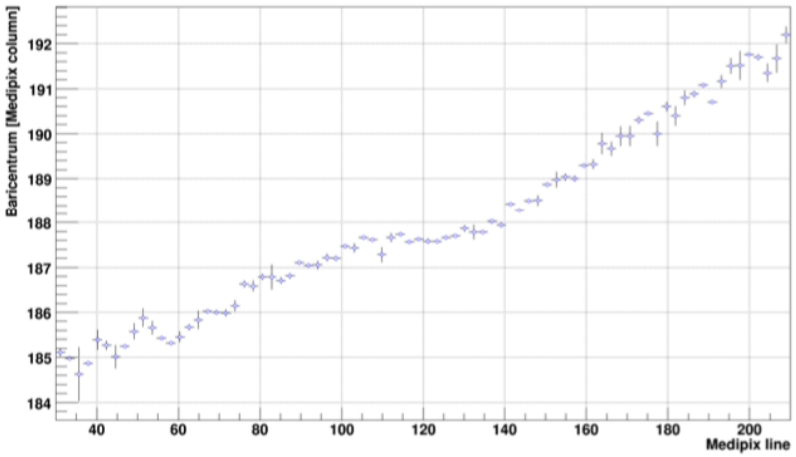

Fig. 17. Evolution of the horizontal position of the centroid of the beam spot vertical slices (plotted in the y-axis) as a function of the vertical slice (plotted in the x-axis).

By segmenting the data into small vertical slices it was possible to compute the centroid of each slice and to determine the evolution of its horizontal position (plotted in the y-axis) as a function of the vertical slice (plotted in the x-axis), shown in Fig. 17. From this, a residual torsion of about 7 mrad/mm could be estimated. Mitigation of the residual torsion was achieved by acting on the alignment of the crystal frame, following the recipe described in Ref. 32.

In Fig. 18, the centroid of the beam spot, recorded by the Timepix in Roman pot 1, was computed as a function of STF9 crystal orientation. The halo beam was

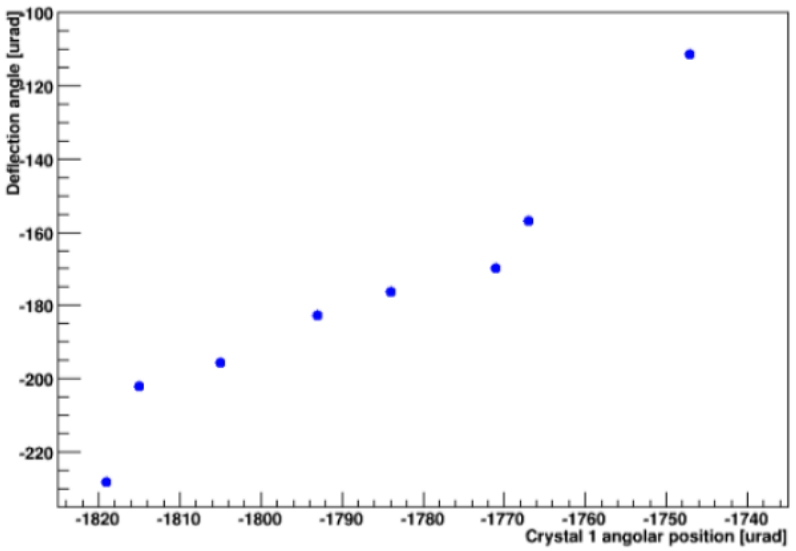

Fig. 18. Horizontal position of the deflected beam during an angular scan of the crystal STF9.

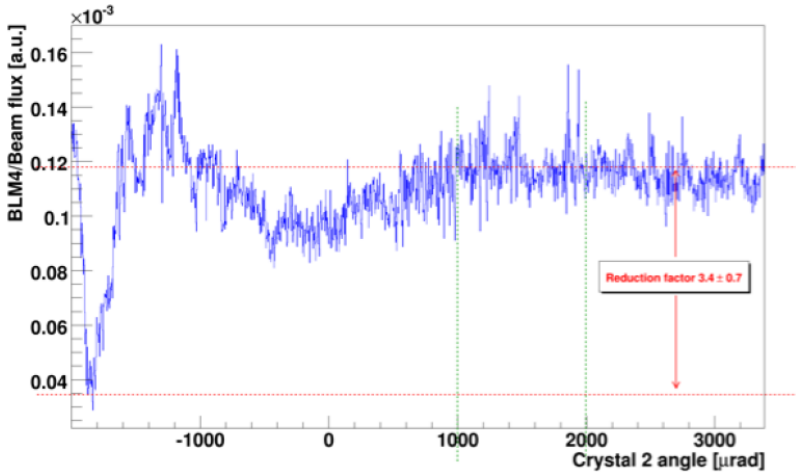

Fig. 19. Angular scan of the crystal QM15.

captured in channeling states over an angular range of more than 70 μrad, much larger than $\theta_c = 15$ μrad. Moreover, the deflection angle increased with the crystal orientation, a behavior explained by the multi-turn effect that extends the angular acceptance for channeling.

Crystal QM15 was installed in its angular actuator with excessive horizontal inclination with respect to the beam reference axis. The consequence was that planar channeling was active in an angular range just at the edge of the range permitted by the actuator, as shown in Fig. 19. Because of this, the crystal was only marginally effective for collimation studies. Such an observation was correlated to a tiny crystal misalignment induced by the vacuum, later taken into account during crystal installation.

The imperfect alignment of the crystals STF9 and QM15 demonstrated how important is the integration of the crystal in its angular actuator. The optimal integration recipe consisted in requiring that, in the central orientation of the actuator, the face and the planes of crystal should follow as closely as possible the geometrical reference of the beam envelope. Appropriate high-precision optical devices were added in the SPS tunnel to ensure the required alignment with an accuracy of the order of 100 μrad.

The angular scans of the crystals STF9 and QM15 exhibited a special feature, illustrated in Fig. 20, in which the scan of each crystal is plotted with the channeling peak shifted at the origin of the angular scale. In both cases, the VR regions had a secondary minimum around 200 μrad. This minimum, foreseen by computer simulation,[24] was at an angle about equal to the bend angle for both crystals. Its explanation is that when the downstream end of the crystal is almost tangential to the beam envelope, the VR event may occur along the whole crystal arc. In these conditions, the repeated angular kicks due to multi-turn VR events always increase

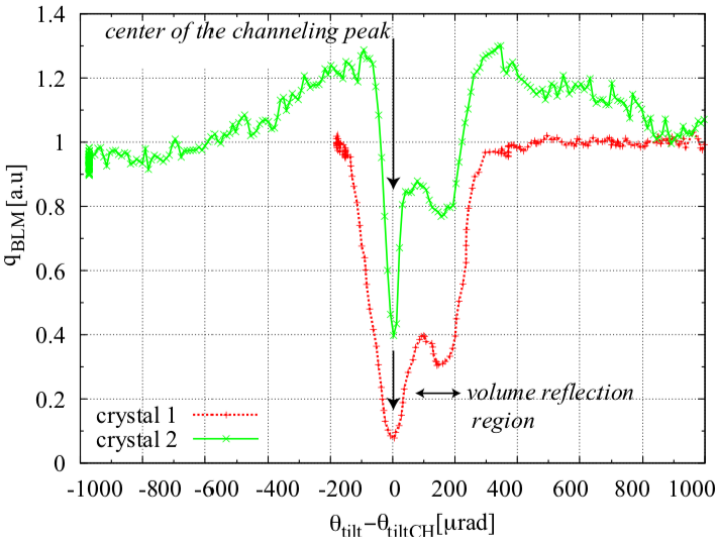

Fig. 20. (Color online) Angular scans of crystals STF09 (in green) and of the QM19 (in red). The plots are shifted to have the channeling peaks at zero angle.

the oscillation amplitudes of particles, allowing them to intercept the absorber more quickly and hence reducing the integrated flux rate. In other crystals, the secondary minimum at the end of the VR range was sometimes not detected during the scans. This could have been caused by some crystal torsion producing a smoothing of the secondary minimum, because of the different orientations of the crystal planes along the vertical direction or of the different deflections for different vertical slices of the crystal. Instabilities of the goniometer or of the circulating beam could also have caused a smoothing of the main and the secondary loss minima.

5.3. *Experiments in crystal-collimation configuration*

The crystals QM25 and STF18, shown in Figs. 21 and 22 respectively, provided extensive information on crystal-particle interactions and on the features of crystal collimation in circular accelerators. For the sake of concision, we report in detail the results recorded with crystal STF18 and restrict ourselves to a synthetic overview of other crystal results in the subsequent subsections.

Crystal collimation was conceived to improve the cleaning efficiency, in the optimal crystal orientation for channeling, by reducing the rate of nuclear and diffractive interactions in the cleaning section and thus limiting the flux of background particles with reduced energy that escape from the cleaning section. Indeed, off-momentum particles not intercepted by the absorber with $\delta = p/p_0 - 1 \neq 0$, where p is the particle momentum and p_0 is the momentum of the synchronous particle, would perform an orbit deviation $x_\delta = D_x(z)\delta$ as they progress in the HD region. Because of the increase of horizontal dispersion, particles could be lost in

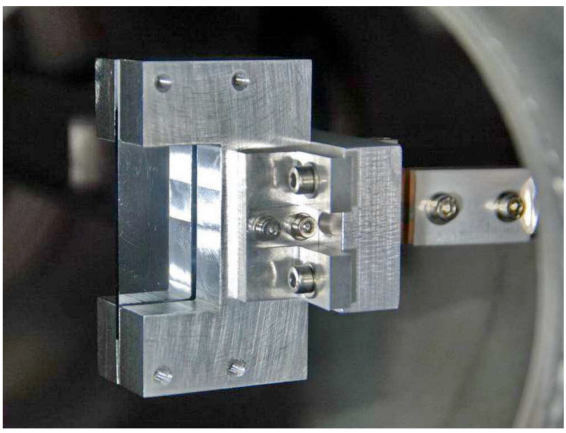

Fig. 21. Crystal QM25.

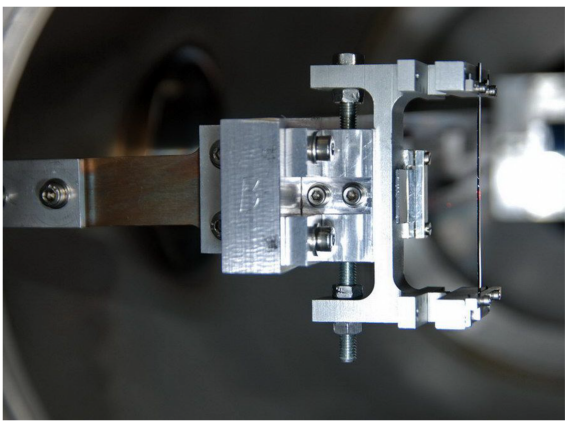

Fig. 22. Crystal STF18.

the vacuum pipe, eventually creating radiation hot-spots, particularly harmful for the accelerator integrity.

Experiments to measure the loss rates and their reduction factor from amorphous to channeling orientations (R_{loss}) were carefully planned and performed with proton and lead ion beams in the SPS, at two different storage energy levels, 120 and 270 GeV.[26] The losses were mapped not only near the crystal but also in the subsequent high-dispersion region (HD-area) and whenever possible in the entire accelerator ring. The relevant UA9 devices involved in the experiments were the crystal (the STF18, conventionally called Cr4, located upstream of the IHEP goniometer was the most often used) and the massive absorber, corresponding to the 60 cm long tungsten block called TAL1, located in the TACW.51998 UA9 vacuum tank in the cleaning section. To evaluate the loss rates downstream of the crystal,

Table 4. Betatron functions of the crystal-collimation test based on crystal STF18.

Element	β_x [mm]	σ_x [m]	$\Delta\Phi_x$	D_x [m]
Cr4 (STF18)	76.16	0.956	0	-0.786
TAL1 (Absorber)	87.68	1.026	0.248	-6×10^{-4}
TAL2	90.43	1.042	0.491	3.402
RP3 (Timepix)	99.03	1.09	0.495	3.592

BLM4 was used (see Fig. 5). The TAL2 and the Roman pot 3 (RP3), hosted in the HD area, were used to perform linear scans, evaluated by the irradiation of the subsequent loss monitors BLM5 and the BLM7 (see Fig. 6). The operational values of the betatron functions of some of those devices are listed in Table 4. The TAL2, made of 10 cm long movable block, initially of duralumin and later of tungsten, was also used to limit the accelerator aperture in the HD area. Off-momentum particles emerging from the cleaning section and interacting with the TAL2 produced secondary particles, detected by beam loss monitors BLM5 and BLM7 downstream. The counting rate of these BLMs was used to rapidly estimate off-momentum halo intensity, predominantly intercepted by TAL2 in fixed position, limiting the momentum aperture. As an alternative, the aperture restriction was obtained using the 3 cm long stainless steel edge of RP3, in particular with ion beams to reduce the interaction cross-section.

In Fig. 23, four angular scans made with the STF18 crystal are shown. The two scans in the top row were made with 270 GeV proton beams, while the two in the bottom row were made with 270 GeV/u lead ion beams. The two plots (a) in the left column were recorded by the BLM downstream of the crystal, while the two plots (b) in the right column were collected by the BLM in the HD area. Curves 1 refer to the experimental data. Curves 2 show simulation results based on the model in Ref. 56, taking into account synchrotron oscillations and the effect of miscut angle between crystal surface and (110) crystallographic planes. During proton run, the crystal and the TAL positions were $X_{\mathrm{STF18}} = 5.6$ mm ($9\sigma_x$) and $X_{\mathrm{TAL1}} = 8.92$ mm ($13.5\sigma_x$), respectively, with a gap $\Delta X = 2.89$ mm ($4.4\sigma_x$), evaluated at the TAL1 azimuth (σ_x indicates the local value of the horizontal RMS beam size). In practice, the gap ΔX indicates the horizontal shift of the TAL from the crystal, weighted by the betatronic functions at their respective azimuthal positions. The measured beam loss reduction factor was $R_{\mathrm{STF18}} = 20$ near the crystal and $R_{\mathrm{HD}} = 6$ in the HD area. The latter value was obtained by positioning the TAL2 at $X_{\mathrm{TAL2}} = 41$ mm, to avoid potential conflict with the hierarchical role of the crystal and the absorber positions in the cleaning section. Similar measurements were also made with 120 GeV/c protons. The crystal and TAL1 positions were not identical to those of the 270 GeV proton run. They were slightly different in terms of real coordinates, but more different in terms of σ_x, because of the beam size variation with energy. The chosen positions were $X_{\mathrm{STF18}} = 4.6$ mm ($4.8\sigma_x$),

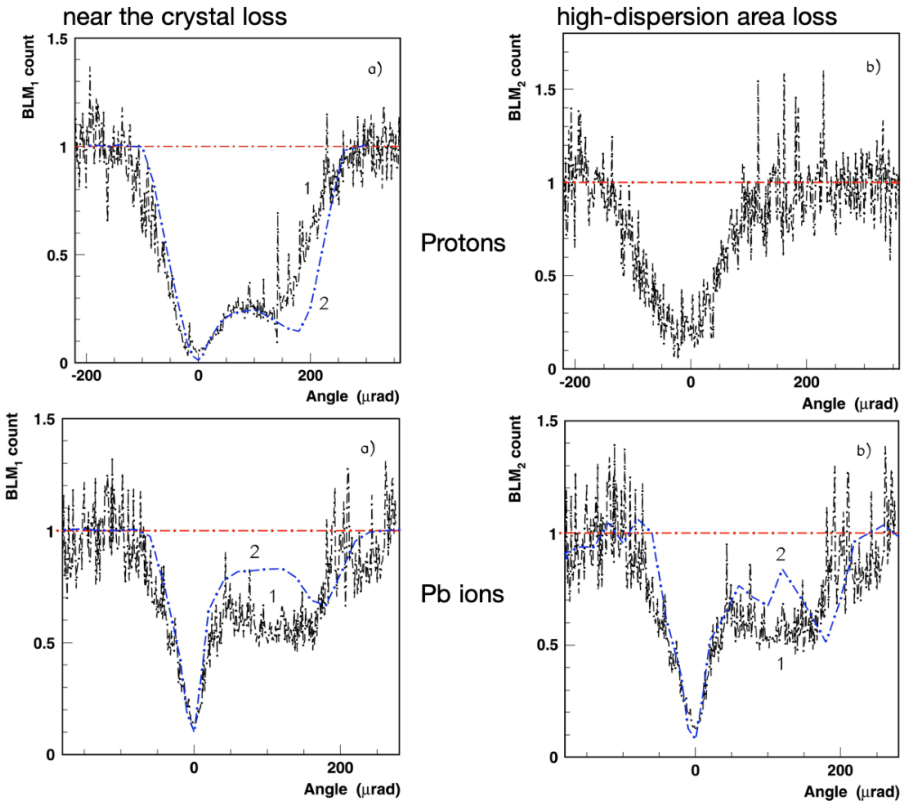

Fig. 23. (Color online) Local losses recorded during crystal angular scans (black) and simulated loss pattern (blue). Both are normalized to their own amorphous level. Both proton (top row) and lead ions beams (bottom row) are presented. Specific focus is made on losses at crystal location (left column) and in the high-dispersion area (right column).

$X_{\mathrm{TAL1}} = 7.2$ mm ($7\sigma_x$) and $\Delta X = 2.3$ mm ($2.24\sigma_x$). The measured loss reduction factors were $R_{\mathrm{STF18}} = 10$ at the crystal and $R_{\mathrm{HD}} = 4.5$ in the HD area. The worsened performance at reduced beam energy was, in our interpretation, caused by the smaller gap ΔX selected and by larger MCS angular kicks imparted to the particles not in channeling states, both contributing to reduce the probability of multi-turn channeling and to increase the loss in the amorphous crystal orientation, thus to decrease R_{loss}.

A multi-bunch proton beam made of a train of 48 bunches spaced by 25 ns was injected and stored at 270 GeV to provide higher circulating intensity and therefore higher loss rate, during angular scans. This made it possible to measure the loss reduction rate in regions of the SPS far from the crystal where the sensitivity of the BLMs is not sufficient to detect loss of a single bunch. Figure 24 shows the beam loss ratio detected by a large number of standard BLMs located near each main quadrupole spaced by 32 m in the SPS circumference.[26] The reduction factor

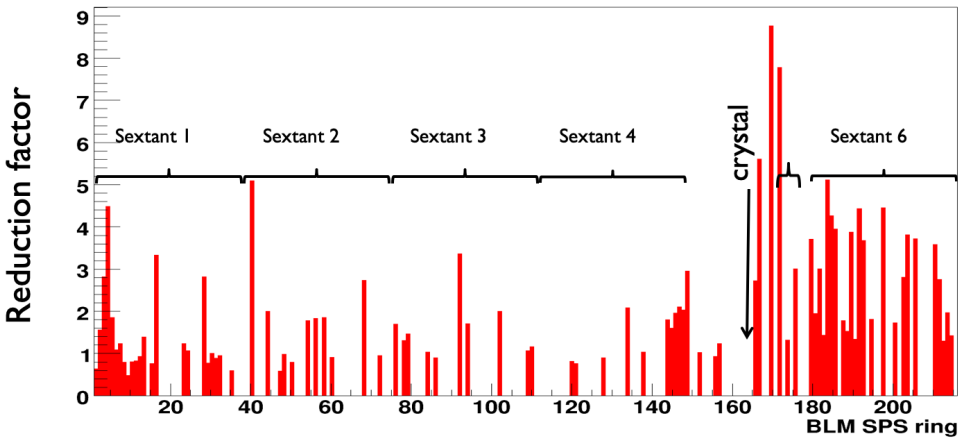

Fig. 24. Loss reduction factor over the SPS ring.

$R_{\rm loss}$, recorded by a standard BLM, was always larger than 1. It was particularly large along the sextant 6 that follows the straight section in the sextant 5, where the cleaning system was located.

The experimental observation that, with proton beams of 270 GeV, $R_{\rm HD}$ was considerably smaller than $R_{\rm STF18}$, although unexpected, could be explained with the following arguments. The 60 cm long tungsten bar, used as the secondary collimator-absorber, was insufficient to absorb the full beam of 270 GeV halo protons. Because of the nuclear inelastic cross-section $\sigma_{\rm in} = 1.725$ b,[57] the interaction length was $S_{\rm in} = 9.18$ cm and the attenuation probability $P_{\rm in} = \exp(-L/S_{\rm in}) = 1.45 \times 10^{-3}$. Protons emerging from the absorber with reduced momentum, because of diffractive scattering events and/or ionization loss, contributed to irradiate the TAL2, used to restrict the momentum aperture of the HD area. Such a mechanism leads to overestimating the off-momentum loss at the TAL2 and to underestimating the cleaning efficiency achievable with crystal collimation. A 1 m long tungsten absorber, with an attenuation probability $P_{\rm in} = 1.86 \times 10^{-5}$ would have been sufficient to solve the issue.

Experiments with Pb ion stored beams of 270 GeV per charge produced, among others, the results in the bottom row of Fig. 23. The emittance was $\epsilon_h = \epsilon_v = 11 \times 10^{-9}$ m $\cdot$ rad and the RMS bunch length $\sigma_t = 0.55$ ns. Although the crystal channeling has the same behavior for protons and Pb ions with the same momentum per unit charge $p_z = p/Z$, interactions with the crystal are very different, in particular because of the considerably different ionization losses, proportional to Z^2. During the data-taking runs with 270 GeV/u lead ion beams, the average value of the energy loss was about 7 GeV per STF18 crystal traversal. This caused a strong orbit shift, an increase of the oscillation amplitude and the ion debunching from the RF bucket in only three crystal passages. The beam attenuation length, governed by a total cross-section $\sigma_{\rm tot} \approx 6$ b, more than 10 times

larger than for protons of 270 GeV, was about 3.5 cm along the crystal. In the bottom row of Fig. 23, curves 1 show the beam loss evolution during the angular scan, recorded downstream the crystal (plot (a)) and in the HD area (plot (b)). The crystal and the TAL positions were $X_{\mathrm{STF18}} = 3.1$ mm ($3.4\sigma_x$) and $X_{\mathrm{TAL}} = 6.9$ mm ($7\sigma_x$). The gap between them at the TAL azimuth was $\Delta X = 3.6$ mm ($3.6\sigma_x$). The RP3, used to limit the aperture in the HD area, was positioned at a distance $X_{\mathrm{RP3}} = 35.7$ mm, to avoid interference with the cleaning process. The loss reduction was $R_{\mathrm{STF18}} \approx R_{\mathrm{RP3}} \approx 7$, i.e. almost the same downstream the crystal and in the HD area. This result was interpreted as a strong indication that the off-momentum halo is predominantly formed in the crystal rather than in the TAL, the survival of the Pb ions and of their fragments from the traversal of the TAL being prevented by the large inelastic nuclear interaction cross-section. Curves 2 show the simulation results and describe sufficiently well the experiment near the channeling minimum.

5.4. *The role of dispersion in the UA9 optical layout*

In Fig. 25, the dispersion function and the phase space advance between some of the UA9 components, i.e. the crystal, TAL1, BML5 and BLM7, are indicated. As discussed in the previous subsection, off-momentum particles, escaping from the cleaning region, have the highest probability to be lost in the subsequent HD region and in particular close to the azimuths of BLM5 and of BLM7, where the dispersion function reaches the two peak values $D_x = 3.8$ m and $D_x = 4.6$ m, respectively. Moreover, at the BLM5 position, the phase advance is $\Delta\Phi \approx 180°$ from the crystal

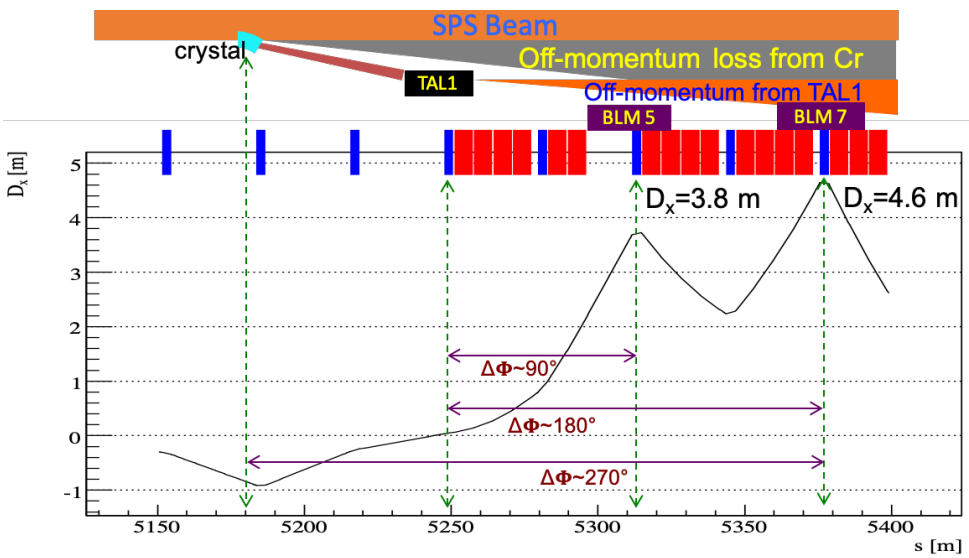

Fig. 25. Shape of the dispersion function in UA9.

azimuth and $\Delta\Phi \approx 90°$ from the TAL1 azimuth, while at the BLM7 the phase advance is $\Delta\Phi \approx 270°$ from the crystal azimuth and $\Delta\Phi \approx 180°$ from the TAL1 azimuth. Off-momentum particles produced at the crystal will be deflected by a combination of dispersive orbit and betatron oscillations toward the BLM7, while the effect of the betatron oscillations is almost canceled at the BLM5. Conversely, off-momentum particles produced at the TAL1 are deflected more toward the BLM5 and less toward the BLM7 positions.

To exploit these features of the UA9 optical layout, another crystal-collimation test was performed, in which the silicon strip crystal STF81 was used as primary collimator.[28] The crystal parameters, reported in Table A.1, were $L = 1.87$ mm, $\theta_b = 165$ μrad and $\theta_m \approx 10$ μrad, all of them in principle, more appropriate to favor capture into channeling states. The test beam was composed of 12 bunches of 270 GeV protons, with a total intensity of 1.3×10^{12} particles. After the alignment procedure, the crystal and the absorber were placed at a distance $X_{\mathrm{STF81}} = 4$ mm ($4.5\sigma_x$) and $X_{\mathrm{TAL1}} = 7$ mm ($7.94\sigma_x$) from the orbit, respectively. The crystal-absorber offset was $\Delta X = 3$ mm. None of the targets limiting the accelerator aperture in the HD area were used, to permit the direct loss of off-momentum particles into the SPS vacuum pipe and the generation of secondary debris as close as possible to the monitors BLM5 and BLM7.

The results of a typical angular scan are reported in Fig. 26. In the left plot, curve (1) represents the loss profile recorded by BLM4 downstream the crystal STF81. The left minimum corresponds to the optimal orientation for channeling. The beam loss reduction is $R_{\mathrm{STF81}} = 11.8$. Curve 2 shows the number of the nuclear inelastic interactions in the crystal, obtained by a simulation based on the model in Ref. 58. Particles were tracked until they hit the TAL or an inelastic nuclear interaction occurred in the crystal. The calculated dependence describes well the width and the shape of the overall experimental data scan, while it provides smaller values of beam losses for channeling and VR orientations of the crystal. Curve 3 shows the multi-turn simulation results based on a Monte Carlo crystal routine[59] and on the SixTrack code to transport the particles in the SPS. The diffractive scattering of protons was accurately included. In this case, the calculated width of

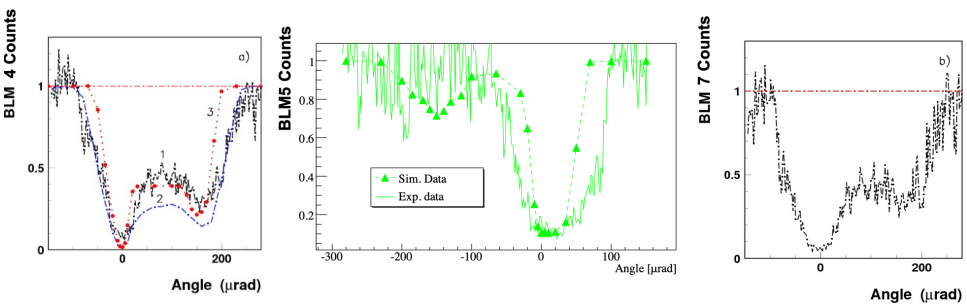

Fig. 26. (Color online) Angular scan with the crystal STF81.

the overall angular shape is smaller than that of the experimental data, the losses in channeling orientation are also smaller than the measured ones, while the loss value in the VR region is in better agreement.

In the central plot (in green) of Fig. 26, the beam loss profile recorded by the BLM5 in the HD area is shown. The beam loss reduction was $R_{\mathrm{BLM5}} = 8.3$, thus smaller than downstream the crystal as in the previous experiments. The green triangles, connected by a dotted curve, are the result of a simulation based on the crystal routine in Ref. 59 and on the SixTrack code. The agreement with the data is satisfactory in channeling orientation and fair in other angular ranges.

The right plot of Fig. 26 shows the beam loss shape as a function of the crystal orientation observed by BLM7. The angular dependence is the same as downstream the crystal. The beam loss reduction in channeling instead is considerably larger, $R_{\mathrm{BLM7}} = 18.1$. The reduction values of the proton losses on the beam pipe obtained by the simulation with the SixTrack code are 9.1 and 20.1 at the crystal and at BLM7, respectively. The large loss reduction at the BLM7 was essentially due to the reduced flux of off-momentum particles emerging from the TAL1 that could reach the BLM7 area. These particles were predominantly lost near the first dispersion maximum and the BLM5, where the betatron phase advance from the TAL1 is about 90°. In fact, protons in channeling regime, deeply deflected inside the TAL1, have a betatron amplitude of about 15 mm at the TAL1 entrance face. The fraction of protons not stopped by the TAL1 and emerging from it, exhibit an additional RMS deflection $\theta_{\mathrm{ms}} = 0.742$ mrad, due to MCS, taking into account the nuclear elastic scattering, and a relative energy loss $\delta = -7.62 \times 10^{-3}$ on average, due to ionization. At the TAL1 exit, the betatron amplitude is $X_m = 68.6$ mm (on average). At the QF.52210 azimuth, it is $X_m = 75$ mm, while the average orbit shift due to $\delta \times D_x$ is $X_\delta = -28.75$ mm. In average, the full orbit shift due to the combined effect of betatron and synchrotron motion, is larger than the horizontal half-size of the SPS beam pipe in the QFs quadrupoles of 76 mm. Thus, the largest fraction of particles deflected by the crystal not intercepted in TAL1 should be lost in the pipe just upstream of BLM5 and should not affect the BLM7.

5.5. *Comparing dispersive losses of proton and lead ion beams*

The crystal QM15 was used for measurements similar to those of STF18 reported earlier. In particular, comparisons were performed of the losses near the crystal and in the HD area, with protons and lead ions at 270 GeV/u.[25] The loss reduction factor R_{loss} was measured using angular scans. Downstream the crystal, R_{loss} varied from 5–9 for proton beams and from 3–3.5 for ions, depending on the gap ΔX imposed between the crystal and the absorber horizontal positions. In the HD area, R_{loss} varied from 1.5–5 for protons and was about 3.5 for ions. The multi-turn efficiency, evaluated with linear scans of the LHC phase 2 collimator, varied from 60 to 70%. Additional linear scans were performed using the TAL2 and the BLM5, to record the off-momentum particles escaping into the HD area. A typical scan made

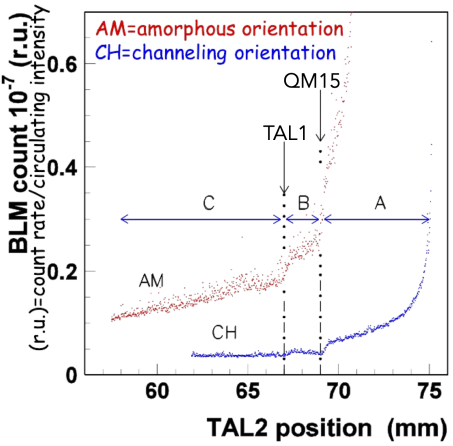

Fig. 27. (Color online) Linear scans of the TAL2 in CH and AM orientations of the crystal QM15.

with 270 GeV proton beams in CH (blue curve) and in AM (red curve) orientations is shown in Fig. 27, where the BLM counting rate, normalized to the circulating beam intensity, is plotted as a function of TAL2 position. The two positions indicated with arrows and dot-dashed vertical lines, denote the shadow of QM15 and of TAL1 at the azimuth of TAL2. In the range A, from 69–75 mm, the TAL2 interacted with the beam tails, populated by particles with large betatron and synchrotron amplitude oscillations. Such area was more rapidly depleted by orienting the crystal in optimal channeling mode, because of the reduced back-scattered flux of particles. The range B, from 67–69 mm, was populated by particles deflected by MCS during the crystal traversal. In channeling orientation, such population of particles was strongly reduced, while in amorphous orientation the depletion rate was much slower because of the small MCS deflection per crystal encounter. The range C, for positions smaller than 67 mm, was populated by off-momentum particles escaping from cleaning area. The reduced population in channeling orientation indicated the reduced probability of nuclear interactions in the crystal and at the TAL edge. The shape of the counting rate around the CR3 and the TAL positions could be interpolated by an error function, the derivative of which indicated the population of off-momentum particles emitted by the crystal and by the internal edge of the TAL, respectively. The latter was considerably larger in AM mode because of the reduced impact parameter of the particles deflected into the TAL by repeated MCS deflections much smaller than the channeling deflection.

5.6. *Optimization of the crystal-collimation configuration*

The main beneficial aspects of crystal-assisted collimation are the reduced production of particles with decreased momentum and their more efficient confinement in the cleaning section. Channeled particles have reduced nuclear interaction cross-section, larger deflection angle, greater impact parameter with the massive

absorber and reduced probability of being scattered back into the beam. The flux of particles escaping from the cleaning area strongly depends on the gap size ΔX between the crystal and the absorber. A larger gap favors the multi-turn channeling process, because particles not captured in channeling states have reduced probability of interaction with the absorber and larger probability of interacting again with the crystal and of being captured in channeling states. Conversely, the impact parameter of channeled particles with the absorber is reduced, therefore their probability of back-scattering toward the circulating beam increases. In these conditions, an optimal value of the size of the crystal-absorber gap that minimizes loss reduction rate R_{loss} is expected to exist. Experiments performed to find it are briefly reported.

Measurements were performed on crystal-collimation setup using the crystal STF18 as primary collimator, with 270 GeV/u proton and Pb-ion beams. The results are summarized in Fig. 28.[27]

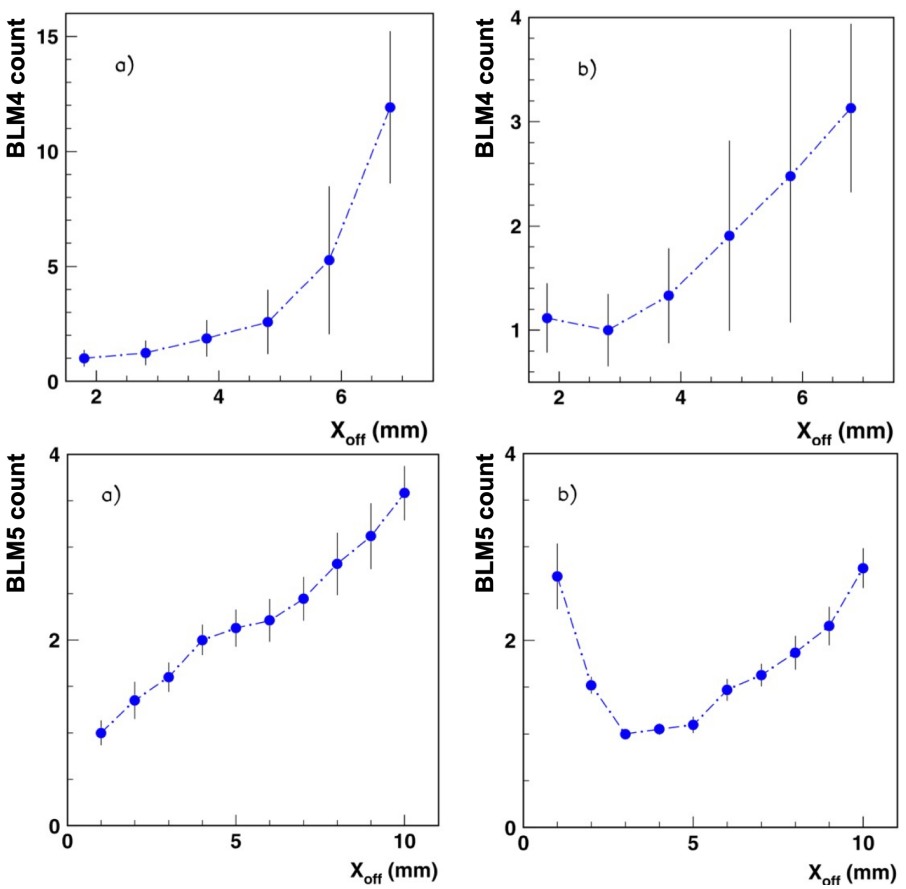

Fig. 28. Loss rates as a function of the gap between the crystal and the absorber.

Experiments with proton beams of 270 GeV consisted, first, in positioning the crystal at $X_{\mathrm{STF18}} = 3.0$ mm and then in orienting it at the optimal angle maximizing the halo channeling. Initially, the TAL1 was positioned at $X_{\mathrm{TAL1}} = 4.84$ mm, with an offset $\Delta X = 1.8$ mm, while the TAL2 in the HD area was positioned at $X_{\mathrm{TAL2}} = 25.4$ mm from the beam orbit. The beam losses produced in the aligned crystal and in TAL2 were measured as the TAL1 distance from the orbit was increased up to 6.4 mm. The plots in the top row of Fig. 28 show the observed beam loss dependence on TAL1 offset value ΔX (called X_{off} in the plots). The plot (a) shows the losses downstream the crystal, recorded by BLM4. The plot (b) indicates the losses downstream of TAL2, recorded with BLM5. The large fluctuations around the experimental points were due to large beam instabilities, during the specific data-taking run reported. Beam losses downstream the crystal rapidly increased with the offset, while in the HD area, a minimum was detected at $\Delta X = 2.8$ mm, as shown in the top plot (b). Smaller offsets of about 1 mm were investigated in other data-taking runs, not reported here. They confirmed the increase of beam losses for $\Delta X < 1.8$ mm. We may thus conclude that for protons the collimation leakage has a broad minimum for $\Delta X \approx 2.5$–3.0 mm.

In experiments with stored beams of 270 GeV/u Pb ions, 10 bunches, separated by 200 ns with average population of about 1.1×10^8 ions per bunch, were injected and stored to increase the loss rates in the BLMs downstream the crystal and in the HD area. Initially, the crystal STF18 and the TAL1 were placed at distances $X_{\mathrm{STF18}} = 2.8$ mm ($3.55\sigma_x$) and $X_{\mathrm{TAL1}} = 12.8$ mm ($16.34\sigma_x$) from the orbit, respectively. The TAL1 offset relative to the crystal was $\Delta X = 10$ mm. The tungsten scraper TAL2 in the HD area was placed at a distance $X_{\mathrm{TAL2}} = 25.4$ mm from the orbit to increase the beam losses detected with BLM downstream. Once the optimal crystal orientation for channeling had been chosen, the beam losses were measured for different distances of TAL1 from the orbit. The results are shown on the bottom row of Fig. 28. The beam losses observed in the crystal (a), and in the HD area (b), were strongly dependent on the value of the TAL1 offset. The losses in the crystal monotonically increase by a factor 3.5, when the offset increases from 1 mm to 10 mm, while the losses in the HD area have a minimum for $\Delta X \approx 3$–5 mm. In the range explored, a loss increase by a factor about 3 was observed.

The measurements reported show that the collimation leakage is minimal for some value of the crystal-absorber offset. The optimum value is 2–3 mm for protons and 3–5 mm for Pb ions with $p_z = 270$ GeV/c. Although the crystal channeling characteristics are the same for protons and Pb ions with the same momentum per charge, the difference in the optimal offset is caused, as already mentioned,[5,6] by the considerably larger ionization losses of Pb ions, which are proportional to Z^2 and whose average value in the crystal traversal is about 7 GeV. As a consequence, the offset should be larger for Pb ions, to comply with the larger synchro-betatron oscillation amplitudes at the exit of the crystal and to permit multi-turn channeling mechanism to operate efficiently. The optimal offset should decrease with the

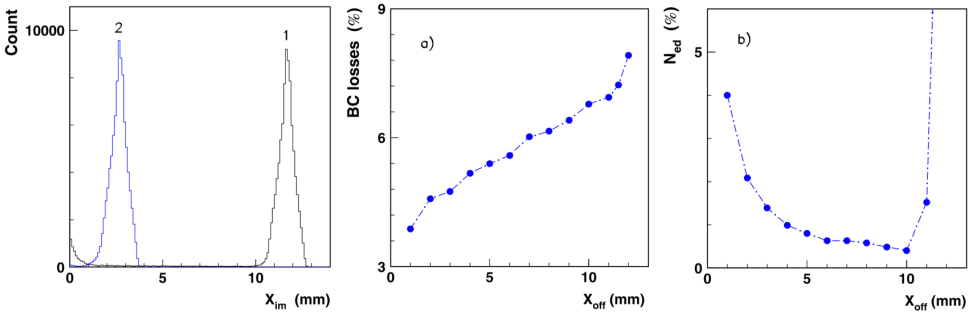

Fig. 29. (Color online) Simulation of the beam loss for the ion beam.

increase of particle energy, because of the smaller MCS angle and of the reduced ratio of the ionization energy loss by the beam energy. The efficiency of crystal collimation is maximal when the optimal crystal-absorber offset is chosen.

Simulations of the Pb-ion behavior, based on the model in Ref. 56, taking into account synchrotron oscillations of particles and effect of the miscut angle between the crystal surface and the (110) crystallographic planes, were performed and their results compared to experimental observations. Off-momentum losses were more relevant for ion beams. As already mentioned, there are three basic mechanisms of producing off-momentum particles. They can emerge from diffractive and nuclear interactions during the crystal traversal in amorphous or VR orientation. They can result from channeled particle ionization energy losses and diffractive nuclear scattering at the edge of the absorber and eventually be scattered back toward the circulating beam, instead of being absorbed. The simulation results, summarized in Fig. 29, helped in clarifying the interplay of these effects. In the three plots the edge of the beam envelope and the crystal inner face were both at the origin of the x-axis, while the inner face of TAL1 was shifted in the range from 1–10 mm. The left plot shows the horizontal distributions of the impact parameters onto the TAL1, for the two extreme values $\Delta X = 1$ mm (curve 1 in black) and 10 mm (curve 2 in blue). In the third curve of the plot (in black), the counts decrease rapidly in a couple of mm, starting from the origin, and represent the distribution of the halo particles that have had either amorphous or dechanneling interaction with the crystal and have been deflected inside the gap region. These particles have the possibility of performing additional passages through the crystal. In this case, they can be either deflected into the channeling regime into the TAL1, or they can be lost by inelastic nuclear interactions in the crystal. Moreover, for smaller offset values, some of the halo particles never captured in channeling states may repeatedly interact with the crystal, being finally deflected by MCS into the edge of TAL1, sometimes producing off-momentum particles that may be scattered back into the beam. For the large offset value instead, the crystal-absorber gap is practically empty at the TAL1 edge. The central and the right plots of Fig. 29 shows the calculated dependence on ΔX

of the number of inelastic nuclear interactions of Pb ions in the crystal, plot (a), and the fraction of particles hitting TAL1 with an impact parameter smaller than 0.5 mm, plot (b). The former is increased and the latter reduced as a function of ΔX. In comparing plot (a) in the bottom row of Fig. 28 with plot (a) in Fig. 29, we observe that the interaction number increase in the simulation is smaller than the beam loss increase in the crystal, observed in the experiment. The discrepancy may be explained by the fact that particles with large momentum reduction produced in nuclear interactions are not considered in the simulation. They also contribute to interactions with the crystal in the subsequent turns. Our simulation confirms that the number of particles with large momentum reduction produced in the TAL1 should decrease, whereas that produced in the crystal should increase, with the increase of absorber offset. From the observed dependence of beam losses in the HD area we may conclude that collimation leakage occurs mainly in the TAL1 edge for small offset values, while for large ones it originates in the crystal. As a result, the leakage has a minimal value as a function of the offset.

5.7. *Effect of the miscut angle*

The miscut angle θ_m is an important parameter for bent crystals inserted in circular accelerators. Its value is positive, if crystal planes are inclined to the side of the crystal bend along beam direction, as shown in Fig. 30, and negative in the opposite case.

If $\theta_m < 0$, there is a special value $b_{\rm lim}$ of the impact parameter that discriminates in two groups the trajectories of the particle in channeling states. Halo particles hitting the crystal with $b < b_{\rm lim}$ follow shortened channels and are deflected by angles smaller than θ_b, insufficient to bring them into the secondary absorber. Instead, particles with $b \geq b_{\rm lim}$ follow the channels over the entire crystal length and are deflected by the angle θ_b. The resulting particle population inside the crystal-absorber gap is strongly increased and the collimation efficiency reduced. For this reason, only crystals with $\theta_m > 0$ have been selected as primary crystal collimators in the UA9 experiment.

If $\theta_m > 0$, the optimal alignment for channeling is rotated by θ_m in comparison with that of a perfect crystal, as shown in Fig. 30. The side effects of changing the crystal orientation are three. The crystal touches the beam periphery at point B of its exit face. The crystal planes are parallel to the beam envelope (the dot-dashed line touching the crystal on the left) at its entrance face AC. A halo particle, entering the crystal through the side face AB, with an impact parameter b, encounters inclined crystalline planes and traverses the crystal as an amorphous material. The inclination is maximal for $b = 0$ and gradually decreases as b approaches the value of the crystal side-face projection $\Delta = R(\cos(\theta_m - \theta_b) - \cos\theta_m)$. Particles with $0 < b < \Delta$ acquire some amplitude increase due to multiple scattering during the first crystal traversal and can enter the crystal next time during following turns through its entrance face AC and be captured into channeling. Such a mechanism increases

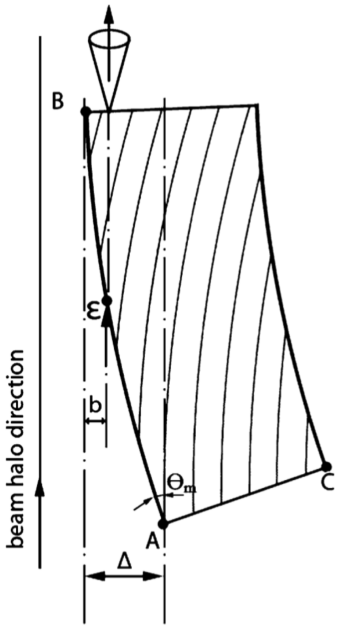

Fig. 30. Miscut angle in a realistic crystal.

the loss due to inelastic interactions beyond the amount expected in perfect crystal, thereby worsening the beam loss reduction rate R_{loss} from amorphous to channeling orientation. The decrease of R_{loss} due to the crystal miscut depends on the ratio between the impact parameter value b in the first hits and the value of the AB face projection Δ.

The crystal STF18, with $\theta_m = 200$ μrad and $\Delta = 0.224$ μm, well illustrates the effect of too large miscut angle on crystal collimation.[26] Data were collected using a single-bunch proton beam of 1.15×10^{10} particles, with 1.2×10^{-8} rad $\cdot$ m emittance, stored at 120 GeV energy. In the experiment, the crystal and the TAL1 were positioned at $X_{\text{STF18}} = 4.6$ mm ($4.8\sigma_x$) and $X_{\text{TAL1}} = 7.2$ mm ($7\sigma_x$), respectively. The gap between them at the TAL1 azimuth was $\Delta X = 2.3$ mm ($2.24\sigma_x$). The RP3, in the fixed position $X_{\text{RP3}} = 8.93$ mm ($8.2\sigma_x$), was used to intercept off-momentum particles in the HD area. The projection of TAL1 at the RP3 azimuth was $X_{\text{TAL1}}(\text{RP3}) = 7.65$ mm, therefore RP3 was in the shadow of TAL1, but only for very small values of the relative momentum deviation δ.

Figure 31 shows the result of an angular scan. The upper plot (a) shows the beam losses downstream crystal STF18 and the lower plot (b) those downstream the HD area target. Curves 1 correspond to the data, whilst curves 2 provide the dependence of the number of inelastic nuclear interactions of protons in the crystal as a function of the orientation angle, obtained by simulation accounting for crystal miscut and synchrotron motion. BLM_1 count in plot (a) is the rate of the scintillation

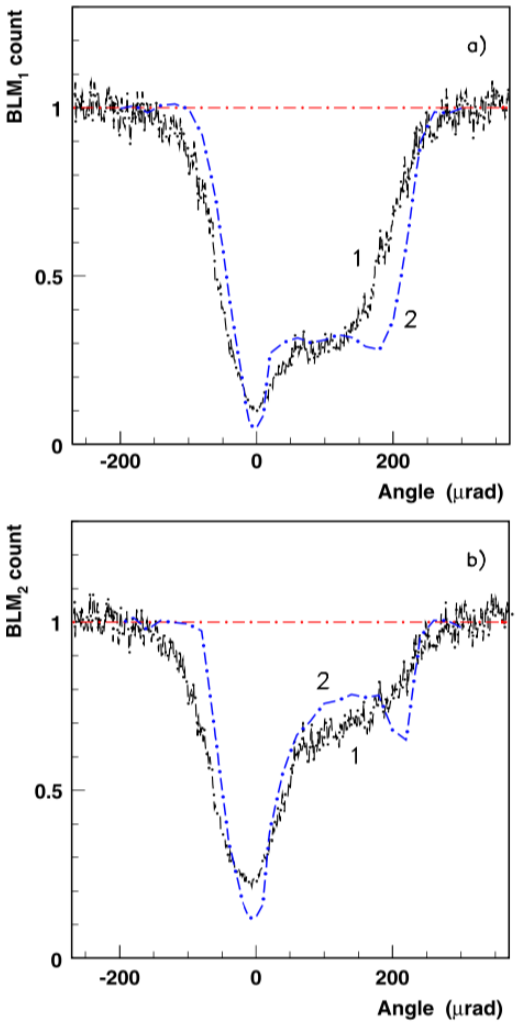

Fig. 31. (Color online) Angular scan of the crystal SFT18.

telescopes B–L, whilst BLM_2 count in plot (b) corresponds to the rate of the telescope J–K (the two telescopes are shown in Figs. 5 and 6, respectively). Each BLM count is normalized to its value for the amorphous orientation (dot-dashed red line) and plotted as a function of the angular position of crystal STF18. The measured beam loss reduction was $R_{\mathrm{SFT18}} = 10$ downstream the crystal and $R_{\mathrm{HD}} = 4.5$ in the HD area. A simulation not taking into account the miscut effect would have predicted $R_{\mathrm{SFT18}} = 32$, a result with a too large discrepancy from the data. In order to improve our prediction, two effects were accounted for in the simulation code: the crystal miscut angle and the average diffusion speed of particles in the halo periphery. The latter was evaluated experimentally by scraping the halo with

TAL near the crystal distance from the orbit and by measuring the average time required to repopulate the gap. The measured growth rate was $\lambda = 2.2$ μm/s. Using the extended simulation model, the distribution of the impact parameter with the crystal could be evaluated: the average value was $b = 0.28$ μm and the full width was about 1 μm. Because of the miscut angle, the first hit happened on the side face AB of the crystal for about half of the particles, the beam loss rate at perfect alignment was almost doubled and the beam loss reduction was $R_{\mathrm{SFT18}} = 21$ downstream of the crystal and $R_{\mathrm{HD}} = 8.4$ in the HD area. The discrepancy compared to the experimental data was reduced to about a factor two, an estimate significantly better than that not including the miscut angle and the average diffusion speed. The beam loss level in the VR region was in good agreement with experiment, as well. It should be noted that while the effect of the crystal miscut considerably modified the beam loss prediction in the aligned crystal, it affected in a negligible manner the channeling efficiency at perfect alignment that was estimated to be $P_{\mathrm{ch}} = 93.2\%$ and 91.4% for cases a) and b) shown Fig. 31, respectively.

The extended simulation model also suggested that the choice of the radial position of RP3 was not optimal in this collimation experiment. In fact RP3 was in the shadow of the TAL and the crystal, but not for the whole halo. The halo particles with large momentum deviations $\delta > 10^{-3}$ could have first hit the RP before touching the crystal. According to the simulation the contribution of such particles was about 5%. The background level of losses produced in RP3 by large off-momentum particles affected the collimation mechanism and artificially reduced the values of R_{SFT18} and R_{HD} observed both downstream the crystal and in the HD area. To avoid such an artifact, RP3 should have been put in the shadow of the crystal for all particles of the bunched beam. To obtain this, the RP3 distance from the orbit should be $X_{\mathrm{RP3}} > X_{\mathrm{STF18}} \cdot (\beta_{\mathrm{RP3}}/\beta_{\mathrm{STF18}})^{1/2} + D_x \cdot \delta = 11$ mm, where $\delta = 1.615 \times 10^{-3}$ is the bucket half-height.

The crystals STF18 and STF81 have very similar lengths and bending angles, while their miscut angles differ by a factor 20 (see Table A.1). They were used for a direct comparison of their performance and to possibly corroborate the simulation findings. During the same data-taking run, the two crystals were used in crystal-collimation mode, in a proton beam of 1.1×10^{11} particles made of a single bunch, stored at 270 GeV. The horizontal emittance was 10^{-9} m $\cdot$ rad. Each crystal was tested separately, using the same configuration. The crystal was positioned at 5σ and TAL1 at 8σ from the beam center. The beam losses downstream of the crystal, recorded during the angular scans, are normalized and plotted together in Fig. 32. As foreseen, the losses of the crystal STF81 are slightly lower than that of the crystal STF18, in the optimal alignment for channeling, while they are practically the same in VR orientation. This means that it is very challenging to observe a clear effect of miscut angles as large as 200 μrad on the beam loss profile of an angular scan, in the UA9 experiments. A lower diffusion speed of the beam halo or a larger miscut angle should be provided to overcome such a difficulty.

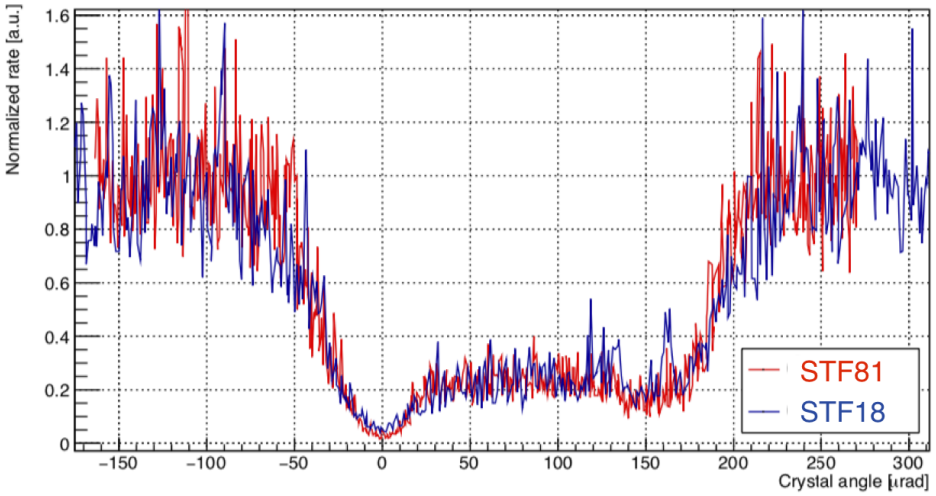

Fig. 32. Angular scan of the crystals SFT18 and STF81.

5.8. *Reducing the SPS mechanical aperture*

In crystal-assisted collimation, the multi-turn mechanism permits the capture in channeling states of halo particles not channeled in the first crystal impact. Moreover, such a mechanism plays the important role of contributing to increase collimation efficiency and to reduce background. The only condition is that there is sufficient clearance between crystal and absorber to guarantee the multi-turn dynamics of particles not captured in channeling states. On the other hand, any restriction of the mechanical aperture outside the crystal-absorber location will drastically affect the probability of the multi-turn process. This is not a hypothetical scenario. Indeed, a possible way of inserting crystals to assist collimation in a superconducting hadron collider such as the LHC operating with nominal performance consists in introducing the crystal in the shadow of the primary amorphous collimator and in exposing it gradually to the halo. Studies of such scenarios were performed in UA9, using the amorphous collimators contained in the tank TCXHW.51651, installed at the beginning of LSS5, two SPS cells upstream the crystals in the cleaning insertion. During the SPS test, the collimators were gradually inserted into the vacuum pipe, in order to artificially reduce the available mechanical aperture and to partially shadow the halo particles directed into the crystal aperture. The main goal was to observe the effect induced by the collimator superposition with the crystal on the dynamics of the deflected halo particles and on the loss recorded during angular scans.

The tests in the SPS were performed with lead ion beam made of single bunch of about 10^9 particles and 6.5×10^9 m $\cdot$ rad emittance, stored at 270 GeV per charge. The crystal, either the STF18 or the SFT81, alternately, was positioned at 6σ, while TAL1 was at 9σ from the circulating beam center. The trajectories of the

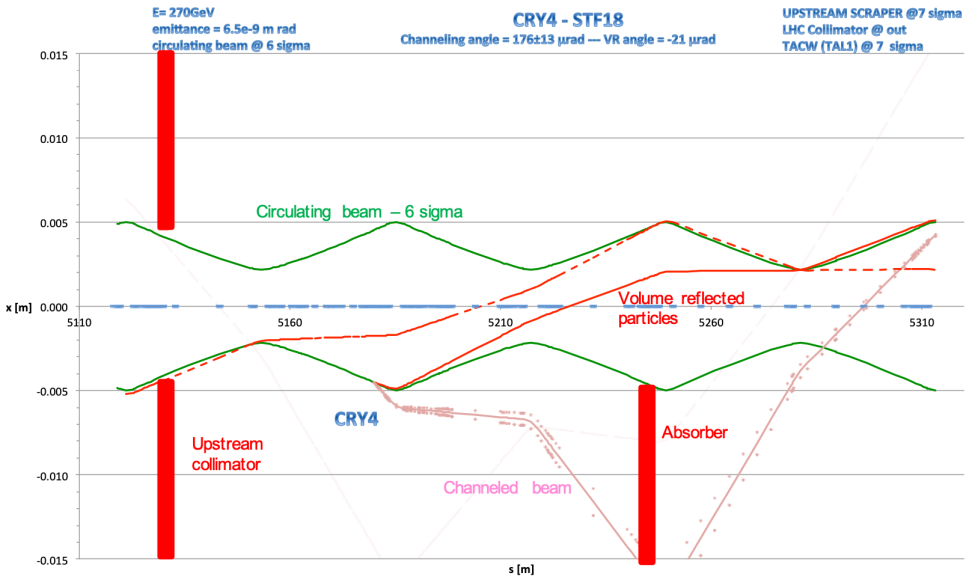

Fig. 33. (Color online) Tracking of the beam in the SPS. In green the circulating beam at 6σ with energy 270 GeV and emittance 6.5×10^{-9} m · rad. In brown the beam channeled by the crystal with 176 μrad. In red the volume-reflected beam at the first turn. In light orange the volume-reflected beam at the second turn.

halo particles that have had a coherent interaction with crystal STF18 in perfect orientation for channeling are shown in Fig. 33. The particles captured in channeling mode are deflected by an angle of 176 μrad into the TAL1 absorber downstream. Instead, the incoming particles volume reflected toward the center line, after one revolution, should hit the upstream collimator and should be absorbed there. The angular scans recorded with the upstream collimators surrounding the circulating beam at four different distances from the beam center are shown in Fig. 34. The normalized losses recorded downstream the crystal (top) and downstream of the TCXHW.51651 collimators (bottom) are plotted as a function of crystal angle. As the collimator-crystal gap varies from 3.1–0.1σ the loss reduction

Table 5. Variation of the loss reduction factor induced by the shadowing of the crystal by an amorphous collimator.

Crystal free area [$\Delta\sigma$]	R_{STF18} CH orientation	R_{coll} VR orientation	R_{STF18} CH orientation	R_{coll} VR orientation
3.1	3.8 ± 0.1	2.9 ± 0.2	1.5 ± 0.1	1.4 ± 0.2
2.1	3.3 ± 0.1	2.5 ± 0.2	1.4 ± 0.1	1.3 ± 0.2
1.1	3.2 ± 0.1	2.3 ± 0.2	1.5 ± 0.1	1.2 ± 0.2
0.1	2.8 ± 0.1	2.2 ± 0.2	1.1 ± 0.1	0.8 ± 0.2

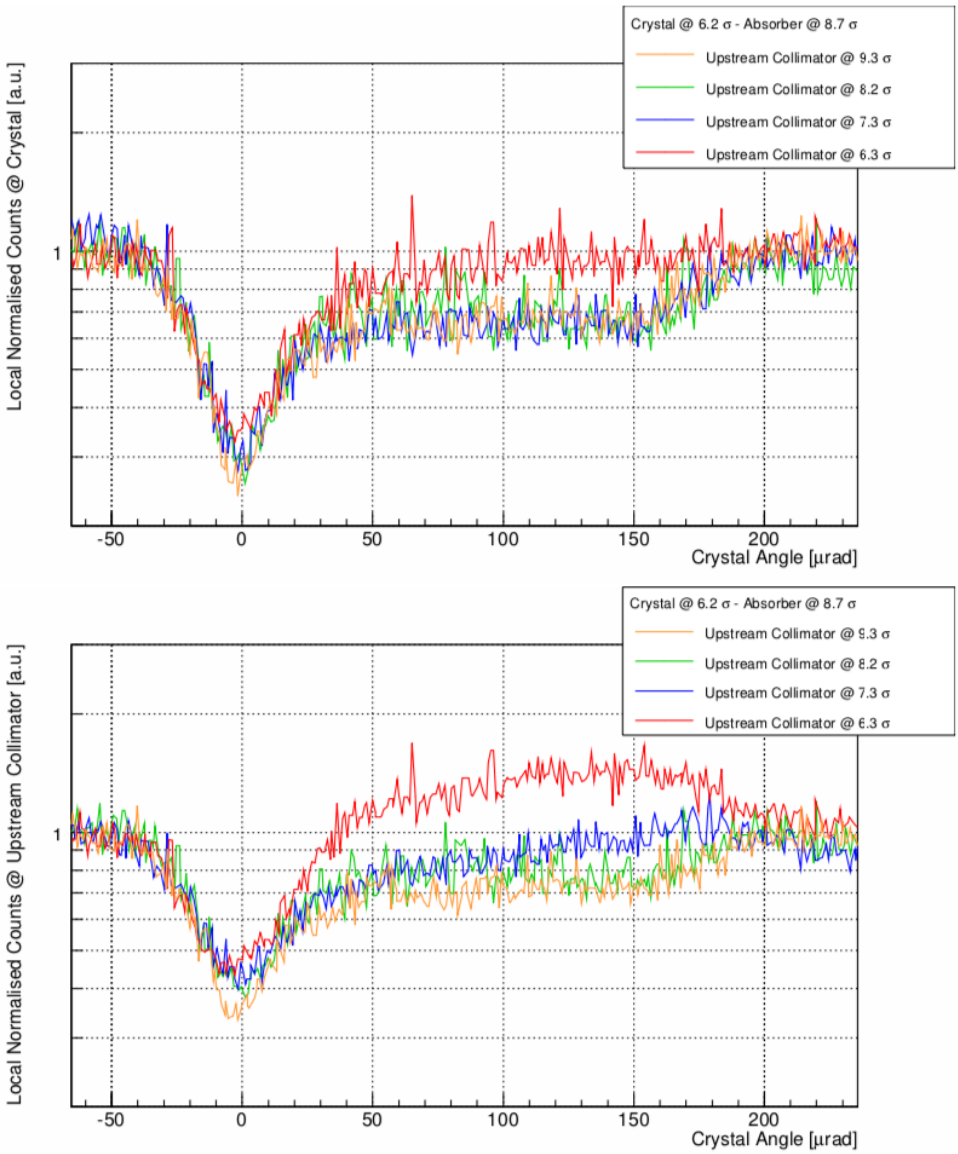

Fig. 34. (Color online) Effect of upstream collimator on crystal angular scan shape. Four different scans with lead ion beams are shown with different upstream collimator settings. Normalized losses are presented at crystal position (top) and the upstream collimator position (bottom).

ratio is monotonically reduced, while the VR particles produce increasing losses. The results of the loss reduction ratio measurements, computed from the angular scans, are presented in Table 5. Similar results were recorded using crystal STF18 with a beam of 10^{11} protons stored at 270 GeV, as shown in the angular scan plots of Fig. 35, where only the losses downstream the crystal are illustrated.

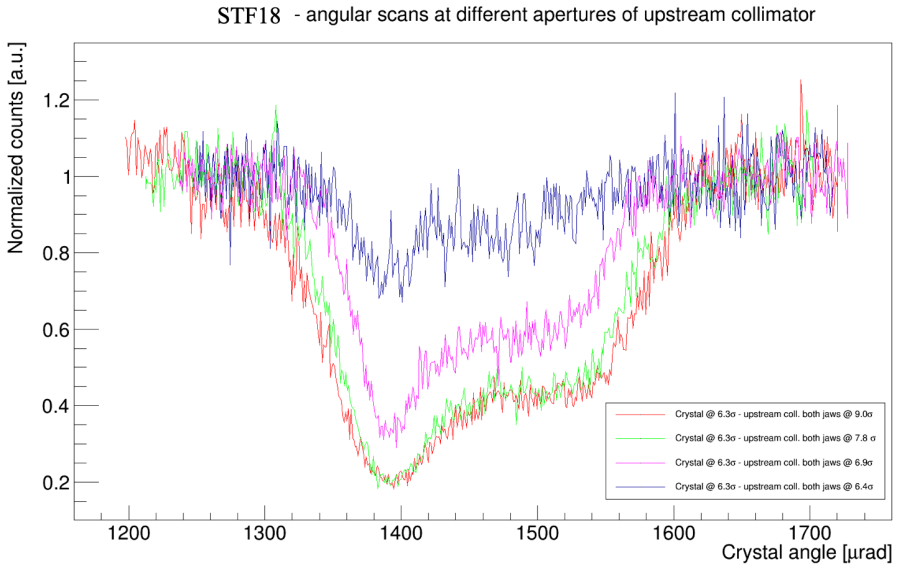

Fig. 35. Effect of upstream collimator on crystal angular scan shape. Four different scans collected with proton beams are shown with different upstream of collimator settings. Normalized losses are presented at crystal position.

5.9. *Crystal irradiation effects*

High fluxes of high-energy particles may endanger the crystal quality by producing dislocations in the crystalline lattice that could reduce the channeling performance. Previous investigations in various laboratories, recently complemented by UA9 studies, help in evaluating to which extent irradiated crystals may preserve their function of assisting beam manipulations in hadron collider.

A pioneering experiment, performed at U70 in Protvino, with 70 GeV protons, provided a deep insight in this matter.[60] A bent crystal was intercepting the 70 GeV extracted proton flux, with the aim of generating a secondary-particle beam. The particles captured in channeling states were deflected into a magnetic channel equipped with detectors. The silicon crystal was a thin plate 0.5 mm thick, with 40 mm vertical height and 30 mm length along the beam direction. The intercepted beam was extracted with a repetition period of 9 s, in bursts of 5 μs, containing on average 1.3×10^{13} protons per cycle. The RMS beam dimensions were $\sigma_x = \sigma_y = 1.4$ mm and the angular divergence in the x-plane was $\sigma_{x'} = 0.8$ mrad. In each cycle, about 1.8×10^{12} particles were thus hitting the front face of the crystal. The deposited power, estimated to be 1 W, heated the crystal up to the measured equilibrium value of 423° K. At each beam passage, the crystal was subject to thermo-mechanical stress, particularly dangerous because of the bender constraints. By bonding the crystal to the surface of a metallic cylinder, homogeneous curvature was obtained. However, the crystal was over-constrained and eventually

fractured from the effects of dynamic stresses. Pressing the crystal by sprung supports against a metal base was the reliable method finally adopted to impart the curvature. The crystal was bent along the (111) planes, over a length $L = 20$ mm (smaller than the full crystal length), by a radius $R_b = 1.5$ m and a bending angle $\theta_b = 13$ mrad. The measured deflection efficiency was 10%, a value compatible with simulations, taking into account that the angular divergence of the beam was 40 times greater than the critical angle. The intensity of the deflected beam fluctuated from one cycle to the next by 12%, while the value of the average intensity was very stable, confirming the theoretical prediction of a weak temperature dependence of the crystal deflection properties in planar channeling orientation.[61] By monitoring the centroid of the deflected beam with a remote ionization chamber, the stability of the crystal bending angle within $\Delta\theta_b/\theta_b < 10^{-2}$ was confirmed. The crystal was irradiated by the intense rapidly extracted beam during one entire accelerator run, receiving on the beam spot a total flux of $\sim 10^{19}$ protons$\cdot$cm^{-2} without mechanical deterioration or significant change of its channeling properties.

Similar investigations were performed in a series of experiments performed at FNAL with 400 GeV protons and at the AGS in the Brookhaven National Laboratory, with 28 GeV proton beams.[62] In the most recent of them, a straight silicon crystal slab 15 mm $\times$ 9 mm wide and 1 mm thick was irradiated for three month period by the 28 GeV primary proton beam directed onto the neutrino production target of the AGS. A total intensity of 2.9×10^{19} protons was sent into the crystal on a circular spot of 1.1 mm RMS radius size. Around the spot center, the peak fluence, estimated by emulsion films, was $(4.1 \pm 1.4) \times 10^{20}$ protons$\cdot$cm^{-2}. The visual effect of the crystal irradiation was a discoloration of about 3.1 mm diameter, fully compatible with the spot detected by the emulsion film. Crystal damage was examined by Rutherford Back-Scattering (RBS), using 2 MeV single ionized helium beam from SUNY-Albany Dynamitron that was fully ionized at the crystal surface impact. As for the previous experiments at FNAL and AGS, the crystal disorder was the observed indicator of radiation induced damage, quantified by the minimum yield of back-scattered alpha particles. The measured value of minimum yield was 2.3% at the non-irradiated crystal surface and 4.1% at the maximum point of damage, respectively. This study was the first to show clear evidence of radiation damage from high-energy beams affecting the crystal morphology. The radiation damage should have been lower if the beam had entered the crystal within the critical angle.[63] However, a question remained unsolved: how to characterize that damage. From the RBS, indirect information on the crystal dislocation density and its radiation-induced increase could be inferred, but it was very difficult to correlate the observed damage more directly to the reduction of channeling efficiency. Also the chemical-physics characteristics are affected by the irradiation.

A bent crystal, submitted to intense irradiation of 450 GeV proton beam extracted from the SPS, provided direct comparison, under controlled conditions, of deflection efficiency in highly-irradiated and non-irradiated areas of the same silicon slab. The slab, 50 mm long in the beam direction, 10 mm wide and 0.9 mm

thick, cut parallel to (111) planes, was mounted in a three-point bender, encircling 30 mm of its length, easily adjustable to impart variable horizontal deflection in the range from 1 to 11 mrad. In a first experiment, the crystal was widely tested to investigate channeling properties as a function of bending angle and to compare them to theoretical expectations.[64] The horizontal divergence of the 450 GeV proton test beam was 3 μrad, thus smaller than the critical angles that, for the larger and thinner (111) channels, were 9 and 3.6 μrad, respectively. For $\theta_b = 2.4$ mrad and $R_b = 12.5$ m, a reference curvature for other applications, the fraction of deflected beam was almost 50% of the total beam hitting the crystal, while about 35% of protons were not deflected and 15% were lost due to dechanneling. In a second experiment, the same crystal was used to investigate radiation damage. Dismounted from the bender, it was irradiated for 1 year in the North Area of the SPS, in nonaligned orientation, receiving a total intensity of 2.4×10^{20} protons$\cdot$cm^{-2} over an area of 0.8 mm $\cdot$ 0.3 mm at FWHM.[65] The irradiated area was evaluated by contact radiography. However, during such an operation the crystal was broken in two pieces. One of them could be inserted in the three-point bender, slightly adjusted to encircle 25 mm crystal length instead of 30 mm encircled length of the unbroken crystal. Because of this, for a given bending angle, the radius of curvature was smaller than in the unbroken crystal, in particular, for $\theta_b = 2.4$ mrad, the radius of curvature was $R_b = 10.4$ m and the deflection efficiency was systematically reduced. Moreover, a large anticlastic reaction was observed that changed the crystal shape as a function of the vertical coordinate. This introduced serious complications in determining the influence of the radiation damage, solved by applying more sophisticated procedures in the data collection and analysis. The channeling efficiency was recorded by displacing the beam vertically. At each beam position, the crystal orientation was adjusted to compensate for the anticlastic bending. Focusing and parallel vertical beam optics were used to guarantee the optimal crystal orientation, both for small size or small divergence beam spots. The measured peak channeling efficiency was 23% in the non-irradiated area and 16% in the center of the irradiated area. The efficiency reduction shape was easily fitted to a Gaussian shape expected for the irradiated spot. The relative peak reduction of the channeling efficiency was $31 \pm 4\%$ for peak fluence at the spot center of 5.0×10^{20} protons $\cdot$ cm^{-2}. Finally, by assuming a linear dependence of the radiation damage with the radiation fluence, the calculated slope coefficient of the relative deterioration was $(6 \pm 2)\%/10^{20}$ protons $\cdot$ cm^{-2}.

In hadron colliders, the asynchronous firing of fast magnets during injection or dump process is a rare faulty situation that eventually produces large orbit oscillations of part of the beam. The oscillating particles may hit the crystal, depositing thermal energy and inducing thermo-mechanical stress. Thermal damage occurs in the necking region, for brittle-to-ductile transition at 850 K and for the solid-to-liquid transition at 1710 K. Local damage of the crystal surface may appear at even lower temperature. Controlled tests were carried out at the CERN HiRadMat facility[66] to investigate crystal damage eventually due to accidental beam loss.

Pulses of 7.2 μs duration, made of up to 288 bunches of 10^{11} protons each, with the RMS beam size of 0.3–0.5 mm in each plane, were extracted from the SPS at 440 GeV/c for a maximum pulse energy of 3.4 MJ. Such a beam, identical to the proton batches used to fill the LHC, was used to irradiate bent crystals, in a configuration reproducing that of accidental crystal irradiation. Such tests were significant also at top energy, since in silicon crystals a few mm thick the energy deposition of 440 GeV/c protons is only 10% less than at 7 TeV. In the first test,[67] the selected crystal, similar to the LHC crystals described in Table A.2, was a silicon strip with a 3 mm $\times$ 55 mm face, 1 mm thick, produced at INFN-Ferrara, bent along the (110) planes, by an angle $\theta_b = 50$ μrad. The experimental setup was accommodated in an aluminum tank, to prevent accidental contamination, equipped with glass windows to permit interior inspection. The crystal, mounted on its vertical aluminum holder, was deliberately rotated by 1° to be in amorphous orientation and was fixed on a sliding support to optimize its horizontal position, as the width of the crystal was smaller than the beam FWHM. A stainless steel strip 1 mm thick, 11 mm long, was installed beside the crystal for more accurate beam-based alignment with low-intensity pulses, during which two diamond detectors were serving as beam loss monitors. For visual verification of the alignment, a screen with self-developing film (GAFCHROMIC© XR-SP2) and a ruler were installed upstream the crystal, monitored online with off-the-shelf webcam. Once the crystal was aligned, high-intensity pulses were extracted from the SPS. The normalized transverse emittance was approximately $\epsilon_x = \epsilon_y = 3.5 \times 10^{-6}$ mrad, confirming the desired RMS beam size of 0.5 mm in both planes. Starting initially with a single bunch of 1.1×10^{11} protons, the number of bunches per pulse was gradually increased to 72, 144 and 288. The integrated number of protons extracted during all high-intensity shots was approximately 2×10^{14}, those hitting the crystal were about 1–1.3 $\times$ 10^{14}, taking into account an alignment accuracy of the order of 0.5 mm. Although the full beam struck the same crystal point with an accuracy of the order of 100 μm, no mechanical damage could be observed after irradiation. In the second test,[68] the two crystals, listed in Table 6, were irradiated at the same time. QMP33 was a quasi-mosaic silicon crystal of the same kind as those already installed and tested in the LHC for collimation purposes (see the three QMP crystals in Table 1). The STF103 was a strip silicon crystal slightly different from the SFT75 (see Table 1) already tested in the LHC collimation. The bending angle was the same, but with half the thickness along the beam direction and quadruple in the transverse direction. The larger transverse size was chosen to simplify the alignment procedure in HiRadMat. The thickness was reduced to test a crystal with higher mechanical stresses induced by the bending holder with respect to a standard LHC strip crystal. This test was important also for other applications, such as crystal-assisted beam extraction in the SPS,[69] where crystals with greater curvature could be used.

The same tank of the first experiment, with an improved alignment system, was used. The two crystals with their respective holders were mounted a single

Table 6. Crystals used in the second HiRadMat test.

HiRadMat crystals	Origin	$L \times W \times H$ [mm^3]	θ_b [μrad]	R_b [m]
QMP33	PNPI	$4.0 \times 30.0 \times 27.0$	40	100
STF103	INFN	$1.97 \times 1.88 \times 55.0$	55	36

mechanical support that could be moved horizontally and vertically with respect to the beam axis. A copper mask, instead of the stainless steel strip, was added for beam-based alignment at low intensity. The alignment procedure consisted of performing vertical and horizontal scans around the beam position with the copper mask, precisely aligned with the crystals, and measuring losses by BLMs downstream. The minimum loss rate indicated the best mask and crystal positions. The optimal alignment position was cross-checked using three GAFCHROMIC© foils, one upstream, one just before and one downstream of the crystals. The irradiation was repeated four times: three times with a batch of 216 bunches and one with a batch of 288 bunches. During each irradiation the vertical position of the beam spot onto the crystal faces was deliberately modified and accurately identified. After the HiRadMat test, the two crystal faces were not affected by any macroscopic damage such as cracks, deformations or surface vitrification. The absence of structural damage was further investigated by measuring the bending angle and channeling efficiency of both crystals with the UA9 silicon microstrip-based telescope in the H8 line of SPS North Area,[70] and by comparing the results to those recorded before the irradiation test. The H8 data were recorded with two different beams: a 400 GeV proton beam, with an horizontal divergence of 10 μrad (the same value of θ_c), and a 180 GeV pion beam, with a divergence of 30 μrad (two times larger than θ_c). The crystal parameters were the same within experimental errors before and after irradiation. In more detail, in QMP33, the values of the deflection angle and of the channeling efficiency, θ_b and $\eta_{\rm ch}$, stayed unchanged at 40 ± 1 μrad and at $63 \pm 2\%$, respectively, while for STF103 θ_b varied from 55 ± 1 μrad to 53 ± 1 μrad and $\eta_{\rm ch}$ from $75 \pm 2\%$ to $70 \pm 2\%$, respectively. In conclusion, silicon crystals demonstrated no macroscopic damage and preserved their beam steering performance, showing a large resilience in case of accidental beam impact at injection or during a dump. Moreover, the HiRadMat tests indirectly confirmed that the number of dislocations produced by 10^{14} particles/cm^2 fluence, 400 GeV energy proton beams does not endanger the channeling performance.

A set of nine crystals similar to STF103, built at PNPI, irradiated with a flux of $2.5{\times}10^{21}$ thermal neutrons/cm^2 at the SCK-CEN BR2 reactor in Belgium, lost on average 8% of their channeling efficiency.[71] Another set of nine crystals have been irradiated with a high flux of protons at the Brookhaven Linac Isotope Production (BLIP facility). The data analysis is still in progress. It should soon provide additional information on the issue of crystal radiation damage.

5.10. *Final considerations on the SPS experiments*

In high-energy, high-intensity, high-luminosity hadron collider, such as the LHC, the accelerator performance depends on the efficient confinement of the diffusive halo into the collimation system.[72] In a standard collimation system, based only on massive components, halo particles having lost longitudinal momentum in diffractive or inelastic scattering interactions with intercepting obstacles and having had negligible change of their trajectories may escape from the collimation area and can be lost in sensitive areas along the ring. Improvement of collider performance requires reducing production and leakage of such particles.

Crystal-assisted collimation is an innovative method to more efficiently confine the losses to a safe area of the ring, thereby guaranteeing ultrahigh luminosity runs and the highest possible physics reach. High-energy particles entering bent crystals are not only deflected in a coherent manner, they also follow paths along which the atomic density is small (inter-planar channels) with strongly reduced probability of creating showers. The UA9 results demonstrate that crystal collimation can be routinely achieved for proton and Pb-ion beams with robust and well-reproducible procedure. Its performance is superior to that of a standard collimation setup with amorphous primary target. Moreover, the crystal-collimation scheme would allow to reduce the number of collimators and absorbers needed to safely dispose of the beam halo and to place them at a larger aperture, thus reducing the machine impedance.

The UA9 components on which the successful scenario of crystal collimation is based have been carefully optimized for more than a decade. Strips or plates of high quality silicon crystals, with low dislocation and impurity density and large mosaicity, were chosen. They were bent by simple flexural stress, imparting the required curvature of the (110) or (111) crystalline planes through inter-molecular forces. The crystal length along the beam direction was short enough to minimize dechanneling effect and long enough to permit bending angles of the order of a 100 μrad, with bending radius about an order of magnitude larger than the critical radius. The angular actuator, vacuum and radiation compliant, was conceived to provide an angular orientation accuracy of the crystal better than one-half the critical angle. Dedicated detectors, such as high sensitivity BLM, scintillation sensors, Roman-pot inserting Medipix sensors inside the vacuum pipe, in-vacuum Cherenkov detector developed *ad hoc*, provided the necessary information to optimize the crystal-collimation configuration and maximize the halo particle confinement into the massive absorber. By such devices the losses downstream of the crystal and outside the collimation area were reduced by more than an order of magnitude for proton beams of 270 GeV and by a bit less than an order of magnitude for heavy ion beams of 270 GeV per charge.

The successful set of results provided by UA9 suggested to install crystals in LHC in a layout configuration a la UA9 reusing as much as possible the specific components of the existing collimation system. Extensive tests at reduced beam intensity have been performed and will be discussed in the following section.

6. Crystal-Collimation Tests in LHC

The feasibility of crystal collimation in the LHC and the experimental validation of its capability to improve the present collimation, are deemed necessary before relying on this concept in future.

A setup for testing the crystal-collimation concept in the LHC has been conceived and integrated into the betatron cleaning insertion. Different challenges have to be addressed in order to demonstrate crystal channeling for LHC. The demonstration of channeling at unprecedented hadron beam energies was the first important open point before this work. The 6.5 TeV design energy of the LHC is seven times higher than the highest energy at which channeling was observed. The critical angle at this energy is reduced on the order of the μrad. Very tight angular requirements with small acceptance demand a goniometer with very high accuracy and stability. The crystal-collimation cleaning efficiency is to be compared to the present system in order to understand if an improvement, which could justify the installation of this new collimation scheme, is indeed possible.

6.1. *Experimental layout*

A layout for crystal-collimation studies has been conceived and optimized within the present LHC collimation system.[73] Crystal assemblies, consisting in a silicon crystal mounted on a high-precision goniometer for angular adjustment,[74] have been installed in the betatron collimation insertion of LHC.[75] The crystal bending angles and lengths were optimized through semi-analytical and tracking studies to intercept the channeled halo with enough clearance with downstream secondary collimators, respect aperture constraints given by the beam pipe and the physical aperture of the elements downstream the crystals and maximize collimation cleaning performance. The required specifications for crystal manufacturers were a bending angle of 50 μrad and a length of 4 mm.

In this scheme, the crystal plays the role of primary collimator. Only selected secondary collimators are used to intercept the halo deflected by the crystal, and the shower absorbers are used at nominal machine aperture during the measurements. The secondary collimators used are the ones in the same transverse direction of the crystal. In addition, the secondary collimators mounted in a skew plane, between the horizontal and vertical direction, can be used to increase the absorption of halo particles. An example is shown in Fig. 36, where the deflected halo trajectory is determined using the LHC optic functions and the transport matrix formalism. There are also reported the position of the collimators present in the region near the crystal. The primary collimators [Target Collimator Primary (TCP)] are not used during the crystal measurement. A detailed layout on the whole machine configuration during the tests is presented in Ref. 76.

The present LHC crystal-collimation experimental setup[73,77] is composed of four crystals: one for each plane and beam. In this experimental layout, it was possible to observe channeling in several LHC configurations, and also to characterize the

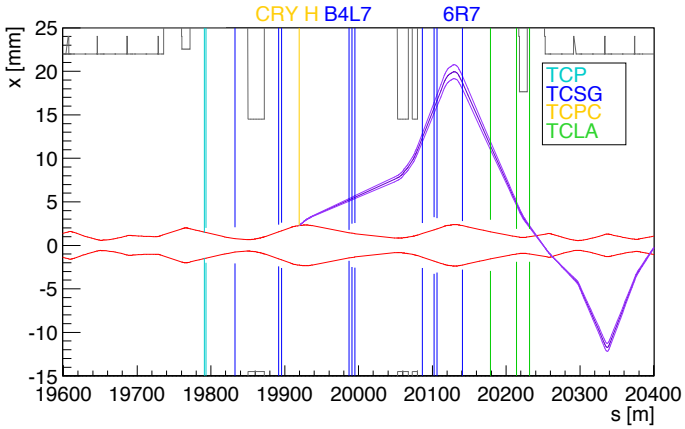

Fig. 36. (Color online) Trajectory of channeled halo particles (purple lines) at 6.5 TeV for the horizontal crystal. The envelope of the circulating beam at amplitudes defined by the crystal settings is also given (red lines). Vertical lines indicate the aperture of the IR7 collimators in the plane of interest.

crystal properties. Local losses at crystal and other positions are used to measure crystal characteristics in a circular accelerator.

6.2. *Design of LHC goniometers assembly*

The crystals are housed in special assemblies, referred to as goniometers.[74] The goniometers are used to adjust both the crystals transverse position (*linear stage*) and orientation (*rotational stage*) with respect to the circulating beams. The main technical requirements to be addressed to guarantee both the crystal collimation functionality and the safe operation in the LHC environment can be summarized as: a rotational stage with an angular range of ± 10 mrad, an angular resolution of 0.1 μrad and an accuracy of ± 1 μrad within 10 mm on the linear stage, from the beam axis; transparency to LHC operation.

To address the requirement for precision and accuracy a piezoelectric actuator was used for the rotational stage, coupled with a high-precision linear axis. During standard LHC operation, the crystals and the full goniometer assembly are not visible to the beam. The crystals are retracted (with a dedicated linear stage) and replaced by a special round vacuum chamber that is inserted to offers to the beam a smooth and continuous pipe aperture.

The crystal/goniometer assembly is called Target Collimator Primary Crystal (TCPC). A schematic drawing is shown in Fig. 37.

6.3. *Channeling observation at multi-TeV energies*

Angular and linear scans are applied to evaluate the channeling performance (see also Subsecs. 4.2 and 4.3). In Fig. 38, a schematic view illustrates how these measurements are performed.

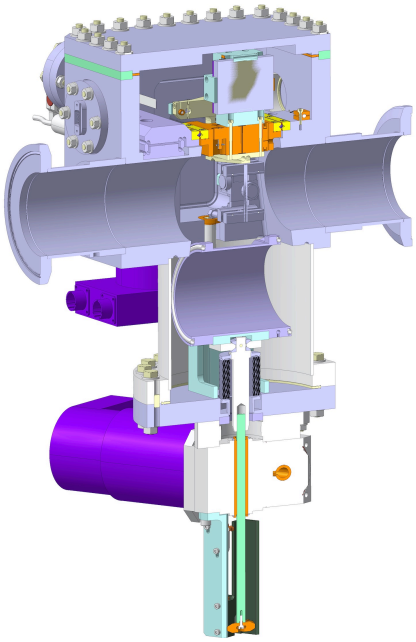

Fig. 37. Schematic drawing of the main part of the vertical goniometer: the crystal is installed in the chamber above the pipe. It is visible also the pipe section, in this case, retracted, to allow the crystal in the beam line.

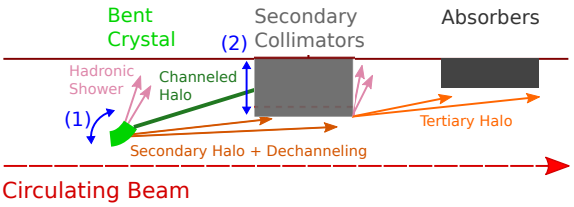

Fig. 38. Illustrative view of the crystal angular scan (1) and of the collimator linear scan (2) that are used to demonstrate experimentally the onset of channeling. Angular scans are used to find the optimum channeling orientation when nuclear losses are minimized. Collimator scans probe the distribution of the channeled halo and the dechanneling region.

The first goal of the tests in LHC was to demonstrate that the channeling phenomenon is observable with LHC beams.

Channeling was then achieved at 6.5 TeV[78] with an angular scan (see Fig. 39). Observation of channeling with protons of such energy was obtained for the first time ever in 2015, with the B1 horizontal crystal.

The edges of the beam losses are sharper with respect to the ones observed in SPS angular scans because the beam emittance is lower at this energy. A second local minimum is observed at the end of the volume reflection at about 65 μrad from the channeling minimum. This is the bending angle of the crystal (note the

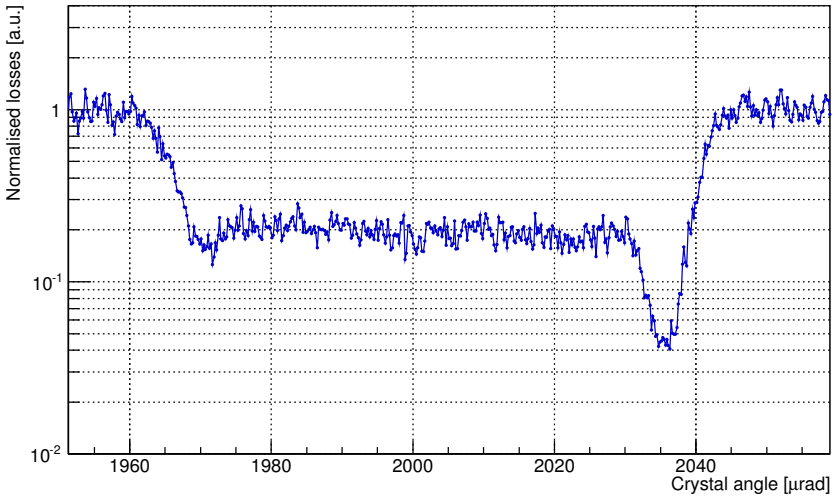

Fig. 39. Flat top angular scans for B1 horizontal crystals. Losses are normalized to the beam flux and to the loss level in amorphous orientation, and shown as a function of the rotational stage orientation angle.

similarity with the SPS data reported in Fig. 20). At this orientation the volume of the crystal that interacts with the beam halo is so small that the volume reflection kicks always increase the oscillation amplitude in the phase space.[78] For this reason particles get a sufficient kick to be absorbed by secondary collimators more quickly.

These measurements demonstrated that the channeling (and other coherent effects) scales to higher energy as expected. The same observations were performed with heavy ion beams such as lead[79] (see Fig. 40) and xenon.[76]

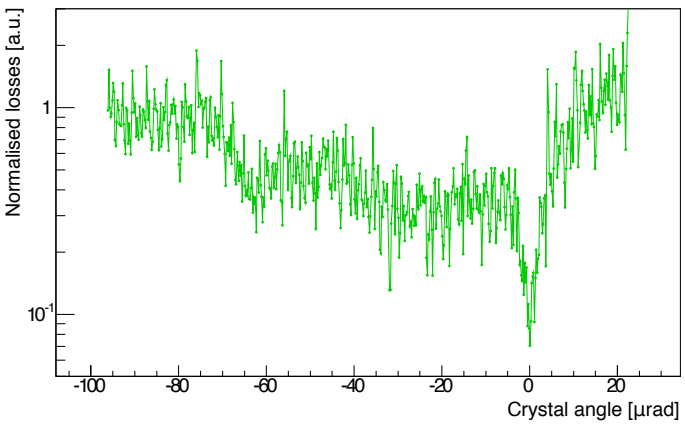

Fig. 40. Local beam losses normalized to the beam flux, and to the BLM signal in amorphous orientations, as a function of the crystal angle for the horizontal crystal. The scan was performed at 6.5 Z TeV with the horizontal crystal on beam 1.

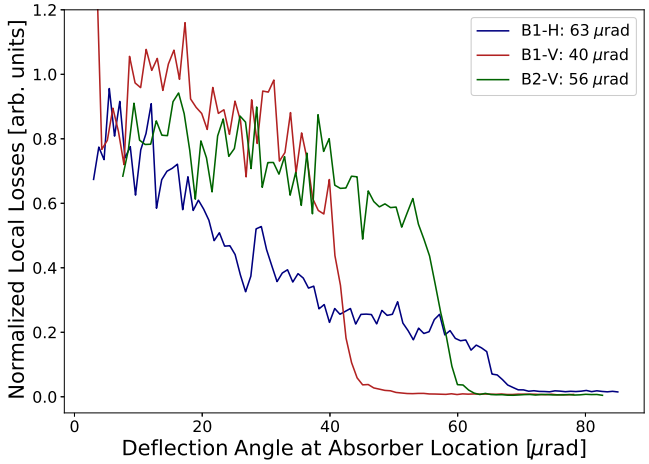

Fig. 41. Beam losses during collimator scan of the channeled beam. The BLM signal is normalized to beam flux and to the loss level at interception of the circulating beam. Data are plotted as a function of the equivalent deflection at collimator position, recorded at TCSGs during linear scans with the crystals in channeling orientation.

By measuring crystals of different bending angles, the dechanneling population was found to be enhanced when the bending radius is close to the critical radius at the LHC energy of 6.5 TeV.[80] This is measured using a collimator scan: the crystal is set in channeling orientation and a downstream collimator is inserted toward the beam pipe center to probe the channeled beamlet. Local losses at the collimator show the presence of channeling and allow to measure its properties as a function of the collimator jaw position (Fig. 38). In Fig. 41, some examples of the measurements on three different crystals during a test with LHC 6.5 TeV proton beam are illustrated.

As reported in Table 7, one of the crystals, the B1 horizontal crystal, is significantly more bent than the others, with a bending radius $\sim 5\ R_c$ at top energy. In Fig. 41, it can be observed that the loss rise between the channeling and the beam core has a higher slope with respect to the other two crystals. This is considered

Table 7. Crystal bending angles and multi-turn channeling efficiency computed from different data sets. Bending angles are computed as averages of measurements at both injection and top energy. Multi-turn channeling efficiency averages are reported per beam energy.

		Multi-turn channeling efficiency [%]	
Crystal	Bending angle [μrad]	Injection	Flat top
B1-H	63.2 ± 1.7	71 ± 5	27 ± 5
B1-V	39.8 ± 2.3	87 ± 5	84 ± 5
B2-V	56.5 ± 1.8	83 ± 5	72 ± 5

an indication for a particularly enhanced dechanneling population at low deflection angle. From this measurement is possible to evaluate the crystal channeling efficiency, as described in Subsec. 4.3. A comparison of the efficiency evaluated at injection (450 GeV) and top (6.5 TeV) highlights the drop in performance of the B1 horizontal crystal. The extreme bending, at such energy, causes a distortion too strong in the bent potential well, that reduces the efficiency of channeling and enhances a quick nuclear dechanneling of the initially trapped particles. Further details are presented in Ref. 80.

Observation of skew planes

Two crystals, installed in a second moment in 2017, were found to be close to the crystal axis ($\langle 211 \rangle$).

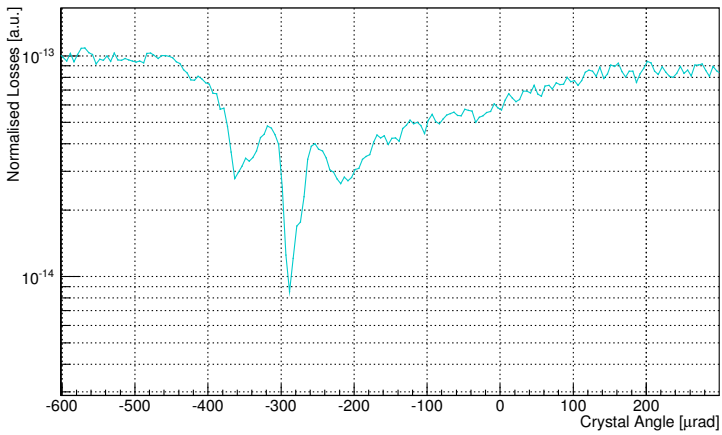

(a) Wide angular scan with B2H crystal.

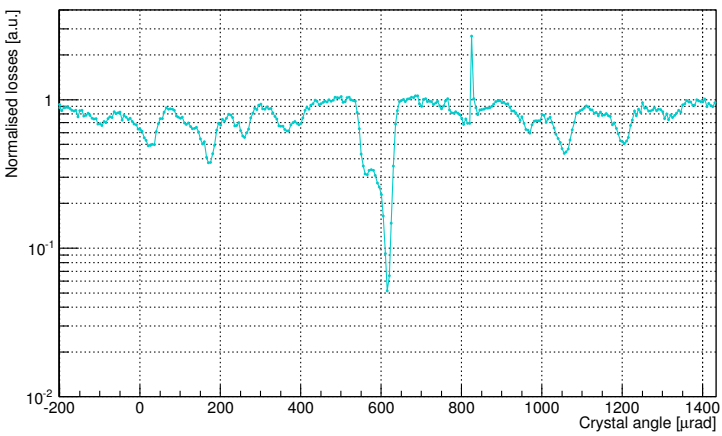

(b) Wide angular scan with B2V crystal.

Fig. 42. Horizontal and vertical B2 crystal angular scans, at injection energy. Losses are normalized to the beam flux and shown as a function of the rotational stage orientation angle.

This has been observed with a wider angular scans (Fig. 42), similar to the observations made in SPS and described in Subsec. 5.2. In the horizontal case, the crystal is oriented too close to the axis, as shown in Fig. 42(a), so that achieving the best channeling orientation is virtually impossible. The vertical crystal is, however, sufficiently far from the axis so that the skew planes are spread out enough to make possible the channeling observation at both injection and top energy.

The presence of skew planes was confirmed by linear scan measurements,[76] that allowed a detailed investigation of the deflection given by the skew planes channeling.

6.4. *Crystal-collimation performance in the LHC*

The cleaning inefficiency of the standard collimation system is measured by Loss Map (LM): a synchronized measure of losses at all the about 4000 beam loss monitors (BLM),[81] ionization chamber detector, spread out along the 27 km ring. To generate a clear signal in the BLMs, a white noise excitation is used to induce controlled high beam loss,[82] allowing a detailed reconstruction of the loss pattern used to validate system performance.

With the standard collimation system, the highest losses are observed at the primary collimator locations; this signal is proportional to the number of halo particles intercepted by the collimation system. Hence, by normalizing all the loss signals to that value, it is possible to retrieve a direct measurement of collimation inefficiency at every machine location. The Dispersion Suppressor of IR7 (IR7–DS) is the point where the highest losses on cold magnets are observed; therefore, the collimation inefficiency is measured in that specific region. An example is given in Figs. 43(a) and 43(b).

With crystal collimation the highest losses are observed at the location of the first collimator used to intercept the channeled halo. This loss signal is not proportional to the number of particles intercepted by the collimation system (i.e. the particles intercepted by the crystals). A qualitative comparison between standard and crystal-collimation LMs is shown in Fig. 43. As shown in Fig. 39, the losses in channeling are reduced with respect to an amorphous material; thus, the collimation loss pattern is different between crystal and standard system. A different normalization has been proposed to compare the two systems, which is uncorrelated to the beam losses at the collimation primary stage. It is chosen to normalize each BLM signal to the flux of particles that are lost from the machine, evaluated from the bunch-by-bunch beam current measurements. This value is considered to be the best estimation possible of the total number of particles that are lost from the machine because of the interaction with the collimation system.

To measure and compare the performance the *leakage factor* is defined; this represents the highest normalized loss value observed in a given machine longitudinal position. In particular, for betatron cleaning the IR7–DS is the region where highest leakages are observed, as already introduced. Several mechanisms are responsible

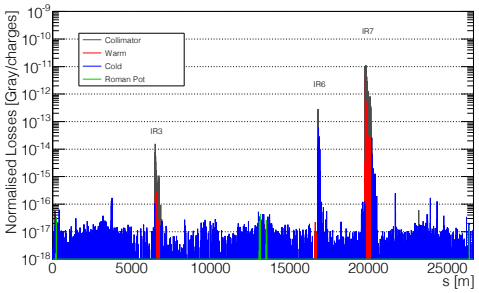

(a) Experimental standard system, full ring.

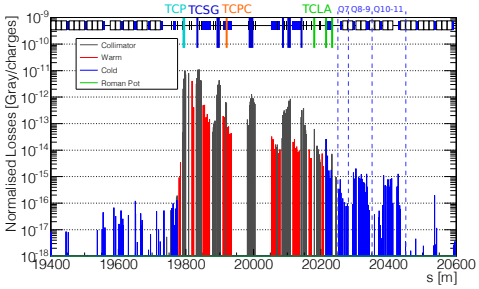

(b) Experimental standard system, IR7 zoom.

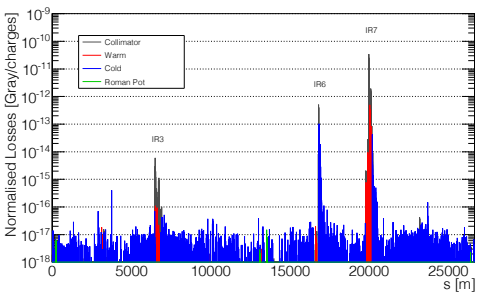

(c) Experimental crystal collimation, full ring.

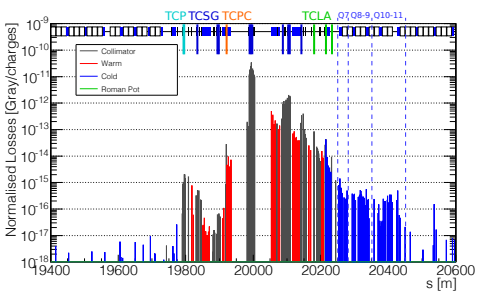

(d) Experimental crystal collimation, IR7 zoom.

Fig. 43. Horizontal experimental loss maps in the full LHC ring (a) and (c), and in IR7 (b) and (d), with proton beam at top energy. Crystal collimation is used with Cfg#1 from Table 8. BLM signals are normalized to the instantaneous beam flux.

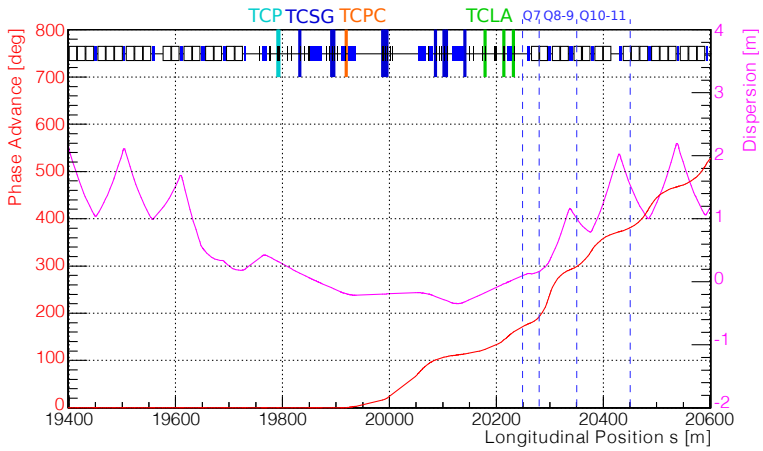

Fig. 44. (Color online) Dispersion function (solid magenta line) and phase advance (solid red line) with respect to the horizontal B1 crystal around IR7 in LHC. The longitudinal location of standard collimators, the crystals and the regions where the performance are compared are highlighted on top of the plot.

for different limiting locations in the DS; hence, different longitudinal regions close to the IR7–DS are highlighted to evaluate the possible cause of the system limitations. In particular, three regions in the matching section and in the dispersion suppressor of IR7, are selected. The different regions are named after the enclosed cold quadrupole (Q). The first one, at the end of the matching section, is where the quadrupole magnet Q7 is located. The Q7 region is considered because the close TCLAs collimators (tungsten absorber) may cause hadron showers in this region if the load of particles impinging on them is very high. The other two regions are located where the first two dispersive peaks of IR7–DS appear. One is identified by the magnets Q8 and Q9, and the other by the magnets Q10 and Q11. The dispersion function and the phase advance with respect to the crystal location, are shown in Fig. 44 for the horizontal case. Further details are presented in Ref. 76.

6.4.1. *Experimental procedures*

The crystal-collimation LM were measured aligning the crystals as primary obstacles and orienting it in channeling. As introduced, a set of the collimators available in the betatron collimation insertion of the LHC were used during the crystal-collimation cleaning measurements. The settings used are reported in Table 8. While the crystal collimation was in place, the collimators were set to the same apertures of the nominal collimation system; a complete description of the procedure is reported in Ref. 76. Different sets of collimators and settings were used to compare the effects on the crystal system, and obtain important insight. As an example, comparison between configuration #1 (Cfg#1) and #2 in the horizontal plane, highlights the effect of the insertion of collimators upstream the crystal. Instead,

Table 8. IR7 collimators positions (in σ units) during flat top loss maps measurements with proton beams. Collimators are listed by descending order in longitudinal position.

Collimator		Standard collimation [σ]	Crystal collimation					
			B1 horizontal [σ]			B1 vertical [σ]		
Configuration (Cfg)	Type (material)	Nominal	#1	#2	#4	#1	#2	#3*
TCPs	primary (C)	5.5	7.5	Out	7.5	Out	Out	Out
TCSG upstream	secondary (C)	7.5	7.5	Out	7.5	Out	Out	Out
TCPCV.A6L7	vertical crystal (Si)	Out	Out	Out	Out	5.5	5.5	5.5
TCPCH.A4L7	horizontal crystal (Si)	Out	5.5	5.5	5.5	Out	Out	Out
TCSG downstream	horizontal secondary (C)	7.5	7.5	7.5	7.5	Out	Out	Out
TCSG downstream	vertical secondary (C)	7.5	Out	Out	Out	7.5	7.5	7.5
TCSG downstream	skew secondary (C)	7.5	7.5	7.5	Out	7.5	Out	7.5
TCLAs	shower absorber (W)	11.0	11.0	11.0	11.0	11.0	11.0	11.0

*Crystal oriented in amorphous.

Cfg#4 shows how removing secondary collimators to absorb the residual deflected halo affects the system performance. In the vertical plane, Cfg#1 and #2 differs for using the full set of secondary collimators downstream the first absorber. Finally, the vertical Cfg#3 is used to study the effect of a crystal oriented in amorphous on the crystal-collimation system.

6.4.2. *Simulations tools*

The `SixTrack` code[83] is used to provide a symplectic, fully chromatic and 6D tracking along the magnetic lattice of circular accelerators, taking into account interaction with obstacles (as collimators) and the machine aperture model. The machine optic and aperture is produced with the `MAD-X` code.[84] In `SixTrack`, a crystal routine has been developed[77] and will be described in Subsec. 7.1.

It has to be pointed out that BLM signals are produced by hadronic showers coming from lost particles interacting with the beam pipe, and all the other materials between the point where the proton is lost and the BLM position. In `SixTrack` it is possible to simulate the beam loss pattern, i.e. the expected number of protons lost per meter on the machine aperture. This means that the loss pattern and the BLM signals can be considered comparable to a first approximation, if one considers the loss distribution to be equal in both measurements and simulations. Thus, under this hypothesis, it is possible to perform relative studies between the simulations and the loss maps measurements.

6.5. *Cleaning measurements with proton beams*

To compare the crystal-collimation system to the standard one, the ratio of the leakage factors, measured with the standard collimation to the one measured with the crystal system, is used: a ratio larger than 1 indicates an improved cleaning performance of the crystal-collimation system with respect to the standard one. Moreover, it highlights how many times the crystal collimation is improving the machine cleaning. Conversely, a ratio smaller than 1 indicates a worse performance of crystal collimation, i.e. a ratio of 0.5 indicates that the crystal collimation is performing at 50% of the standard system capacity (or that it is two times worse). These *leakage ratios*, measured in IR7–DS, on three different regions defined in Subsec. 6.4.1, are presented in detail in Table 9.

In simulations, the cleaning efficiency is evaluated averaging the cold losses in the same regions of interest defined in measurements in IR7. The simulated cleaning ratios, between standard and crystal collimation, are reported in Table 9. A more detailed and extensive analysis is presented in Refs. 76 and 85.

Vertical plane

For the vertical crystal Cfg#1 an improvement by at least a factor of 3 is observed in the dispersion suppressor region, and an improvement of losses of a factor higher

Table 9. Collimation leakage ratio (standard versus crystal) for proton beams. Measurements and simulations leakages are reported for each layout listed in Table 8.

	Leakage ratio IR7–DS					
	Q7		Q8–9		Q10–11	
Configuration	Meas.	Sim.	Meas.	Sim.	Meas.	Sim.
H–1	0.34 ± 0.06	—	2.34 ± 0.53	9.99	1.54 ± 0.40	7.74
H–2	0.56 ± 0.08	—	3.67 ± 0.59	11.46	2.60 ± 0.44	9.15
H–4	0.27 ± 0.06	—	2.99 ± 0.53	12.87	2.03 ± 1.09	11.04
V–1	3.49 ± 1.54	—	16.43 ± 9.60	20.00	11.25 ± 2.99	22.45
V–2	0.17 ± 0.01	—	3.34 ± 0.27	12.33	3.17 ± 0.12	14.47
V–3*	0.42 ± 0.06	—	0.68 ± 0.10	0.40	0.73 ± 0.07	0.51

*Crystal oriented in amorphous.

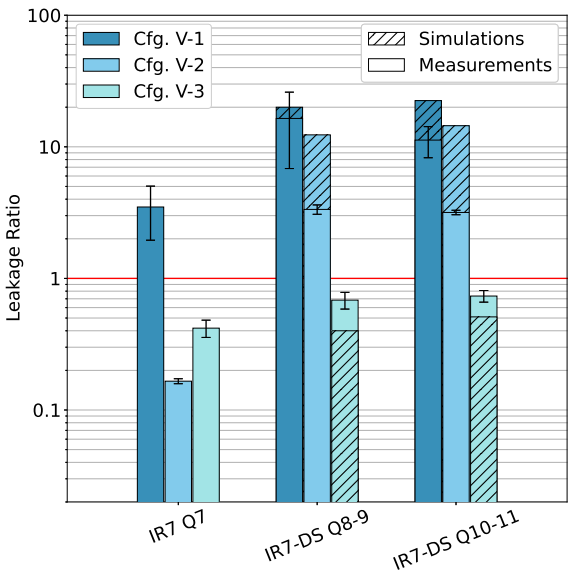

Fig. 45. (Color online) Leakage ratio with respect to standard collimation in several LHC locations, for proton beams at top energy. Measurements and simulations are shown by solid and dashed bars, respectively, for the vertical configurations in Table 8. The red line shows the standard collimation reference: above the line the crystal collimation is improving the cleaning performance of the present system.

than 10 is observed in both Q8–9 and Q10–11 regions (where the dispersive peaks are located). When a reduced set of TCSGs is used in Cfg#2, the system shows a reduced performance, see Fig. 45. Finally, orienting the crystal as an amorphous material shows a general worsening in the collimation performance, between 30–50% less than standard collimation in every region under study.

In simulations, the relative performance with respect to standard collimation is reasonably well reproduced, as shown in Fig. 45, apart from the observation of losses in the Q7 region. In Cfg#2 where only TCLAs (at 11σ) are used to absorb the channeled halo, crystal-collimation performance is two times more efficient in simulation than in measurements in the IR7–DS. The amorphous orientation Cfg#3 presents leakage ratios in agreement between simulation and measurements.

Horizontal plane

In the horizontal plane, a worsening of cleaning performance is observed with any configuration of crystal-collimation setup. In particular, what appears to consistently limit the performance is the leakage in Q7 (see Fig. 46). Comparing #1 (Cfg#1) and #2 in the horizontal plane, demonstrate that the presence of upstream collimators reduces the performance of the crystal system by about $\sim 40\%$ in any region in consideration. This effect was studied in the SPS, as presented in Subsec. 5.8.

The leakage ratios measured in Cfg#4 clarify that removing secondary downstream collimators worsen the system performance in the dispersion suppressor. This observation, made in both vertical and horizontal planes, can be an evidence of the fact that carbon collimators are not suitable to absorb the channeled halo, therefore several are needed to obtain a reduction of losses in the DS.

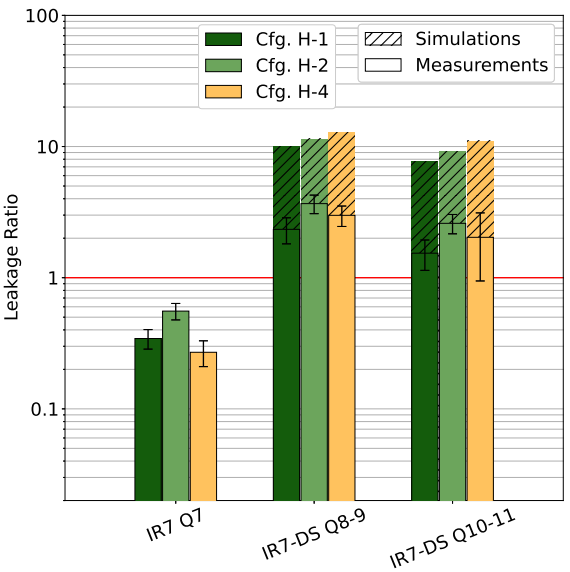

Fig. 46. (Color online) Leakage ratio with respect to standard collimation in several LHC locations, for proton beam at top energy. Measurements and simulations are shown by solid and dashed bars, respectively, for the horizontal configurations in Table 8. The red line shows the standard collimation reference: above the line the crystal collimation is improving the cleaning performance of the present system.

In Subsec. 6.3 it is pointed out that the horizontal crystal has a curvature radius close to the critical value for which channeling does not appear, and it is shown how this feature enhances the dechanneled particles at low deflection angle, with respect to the vertical crystals as shown in Fig. 41. Thus, more particles come out of the crystal with trajectories closer to the beam halo, and not properly deflected.[80] Secondary collimators placed at transversal aperture larger than the crystal are only able to intercept the deflected halo with a certain deflection.[73] Given a fixed aperture setup for crystals and secondary collimators, the range of the angular cut vary with the obstacle location and its optic functions. This might explain how the absence of a proper screen by the downstream secondary skews, enhances losses on Q7.[76,85] Moreover, the trend observed in both horizontal and vertical measurement, leads to the hypothesis that losses in the Q7 region are produced by hadronic showers produced in the very upstream TCLAs.

In simulations, an overall factor ~ 7 of improvement with respect to standard collimation is expected in every configuration presented, as shown in Fig. 46. The crystal routine in `SixTrack` is not optimized to simulate crystals close to the critical radius as the B1 horizontal crystal. This is discussed in detail in Refs. 76, 77 and 80.

6.6. *Cleaning measurements with heavy ions beam*

6.6.1. *Xenon ions*

The standard collimation system LMs (with nominal settings for the collimator hierarchy) were carried out as a reference for the comparison to the crystal-based system. The standard collimation leakage values are used as reference to evaluate the crystal-collimation performances in each one of the regions described in Subsec. 6.4.1. In addition, the region immediately downstream the DS, in the arc between points 7 and 8, where the quadrupoles 12 and 13 are located, was considered. A more complete description is presented in Refs. 76 and 86.

Given the observation obtained with proton beams about the enhanced dechanneling for B1 horizontal crystal, it was chosen to study the effect of the downstream collimators transverse aperture, as described in Table 10.

Table 10. IR7 collimators positions (in σ units) during flat top loss maps measurements with xenon ion beams for the B1 horizontal case.

	Standard collimation [σ]		Crystal collimation [σ]	
Collimator configuration	Nominal	Tight	#1	#7
TCPs	5.0	5.0	Out	Out
TCSG upstream	6.5	6.0	Out	Out
TCPCH.A4L7	Out	Out	5.0	5.0
TCSG downstream	6.5	6.0	6.0	6.5
TCLAs	10.0	6.0	6.0	10.0

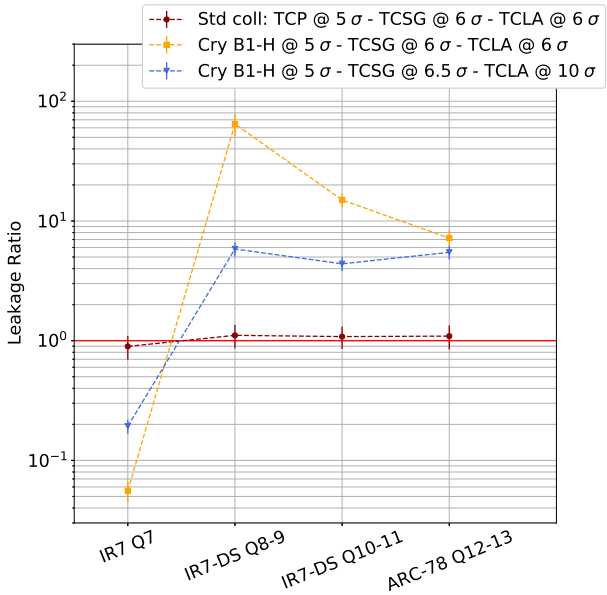

Fig. 47. (Color online) Leakage ratios with respect to standard collimation in LHC locations under study, for xenon ion beams at top energy. In this plot, the horizontal crystal is used to compare the nominal and the tight arrangement of downstream collimators with the configuration #1 and #7 described in Table 10. Also, the standard collimation system using tight setting is presented in the plot (solid brown bars). The red line shows the standard collimation reference: above the line the crystal collimation is improving the cleaning performance of the present system.

In particular, both secondary and absorber collimators were closed to only 1σ retraction with respect to the crystal aperture. This was done to optimize the collimation hierarchy downstream to match the B1 horizontal crystal characteristics, allowing the collimation system to catch a larger part of the deflected halo. In Fig. 47, the leakage ratio of standard collimation with tight settings and the crystal-collimation performance with both TCSGs and TCLAs at nominal and standard settings (that corresponds to Cfg#1 and Cfg#7 in Table 10), are presented. A summary of the cleaning performance obtained, once again expressed in terms of *ratio* of the *leakage factors* measured with crystal collimation to the ones measured with the standard system, is given in Table 11. While no significant difference is observed

Table 11. Collimation leakage ratio (standard versus crystal) for xenon beams, reported for each layout listed in Table 10.

	Leakage ratio			
Configuration	Q7	Q8–9	Q10–11	Q12–13
H–1	0.06 ± 0.01	64.61 ± 13.39	14.98 ± 2.03	7.20 ± 1.22
H–7	0.19 ± 0.03	5.83 ± 0.80	4.39 ± 0.58	5.47 ± 0.71

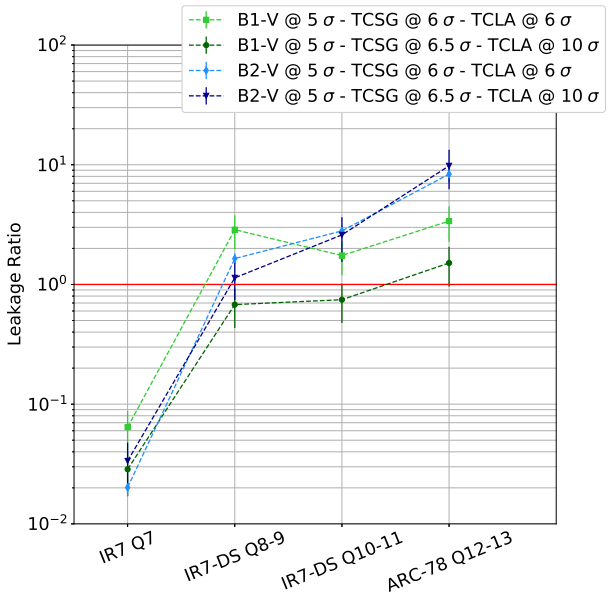

Fig. 48. (Color online) Leakage ratio with respect to standard collimation in LHC location under study, for xenon ion beams at top energy. The vertical crystals in B1 and B2 (both at 5σ aperture) are used with the tight (both TCSG and TCLA at 6σ) and nominal (TCSG at 6.5σ and TCLA at 10σ) configuration for downstream collimators. The red line shows the standard collimation reference: above the line the crystal collimation is improving the cleaning performance of the present system.

when the standard system is set to tighter aperture, the crystal-collimation system is observed to improve the LHC collimation with ion beams. The improvement is observed in any configuration, up to a factor ~ 60 when the tighter settings are used.

The same tests were carried out with two vertical crystals mounted in each of the LHC clockwise and counter-clockwise rings; both the crystals are QM. As already introduced, the QM crystals use a different orientation of the crystalline planes, the (111) planes. The (111) planes presents a pattern of two channels (where the smaller is 1/3 narrower than the larger), conversely to the horizontal crystal that uses the (110) planes that shows a single channel width. The crystal-collimation test results are summarized in Fig. 48 where leakage ratios with respect to the standard collimation are shown for crystal collimation in the vertical plane. The downstream collimators are set to nominal and tight settings (for both rings), as done for the horizontal plane. In general, only a slight improvement is observed in the vertical plane, i.e. less promising than for the horizontal case. Also, the tighter settings seem to not have the same effect on cleaning performances. Those crystals are not as close as the horizontal crystal to the R_c, and do not present the same high dechanneled population (see Subsec. 6.3). This might explain why tighter settings of downstream collimators do not improve — if not deteriorate — the cleaning

performance. Future studies should aim to understand if the noted difference might be induced by the diverse crystal technology, in particular the effect of the different crystalline planes width, when heavy ion beams are used.

6.6.2. *Lead ions*

In view of these measurements, crystal-collimation tests were performed also with lead ion beams.[87] The test was carried out with both high-intensity and low-intensity beams. The high-intensity beam tests were allowed only using upstream primaries and secondary collimators inserted close to the crystal aperture for safety reasons. This resulted in an improvement factor to standard collimation cleaning of ~ 10 for the B1H crystal, confirming observation made both in LHC and SPS (see previous paragraph and Subsec. 5.8) about the effect of upstream collimators on the crystal-collimation cleaning performance. Nevertheless, this test demonstrated that the crystal-collimation system was able to withstand the high intensity of LHC standard operation heavy ions beam.

Test with low-intensity beam, confirmed the observation made with Xe ions. In fact, an improvement larger than a factor ~ 100 was observed for the B1H crystal, when no upstream collimator was present and the full chain of carbon and tungsten collimators downstream was as close to crystal aperture. More specifically, this result was obtained with the carbon and the tungsten collimators were set to 1.5σ and 2σ retraction to the crystal aperture, respectively.

6.7. *Crystal-collimation operations in the LHC*

To deploy the system for standard operation the crystal collimation is required to be functional during dynamics phases of the machine cycle. One of the functionality tests carried out was to assess the reliability of crystal collimation during the beam energy ramp.[76,88] The energy ramp follows a nonlinear function made to safely increase the magnetic field strength in the machine. During this phase the critical angle for channeling changes, as well as the machine optics. This means the aperture and the orientation of the crystal must be continuously modified to keep the crystal in channeling orientation.

Specific functions were produced for the crystal goniometer and deployed in a special test (see Fig. 49(a)). To verify that the crystal was kept in channeling during the whole energy ramp were measured, the local losses at crystal and at the first collimator used to intercept the channeled beam. It is in fact observed that during tests with constant energy (both 450 GeV and 6.5 TeV) local losses at crystal were less than 1% of the losses at the first collimator. In Fig. 49(b), it is shown that the local losses at the crystal were kept below 1% of the ones at the collimator, proving that the crystal was successfully kept in channeling during the LHC energy ramp.

Crystal collimation was also deployed during special high-β^* physics runs.[89] These special runs were performed to allow the ATLAS (ALFA)[90] and TOTEM[91]

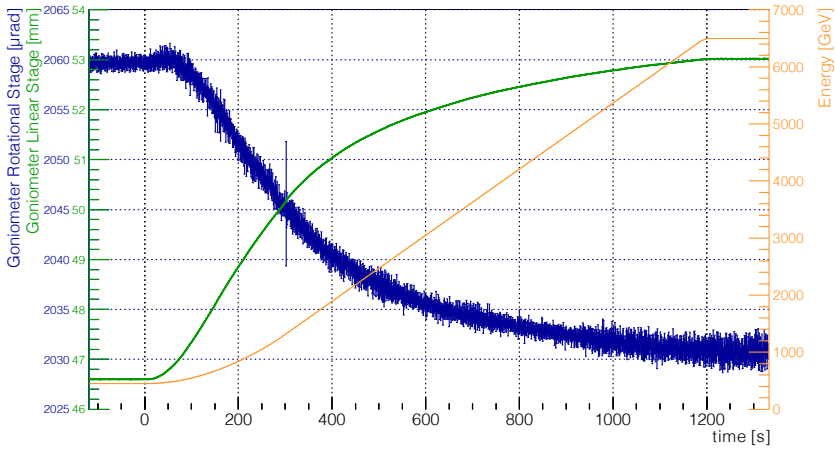

(a) Energy ramp function and goniometer stages position.

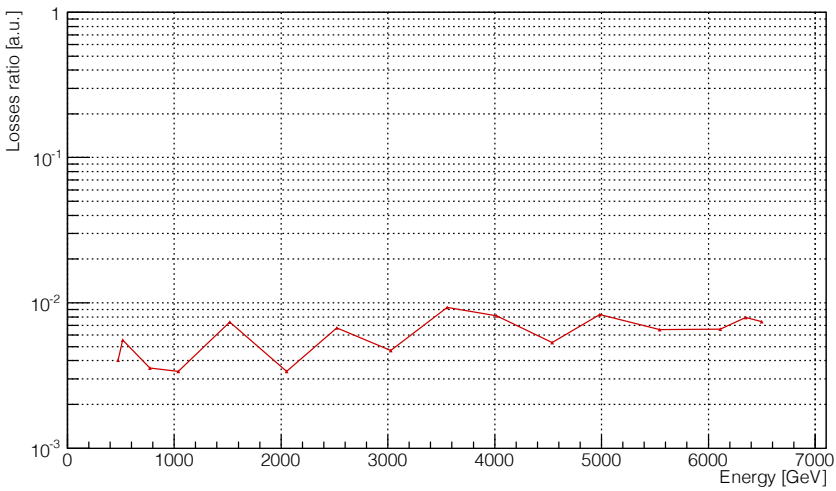

(b) Ratio of local losses.

Fig. 49. (Color online) In (a) the linear (solid green) and rotational (solid blue) stages position were recorded during the energy ramp (solid yellow). Data are averaged over a second (raw data rate 10 Hz), also RMS is calculated and shown as error bars. In (b) is presented the ratio of losses recorded at crystal and first collimator as a function of energy during the ramp for one of the crystals.

Collaborations to obtain data on the elastic scattering cross-section. The crystal-collimation system was observed to be reliable and stable during operations, more than the standard collimation system. The experimental background was observed to reduce when crystal collimation was in place, improving the collected data quality. Even though these special runs were carried out with low-intensity proton beams at 450 GeV, the results represent a milestone in terms of operational reliability of the crystal-collimation setup.

6.8. *Final consideration*

The LHC crystal-collimation experimental layout was extensively used to observe channeling of hadron at unprecedented energy and to assess the feasibility of crystal-assisted collimation system. Observation of channeling were made with several hadron species delivered in the LHC in the TeV energy range. The measurements were useful to understand the behavior of bent crystal close to the critical radius.

The crystal-collimation layout was used to evaluate and understand the performance of the system with both proton and heavy ion beams. It was clear that losses observed in regions not affected by betatron losses were due to the not proper absorption power of the collimators downstream the crystal, for such application. Tests with xenon ions highlighted how these losses came from showers due to the interaction of particles with both the crystal and secondary carbon collimators. It has also been observed that carbon collimators produce a large population of off-momentum particles that can be cleaned only by closing the shower absorber to their same aperture.

For proton beam operation a dedicated absorber needs to be studied to safely dispose of the beam halo deflected by a crystal, at the nominal circulating beam intensity. The design of this absorber can be driven by the observations presented in this work.

Nevertheless, the factor of improvement observed when crystal collimation is used with heavy ion beams is a clear indication that the system can withstand the energy load. This means that the system is ready to be deployed for ion standard operations.

7. Equation of Motion and Simulation Software

Particle motion in a crystal is governed by a complex equation of motion describing interactions with the ordered set of crystal atoms. A summary of the theoretical description is presented in App. B. Integration algorithms are used to identify numerical solutions for high-accuracy tracking code. Much faster Monte Carlo randomized approach, based on parametric definition of event probability densities, could emulate in a single algorithm the entire set of interactions felt by the particle during crystal traversal. Accurate formulae describe the electromagnetic field produced by atom arrays or planes in a crystal. Parabolic approximation of interplanar fields brings to harmonic equation of motion and useful scaling law that simplifies interaction description and solution finding with the Monte Carlo algorithm. Computer simulations, performed to describe beam halo behavior during crystal-assisted collimation tests, were based either on numerical integration or on Monte Carlo processing of the equation of motion. They often provided information for a deeper interpretation of the experimental data and sometimes were used to predict weakness of the setup and to investigate possible improvements of the hardware configuration.

Two distinct approaches, based on independent computer codes, were applied in SPS and LHC simulations. One was giving emphasis to the accurate computation of particle trajectories inside crystal and basing on very fast six-dimensional (6D) transfer matrix method the particle coordinate propagation along a few essential azimuths of the accelerator lattice.[58,92] The other was using fast Monte Carlo algorithm to provide the point-like description of crystal-particle interaction[93] and SIXTRACK tracking code[94] to propagate particle trajectories along the azimuth of each accelerator element. Indeed, high-accuracy simulations simultaneously applied in the crystal and along the accelerator, although possible, would have been prohibitive in terms of computing power for the large numbers of hardware configurations and initial conditions required in UA9. A large effort was devoted to mutually cross-check the tracking results and to compare them with experimental data recorded in the H8 line of the SPS North Area, with the crystals of Table 1.[95]

Additional routines, developed to extend simulations to more general environments, were coded using different descriptions of crystal-particle interactions. One was based on FLUKA,[96] another on GIANT4[97] and a third one on DYNECHARM numerical integrator.[98] They were also compared to H8 experimental data but never exploited during UA9 crystal-collimation studies.

7.1. *Monte Carlo algorithm for crystal-particle interaction*

In the Monte Carlo approach,[52,77,99] a probabilistic algorithm models the physics of the crystal-proton interaction using theoretical formulae with free parameters trimmed on experimental data. In order to calculate the probability for each particle to undergo a specific physical process, the crystal parameters and the particle coordinates at the crystal entry are also provided. Self-consistent but lengthy step-by-step particle tracking inside the crystal volume is no longer required. The Monte Carlo code developed in the frame of UA9 is applicable to protons interacting with silicon crystal strips or slabs with anticlastic or quasi-mosaic curvature with constant radius R. In the present version ion interactions, axial channeling, torsion modeling, showers of secondary emitted particles, radiative process and simulation of the holder geometry are not foreseen. In general, only horizontal curvature and horizontal motion is treated. For an over-barrier case, however, vertical motion is also considered. Finally, simulations for crystals with $R < 3R_c$ cannot be considered reliable because of the underestimated nuclear processes for such bending conditions.

The probabilistic algorithm computes separately interactions with bent crystals and scattering events with amorphous materials. The selection of the crystal-particle process is based on the value of θ_{in}, the impinging angle of the proton onto the crystal. If $\theta_{\text{in}} < \theta_c(R)$, channeling, dechanneling, or volume reflection events may occur. The probability of each realization is calculated and the final coordinates of the proton are randomly extracted accordingly. If $\theta_{\text{in}} > \theta_c(R)$, a similar calculation provides the probability that the occurring event is volume reflection,

volume capture, dechanneling after volume capture, or crystal traversal as amorphous material. If the proton moves over-barrier, the probabilistic selection of possible amorphous interactions includes multiple Coulomb scattering, single diffractive, nucleus–proton elastic, proton–proton elastic, Rutherford and deep inelastic events. The angular deflection given by scattering and the ionization energy loss are applied to any impinging proton, depending on its impact parameter.

Single diffractive and nuclear elastic scattering are particularly prone in producing leakage from crystal-assisted collimation system, thereby limiting its cleaning performance. Energy loss by ionization unavoidably brings escaping particles into the dispersive area of the accelerator, producing highly detrimental energy deposition. Care is thus needed in implementing accurate descriptions of cross-section of these events. Improvements of the present version of the algorithm consist in the implementation of the correlation between kick and energy loss in single diffractive events, in the use of a more accurate cross-sections of nuclear events and of the relative energy scaling, in the better choice of the free parameters of nuclear elastic events, and in the implementation of Rutherford scattering. In computing dE/dx, the Bethe–Bloch formula at 400 GeV is used. Moreover, to take into account the ultra-relativistic $\beta\gamma$ regime in which the particle hit the crystal, the probability of ionization losses in the long tail of the Landau distribution is included as well.

The Monte Carlo algorithm, very fast and suitable for high-statistics estimates, is in fact an emulator of crystal-particle interaction. Realistic result requires to introduce free parameters in some cross-section formulae and to fine tune them by comparing the simulations with experimental data, specifically collected in the SPS North Area with 400 GeV protons.[34,36] The cross-sections trimmed at 400 GeV are extrapolated to higher-energy regime, whenever needed. The parametric approach, extensively described in Ref. 77, is exemplified hereafter.

If $\theta_{\rm in} < \theta_c(R)$, the assumed probability of capture in channeling states is empirically reproducing analytical estimate of the channeling efficiency, for a wide range of crystal parameters:

$$P_{\rm CH} = \frac{\sqrt{\theta_c^2(R) - \theta_{\rm in}^2}}{\theta_c(R)}\,, \tag{1}$$

that can be expanded in the form

$$P_{\rm CH} = \left(1 - \frac{R_c}{R}\right)\sqrt{1-k^2}\,, \tag{2}$$

where $k = \theta_{\rm in}/\theta_c(R)$ is the ratio of the initial to the critical angle. Equation (2), applied to a collinear beam perfectly aligned to a straight crystal, provides the unrealistic result $P_{\rm CH} = 1$. To correct this, the trimmed form adopted is

$$P_{\text{CH-trim}} = \left(1 - \frac{R_c}{R}\right)\sqrt{0.9(1-k^2)}\,. \tag{3}$$

To decide how a channeling event evolves, a random number n_r is extracted with flat probability $\in [0,1]$. If $n_r < P_{\text{CH-trim}}$, channeling state along the entire crystal length

is assumed. Alternatively, the process is classified as belonging to the intermediate region between amorphous and VR, where the trimmed deflection depends on the linear interpolation between the average MCS angle, equal to zero, and the VR angle:

$$\Delta\theta_{\rm trim} = 0.45(1+k)\theta_{\rm VR}\,. \tag{4}$$

The total particle deflection results from the sum of the value provided by (4) and the MCS angle, obtained by a randomized algorithm.

In volume reflection events, the average deflection and the angular dispersion are expressed as:[100]

$$\theta_{\rm VR} = c_1\theta_c(R)\left(1 - c_2\frac{R_c}{R}\right), \quad \Delta\theta_{\rm VR} = c_3\theta_c(R)\frac{R_c}{R}\,. \tag{5}$$

For strip crystals bent along the (110) planes, the optimally trimmed values of the free parameters are: $c_1 = -1.5$, $c_2 = 1.7$, $c_3 = 1.7$, $k_{\rm VC} = 7\times10^{-4}$. For quasi-mosaic curvature along the (111) planes c_1 is decreased by 7% and c_2 is increased by 5%.

Particles in channeling states, with $n_r < P_{\text{CH-trim}}$, can still be dechanneled before the crystal ends. The intensity of channeled particles decreases exponentially with the path length, because of MCS on electrons. The e-folding constant is

$$S^e_{\rm dec} = \frac{256}{4\pi^2}\frac{pv}{\ln\left(2m_ec^2\gamma/I\right)}\frac{a_{\rm TF}d_p}{r_em_ec^2}\times\left(1-\frac{R_c}{R}\right)^2, \tag{6}$$

where r_e and m_e are the classical radius and the rest mass of the electron, $a_{\rm TF}$ is the screening length in the Thomas–Fermi approximation defined in App. B, $I \simeq 172$ eV for silicon (a value slightly higher than in Eq. (B.21)). The used value of the e-folding constant for nuclear interactions is

$$S^n_{\rm dec} = \frac{1}{200}\times S^e_{\rm dec}\,. \tag{7}$$

Only 10% of the protons were assumed as potentially affected by the nuclear e-folding, as the ratio of nuclear corridor by channel widths suggests. The position of the dechanneling event is given by the expression $L_{\rm dec} = -S^e_{\rm dec}\times\ln(r)$ where r is again a random number $\in[0,1]$. If $L_{\rm dec} < L$, the proton proceeds in channeling states up to the length $L_{\rm dec}$ and in amorphous state afterwards. If $L_{\rm dec} \le L$, the proton is in channeling states for the entire crystal length.

At the crystal exit, the coordinates of a channeled particle are

$$\begin{aligned} x' &= \theta_b + \theta_c(r)r_g/2\,, & x &= x_0 + L\sin(x'/2+\theta_m)\,,\\ y' &= y'_0\,, & y &= y_0 + Ly'\,, \end{aligned} \tag{8}$$

where r_g is a random number with normalized distribution.

Volume reflected particles obey two conditions $\theta_{\rm in} \le \theta_c(R)$ and $L_{\rm VR} = R\theta_{\rm in} \le L$. The latter prescribes that the point of VR event occurs inside the crystal length L.

If $L_{\mathrm{VR}} > L$, the particle is in an amorphous state along all the crystal lengths. The VR trajectory obeys

$$\begin{aligned} x &= x_0 + x' L_{\mathrm{VR}}\,, & y &= y_0 + y'_0 L_{\mathrm{VR}}\,, \\ x' &= x'_0 + \theta_{\mathrm{VR}} + r_g \Delta\theta_{\mathrm{VR}}\,, & y' &= y'_0\,, \end{aligned} \tag{9}$$

where r_g is a random number with normalized distribution and where θ_{VR} and $\Delta\theta_{\mathrm{VR}}$ are given by (5).

Volume captured particles are treated as particles in channeling states that will cross only a fraction of the crystal curvature, with finite probability of being further dechanneled. The probability of the volume capture process is

$$P_{\mathrm{VC}} = k_{\mathrm{VC}} \left(\frac{R}{R_c} - 0.7 \right) E^{0.2}, \tag{10}$$

where k_{VC} is a trim constant.

7.2. *Monte Carlo simulations versus experimental data*

In the Monte Carlo approach,[59,99] probability distributions randomly sampled determine the particle trajectory modification due to crystal traversal. Free parameters embedded in the interaction cross-section formulae are optimally trimmed on the observed process. Simulation results are finally compared to a representative set

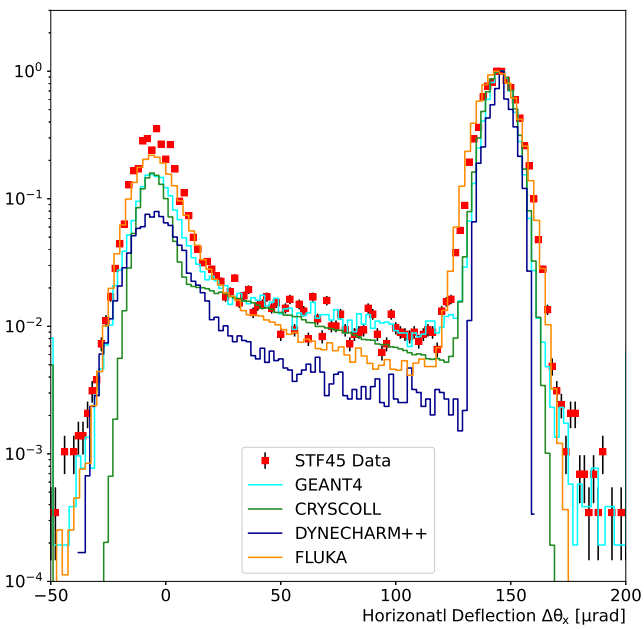

Fig. 50. (Color online) Angular distribution of crystal STF45: deflected particle density, normalized to the peak value of the experimental data as a function of the horizontal deflection due to the crystal traversal.

Table 12. Crystal SFT45: comparison of the experimental data with simulations (updated from Ref. 36).

	θ_b [μrad]	$\eta_{\rm CH}$	$L_{\rm dec}$ [mm]
Exp. data	143.78 ± 0.07	0.689 ± 0.005	1.41 ± 0.14
DYNECHARM	144.35 ± 0.04	0.769 ± 0.008	1.05 ± 0.12
GEANT-4	144.25 ± 0.03	0.744 ± 0.007	1.95 ± 0.19
CRYSCOLL	144.40 ± 0.01	0.799 ± 0.001	1.08 ± 0.01
FLUKA	143.94 ± 0.01	0.759 ± 0.001	1.43 ± 0.05

of experimental data, collected with the crystals in Table 1, to assess predictivity of the algorithm.[34,36,77]

An example of the comparison is shown in Fig. 50. The crystal SFT45 is irradiated with 400 GeV protons and incoming and outgoing trajectories are recorded with the telescope in Fig. 1. Only particles with incident direction parallel to the entry crystal planes within ± 5 μrad are selected. The flux of deflected protons is shown as a function of the recorded deflection, normalized to the peak recorded flux. In Fig. 50, the experimental data are shown as red dots and the simulation data as solid lines. Those of the Monte Carlo algorithm (CRYSCOLL) are shown in green, those of the GEANT-4 routine in light-blue, those of the routine DYNECHARM in dark-blue and those of FLUKA in dark-orange. Quantitative comparison produces the results of Table 12.

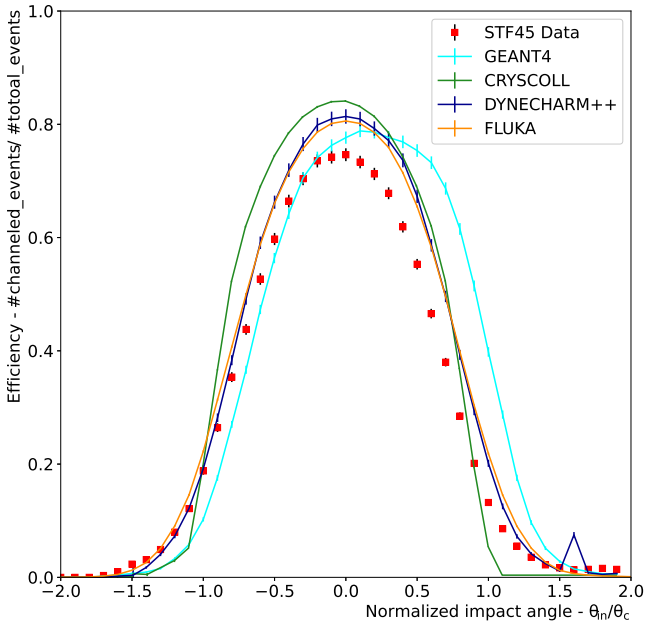

Fig. 51. (Color online) Angular distribution of crystal STF45: channeled particle density, normalized to the total number of events as a function of the incoming angle $\theta_{\rm in}$, normalized to θ_c.

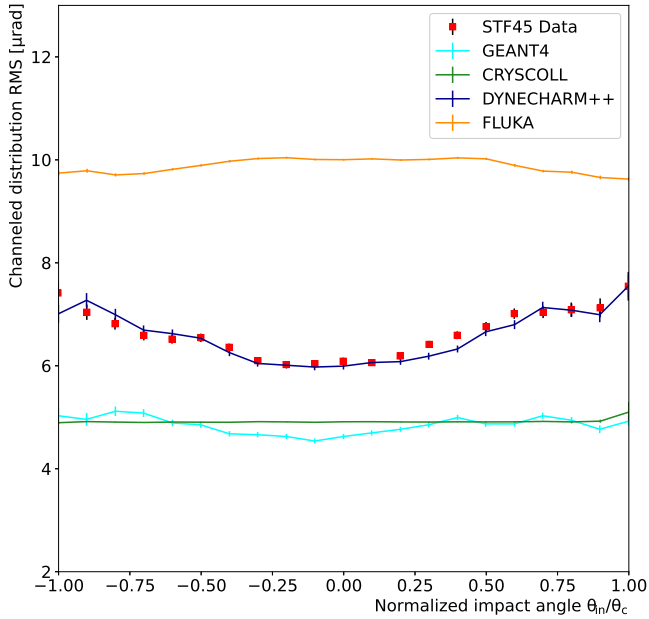

Fig. 52. (Color online) Angular distribution of crystal STF45: RMS variation of the channeled particle deflection as a function of the incoming angle $\theta_{\rm in}$, normalized to θ_c.

Probability density of particles in channeling states as a function of the crystal entry angle, normalized to the critical angle, is shown in Fig. 51. The simulation routines overestimate the channeling population, in particular in the angular range around $\theta_{\rm in} = 0$, and the average bending angle (see also the first column of Table 12). The curve obtained with CRYSCOLL has sharp edges, because of the compelling condition for channeling $\theta_{\rm in} < \theta_c$. Considering thinner slices of channeled particles as a function of the entry angle, one finds, for each routine, a linear dependence of the average deflection on incident angle, very well correlated to experimental data, within the experimental errors. The spread of the deflection, instead, has a weak correlation with the data, except for the DYNECHARM case, as shown in Fig. 52. In particular the plot relative to CRYSCOLL is flat, because the estimated deflection spread is Gaussian with RMS equal to $\frac{1}{2}\theta_c$, uncorrelated to the entry angle.

Probability density of dechanneled particles as a function of the crystal entry angle, normalized to θ_c is illustrated in Fig. 53. The trend identified with CRYSCOLL is regular, with sharp edges for $\theta_{\rm in} = \theta_c$, because the coded value of e-folding dechanneling length is the same for all entry angles. The trends given by DYNECHARM and FLUKA have a shape similar to that of experimental data, but the dechanneling probability density is underestimated in the range $\theta_{\rm in} \in [-\theta_c, \theta_c]$. The trend computed by the GEANT-4 routine is asymmetric, because of the assumed particle distribution density in the channel.

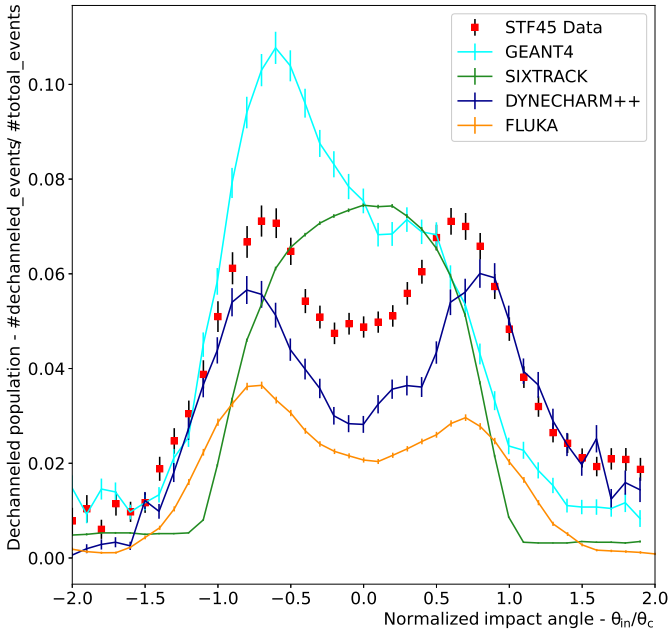

Fig. 53. (Color online) Angular distribution of crystal STF45: dechanneled particle density, normalized to the total number of events as a function of the incoming angle $\theta_{\rm in}$, normalized to θ_c.

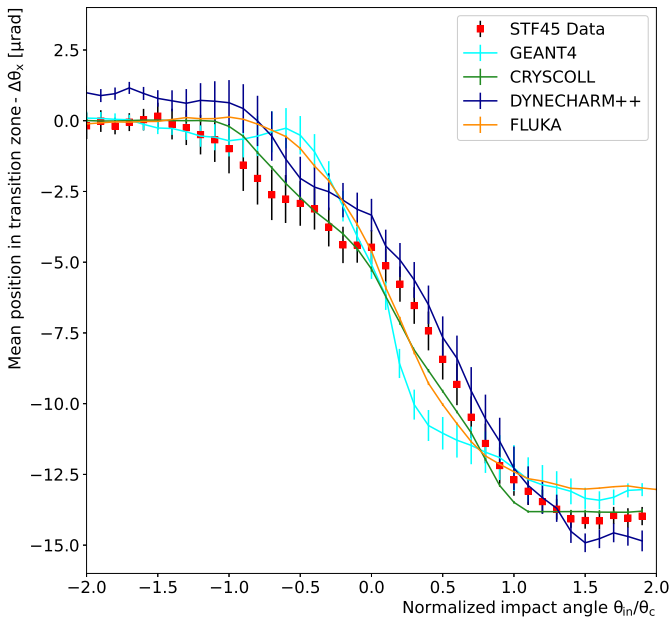

Fig. 54. (Color online) Angular distribution of crystal STF45: average deflection in the transition from AM to VR regime as a function of the incoming angle $\theta_{\rm in}$, normalized to θ_c.

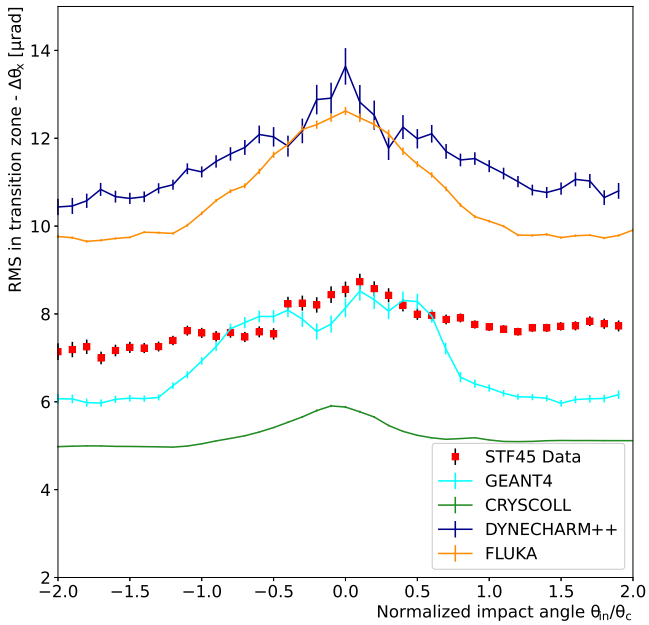

Fig. 55. (Color online) Angular distribution of crystal STF45: RMS deflection in the transition from AM to VR regime as a function of the incoming angle $\theta_{\rm in}$, normalized to θ_c.

Probability density from the edge of the amorphous regime to the onset of volume reflection is fixed by empirical formulae and needs careful comparison with experimental data. Average and RMS deflection as a function of incoming angle are shown in Figs. 54 and 55, respectively. Average deflection is very similar to experimental data for all simulations, while RMS fluctuation is in weak agreement.

It is important to consider that the experimental data are convoluted to the telescope accuracy, whilst the numerical simulations are not suffering instrumental inaccuracy. Simulation results weighted with the same inaccuracy of the experimental data, are affected by considerably reduced discrepancy. In particular, CRYSCOLL estimate of channeling efficiency becomes $\eta_{\rm CH} = 0.685 \pm 0.005$, a value fully compatible with the experimental one in Table 12.[59] At the same time, the RMS deflection of channeled particles in Fig. 52 and of the transition region in Fig. 55 become closer to the data values. Simulation results and experimental data of the other crystals of Table 1 are discussed in Ref. 36. Their trend is similar to the one of crystal STF45, discussed here. New results from FLUKA routine have recently been published[101] and compared with experimental data obtained by UA9.

7.3. *Tracking of the particle trajectory in SPS and LHC*

Particle motion in circular accelerators, governed by Courant and Snyder equations, is described by approximate solutions, relying on Twiss functions, phase space integral of motion and transfer matrices of canonical coordinates.[102] Tracking

code is the privileged tool to simulate long-term behavior of large sets of particles. SIXTRACK,[94] developed and upgraded for many decades, is the advanced code preferentially used at CERN[103,104] for numerical simulation in large accelerators. Specific approximations model the lattice to speed-up computation. Thin-lens approximation allows replacing thick magnets by pointlike lenses with the same integrated strength. Advantages and limitations are discussed in Ref. 105. Hard-edge approximation of the magnetic field implies suppressing the fringe field at the magnet extremities, thereby violating Maxwell's equations and symplecticity of motion. Consequences and applicability field of the assumption are presented in Ref. 106. Small-angle approximation, holding for $p_{x,y} \ll p$, allows expanding the equation of motion in powers of $p_{x,y}/p$, greatly simplifying first-order solutions. The combination of previous approximations easily provides 6D matrices to describe the motion in linear elements of the accelerator, such as drift spaces, dipoles, quadrupoles and RF cavities, by a simple and very accurate formulation, greatly reducing the simulation computing time.

Particle tracking in the SPS applies linear 6D transport matrices between four critical azimuths, where the crystal, the secondary absorber, the first high-dispersion area downstream the crystal and the radio-frequency cavity are, respectively, located. The crystal-particle interaction is accurately described by a numerical integrator of the equation of motion (B.23), applying Eq. (B.15) to account for diffusion due to electron scattering and Eq. (B.20) to account for nuclear scattering. The particle-absorber interactions are described by Bethe–Bloch and nuclear interaction cross-sections and radiation length e-folding in tungsten. The coordinate marker in the high-dispersion area is used to sample the trajectories of particles with reduced energy and the RF-cavity region to compute the particle momentum increase due to electromagnetic accelerating field, according to

$$\delta = \delta_0 + \frac{eV_{\mathrm{RF}}}{E_0} \sin\left(\pi + \frac{2\pi h \ell}{C_0}\right), \tag{11}$$

where E_0 is the energy of the synchronous particle, V_{RF} and h are the amplitude and harmonic number of the accelerating voltage, ℓ is the longitudinal deviation of the particle in the bunch and C_0 is the orbit length. The tracking history ends by nuclear inelastic interaction either in the crystal or in the absorber.[56,58] The initial distributions of the transverse and longitudinal coordinates is generated at the crystal azimuth. The longitudinal coordinates (δ, ℓ) follow Gaussian distribution, with $\sigma_\ell = 0.18$ m and $\sigma_\delta = 0.6 \times 10^{-3}$, respectively, in agreement with the longitudinal bunch shape recorded during the data-taking runs. Initial conditions of each particle are chosen at distance δx_0 from the crystal edge, with the initial betatron and synchrotron amplitudes, x_0 and δ_0, respectively, satisfying the condition

$$x_0 + \delta x_0 = |x_{\mathrm{cr}}| - |D_x \delta_0|\,, \tag{12}$$

where x_{cr} is the crystal edge distance from the beam center and D_x is the horizontal dispersion at the crystal position. The value $\delta x_0 = 30$ μm is chosen for simulation

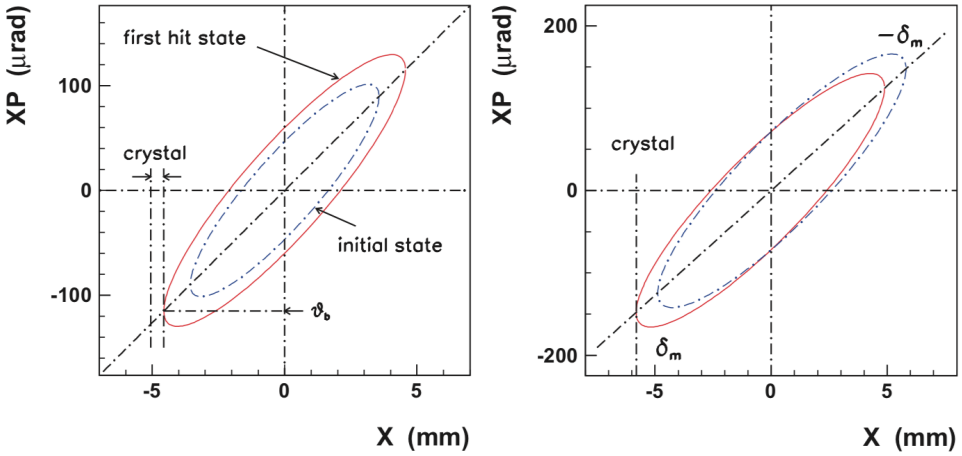

Fig. 56. (Color online) Phase space in the SPS: (a) synchronous and (b) off-momentum tracked particles driven by diffusion and synchrotron motion. Initial trajectories (dot-dashed blue ellipses), first hit ones (solid red ellipses) and crystal position (dot-dashed line) are shown.

in SPS. The initial betatron phase is randomly selected with uniform probability in the interval $\vartheta_0 \in [0, 2\pi]$. An example of such particle is shown in Fig. 56. The top image (a) shows the initial trajectory of the on-energy particle with $\delta = 0$ (dot-dashed ellipse in blue). Amplitude diffusion, due to interactions with the residual gas or artificially induced by electronic noise, brings the particle to collide with the crystal edge. At the collision point, where $\vartheta_b \simeq \pi$, the phase space trajectory is represented by the red ellipse. The bottom image (b) represents the same dynamical evolution for off-momentum particle with $\delta \neq 0$. The dot-dashed ellipse in blue represents the phase space for $\delta = -\delta_m$ and the red ellipse that for $\delta = +\delta_m$, where δ_m corresponds to the peak momentum offset during the synchrotron oscillation. On-momentum particle trajectory shown in Fig. 56(a) is an asymptotic idealization, because the probability density around $\delta \simeq 0$ is negligible. Almost all the halo particles have some momentum deviation δ, which leads to amplitude modulated trajectory shift $x_\delta(t) = D_x \delta_m \sin(\omega_{\rm rev} Q_s t + \varphi)$, where Q_s is the synchrotron tune, $\omega_{\rm rev}$ the angular revolution frequency, φ the initial synchrotron phase. The two trajectories in Fig. 56(b) correspond to the maximum and the minimum of the synchrotron oscillation, respectively. For $V_{\rm RF} \simeq 1.5$ MV, generally used during the UA9 runs, for $\delta = \sigma_\delta$ the synchrotron period $T_s = \frac{2\pi}{\omega_{\rm rev} Q_s}$ becomes $T_s \simeq 150 T_{\rm rev}$, where $T_{\rm rev} = \frac{2\pi}{\omega_{\rm rev}}$ is the revolution period.

In linear approximation, close to the crystal edge, at about $6\sigma_x$ from the beam center, the average speed of amplitude oscillation growth, measured in the UA9 runs and applied in tracking simulations, is $\langle \dot{x} \rangle \in [2.2, 8.8]$ μm/s, corresponding to $\delta x_{\rm rev} \in [0.5, 2]$ nm per revolution period $T_{\rm rev} = 23$ μs and to $\delta x_s \in [75, 300]$ nm per synchrotron period $T_s = 3.5$ ms. At the crystal azimuth, for $\delta = \sigma_\delta = 0.6 \times 10^{-3}$,

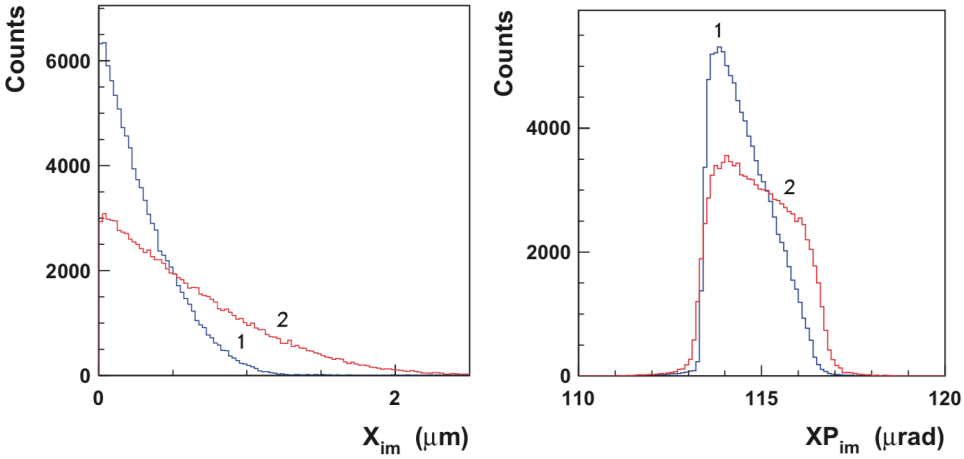

(a) (b)

Fig. 57. The distributions of impact parameters (a) and angles (b) at the first crystal hit, for $\langle \dot{x} \rangle = 2.2$ μm/s (1) and $\langle \dot{x} \rangle = 8.8$ μm/s (2).

the maximal trajectory shift from the orbit is $\hat{x}_\delta = D_x \sigma_\delta = 0.47$ mm, a value three orders of magnitude greater than δx_s. The first hit with the crystal thus occurs when the particle amplitude-phase vector in the synchrotron phase space is near $(\delta_m, 0)$ and the betatron oscillation phase near $\varphi = \pi$. The impact parameter distribution becomes considerably larger than the average amplitude increase per turn. Figure 57 shows the distribution of impact parameter (a) and angle (b) of the particle at the first crystal hit. In Case 1, $\langle \dot{x} \rangle = 2.2$ μm/s and, in Case 2, $\langle \dot{x} \rangle = 8.8$ μm/s, respectively assumed. In Case 1, the resulting distributions have an average impact parameter $\langle b \rangle = 0.28$ μm and an impact angle FWHM $\simeq 2.2$ μrad, much smaller than θ_c. A slightly worse situation holds also for Case 2, where the impact distributions are larger. High channeling efficiency should be possible in both cases.

8. Conclusion

The successful construction and operational tests of the crystal-assisted collimation prototype setups in SPS and LHC have fully demonstrated the feasibility of crystal-assisted collimation in hadron colliders.

Acknowledgments

The effort of the UA9 Collaboration was strongly supported by the funding agencies. We also acknowledge partial support by the European Community-Research Infrastructure Activity under the FP6 "Structuring the European Research Area" program (CARE, Contract No. RII3-CT-2003-506395), the EuCARD program GA 227579, within the "Collimators and Materials for high power beams" work

package (Colmat-WP), the EU FP7 "HiLumi LHC" Grant Agreement 284404, the ERC Ideas Consolidator Grant No. 615089 "CRYSBEAM"; the INTAS-CERN collaborative Project No. 05-103-7525; the Italian Ministry of the Research for the MIUR Project No. 2006028442, the FIRB Grant No. RBFR085M0L-001/I11J10000090001, the PRIN No. 2008TMS4ZB, the Grants RFBR-CERN Nos. 08-02-91020 and 12-02-91532; the INFN NTA-HCCC Program; the Russian Foundation for Basic Research Grants Nos. 05-02-17622 and 06-02-16912, the Council of the President of the Russian Federation for the Grants Nos. NSh-3057.2006.2, SS-3383.2010.2 and SS-1633.2014.2, the "Physics of Elementary Particles and Fundamental Nuclear Physics" program of the Russian Academy of Sciences, the "LHC Program of Presidium of Russian Academy of Sciences"; the US DOE under the LHC Accelerator Research Program (LARP), the project ADTP No. 2.1.2/13162; the UK Science and Technology Research Council.

A special thanks to the SPSC referee teams that provided suggestions and encouragement over the last decade.

We wish to acknowledge the CERN BE-OP team in charge of setting up the SPS and of the H8 beams during the data taking, the CERN EN-STI, EN-MME and BE-ABP groups for the strong support.

Appendix A. Crystal Design Optimization and Fabrication

In the early 1990s, crystals started to be intensively exploited in circular accelerators in RD22 at CERN[107] and in E853 at FNAL.[108] They were cut from dislocation-free silicon ingots with horizontally elongated rectangular shape and with larger faces, parallel to the (110) crystalline planes, properly etched and optically polished. The plates were clamped on multi-point bender to impart them the desired curvature. Such a simple bending mode, although very effective and inexpensive, was prone to induce a horizontal curvature varying with the vertical coordinate and a flat shape at the plate extremities (details of the RD22 crystals are discussed in Ref. 15 and those of the E853 crystal in Refs. 19 and 109). A side effect of the imperfect geometrical shape was the reduction of channeling efficiency and the consequent increase of dechanneling and nuclear interaction rates. In order to mitigate the anticlastic reaction of the crystal plate to multi-point mechanical torque, U-shaped crystals, with the slab and the legs cut as one single self-supporting piece, bent by two screws pressing the legs, were introduced in RD22. Although laser-based measurements indicated a substantial improvement from this new bending technique,[110] RD22 tests did not record significant changes of channeling efficiency.[107,111]

Investigations of the late 1990s, demonstrated that short crystals of a few mm length would considerably increase halo deflection efficiency and enhance multi-turn mechanism of capture into channeling states. Particles not captured in channeling state at the first crystal encounter suffer small deflection by MCS, because of the short crystal length. In successive turns, interactions at a small angle with the crystal could happen again, in which channeling might occur.[16,20,21,112] As a general rule, the smaller the crystal length and the MCS angle per crystal crossing, the

larger will be the probability of multi-turn capture in channeling states. The drawback is that shorter crystals can achieve smaller bending angles θ_b, for the same radius of curvature. One of the first achievements along this line was the short O-shaped crystal build at PNPI and used for crystal-assisted extraction tests at IHEP in U70.[113] It was cut from a monolithic silicon ingot in "O" shape with sizes of $0.6 \times 5 \times 5$ mm^3, bent by 440 μrad. As shown in Fig. A.1, the curvature was imparted by compression in the middle part of larger crystal faces. The bend part

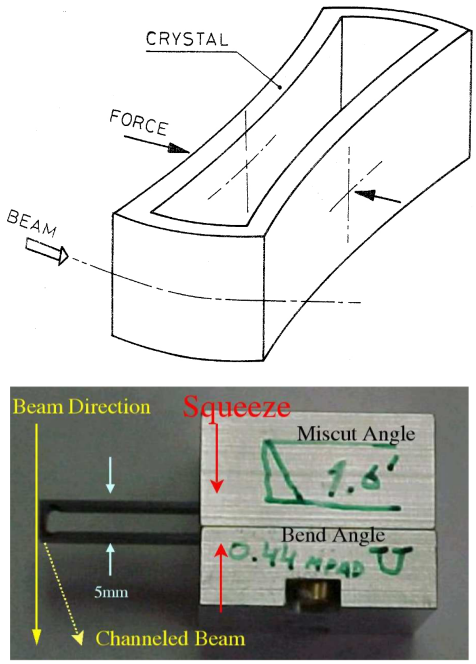

Fig. A.1. O-shaped crystal used at U70 in IHEP, at RHIC and at the Tevatron. Schematic view (top) and real crystal (bottom).

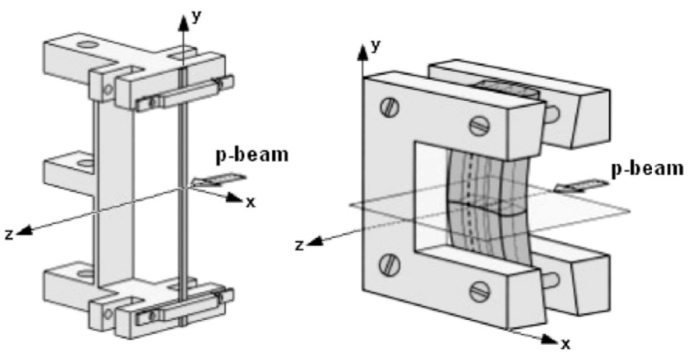

Fig. A.2. Schematic view of the strip (left) and quasi-mosaic (right) crystals clamped in their holders.

was 3 mm long and the straight ends 1 mm each. Such a conceptual design was intrinsically better for higher channeling efficiency, even if the issue of flattish shape of the edges remained unsolved. Although available too late for RD22 and E853, the U70 crystal was reused at RHIC and later in the initial collimation test of the T980 experiment at the Tevatron.[11]

Bending methods, better exploiting the elastic response of crystal to external flexural stress, systematically investigated from the beginning of the 2000s, could finally provide a substantial improvement. Strip crystals (see Fig. A.2) a few cm long by a few mm thick, clamped by the ends to a C-shaped holder were assembled for the first time by Yu. Chesnokov and collaborators at IHEP. By imparting a curvature to the long side of the strip, an anticlastic reaction was produced with a saddle point in the middle of the strip and a quasi-circular curvature along the short side. Such a clever concept is illustrated in detail and experimentally demonstrated with data collected in U70 at IHEP in Ref. 114. The crystal strip is cut parallel to a layer of crystal planes, preferably the (110) planes that provide consecutive channels of equal width. The mechanical cut generally produces a superficial layer with a large number of defects and crystalline disorder and a residual miscut angle θ_m of the crystal faces with the crystallographic planes. The amorphous layer, ineffective for channeling, can be reduced by optical polishing. For a more effective result, the controlled chemical etching of the crystal surface could also be performed.[115] In circular accelerators, beam manipulations assisted by bent crystals ideally require that the crystalline planes are perfectly aligned with the lateral face exposed to halo particles. In real crystals, a nonzero angle between the lateral face and the planes is however unavoidable because of the finite precision of the cutting procedure. A minimal miscut angle helps in maximizing the crystal portion available for full θ_b particle deflection by channeling, and in making simpler the optical pre-alignment of crystal with respect to the accelerator reference. A high-precision Magnetorheological Finishing (MRF)[116] of the crystal surface exposed to the beam halo should help in minimizing the miscut angle.[117] The MRF procedure consists in introducing the crystal into a fluid, whose viscosity may change by several orders of magnitude when activating a magnetic field. Thanks to the friction with the high viscosity fluid, a local shear-based material removal from the crystal surface can take place. By iterating measurements of the miscut angle, based on a high-resolution X-ray diffractometer assisted by an autocollimator, with successive MRF treatments, the miscut angle could be eventually minimized. The flexural stress that the frame imparts to the strip crystal should be symmetric to prevent a torsional reaction that would modify the trajectory of the channeled particle with the vertical coordinate of the impact point. Two independent solutions were proposed. At INFN-Ferrara, the parallelism of the clamping edge was adjusted using micrometric screw to compensate the torsion recorded during the crystal characterization with X-ray diffractometer.[117] At PNPI, a very rigid frame was built and machined with high-precision shape to impose parallelism of clamping and of crystal strip ends to within a few μrad tolerance.[118] The strip crystals for the SPS tests were clamped on

Table A.1. Crystals for the collimation studies in the CERN accelerator complex.

SPS crystals	Origin	$L \times W \times H$ [mm^3]	θ_b [μrad]	R_b [m]	Torsion [μrad/mm]	θ_m [μrad]	Date In	Date Out	Notes
STF09	INFN	$2.00 \times 0.5 \times 70.0$	150	13.33	?	<170	2009.12.10	2011.01.06	strip
QMP15	PNPI	$1.98 \times 18.0 \times 13.1$	140	14.11	8	<100	2009.12.10	2010.05.31	QM
QMP15B	PNPI	$1.60 \times 18.0 \times 15.0$	150	10.67	2	43	2010.08.30	2011.01.06	QM
QM25-SPS	PNPI	$2.10 \times 30.5 \times 57.5$	165	12.73	1	92	2010.01.14	2015.01.12	QM
STF18	INFN	$2.00 \times 0.5 \times 70.0$	176	11.36	0.6	200	2010.01.14	2019.01.21	strip
STF49	INFN	$0.80 \times 0.5 \times 55.0$	270	2.96	?	<170	2012.01.10	2012.09.10	strip
QMP32	PNPI	$0.96 \times ? \times ?$	175	5.49	<2	<40	2012.01.10	2012.09.10	QM
MSTF16	INFN	$1 \cdot 16 \times ? \times ?$	714	1.4	?	?	2012.09.10	2014.04.22	16 strip
STF81	INFN	$1.87 \times 0.5 \times 55.0$	165	11.33	?	10	2014.04.25	2019.01.21	strip
QMP35	PNPI	$0.47 \times ? \times ?$	175	2.68	<2	<20	2014.04.25	2017.03.06	QM
MSTF13	INFN	$1.28 \cdot 8 \times 1 \times 55$	600	2.13	?	?	2012.09.10	2014.04.22	8 strip
LHC crystals	**Origin**	$L \times W \times H$ [mm^3]	θ_b [μrad]	R_b [m]	Torsion [μrad/mm]	Miscut [μrad]	Date In	Date Out	Notes*
STF75	INFN	$4.00 \times 0.5 \times 55$	50	80.00	?	<10	2014.02	2019.03	strip B1 H
QMP34	PNPI	$4.00 \times 6.5 \times 27$	47	85.11	<1	<20	2014.02	2019.03	QM B1 V
QMP52	PNPI	$4.00 \times 6.5 \times 27$	50	80.00	<1	<54	2017.02	2018.02	QM B2 V
QMP53	PNPI	$4.00 \times 6.5 \times 27$	50	80.00	<1	<55	2017.02	2019.03	QM B2 H
TCP76	PNPI	$4.00 \times 1.5 \times 54$	50	80.00	<1	<50	2018.02	2019.03	strip B2 V

*B1 (B2) indicates the crystal insertion in beam 1 (beam 2) of LHC; H (V) indicates the horizontal (vertical) plane.

massive frames in aluminum to guarantee a very stable shape. Such a design was inappropriate for the LHC, because of the too large emissivity of the aluminum, potentially prone to activate the electron cloud process.[41] Frames made in titanium grade V were thus adopted, of total weight not exceeding 90 g, fully compatible with the requirements of the LHC angular actuators, able to mitigate the electron cloud effect, because of their reduced emissivity. Such a design change had the adverse consequence of reducing the mechanical stability of the frame during the thermal cycles requested by the high-vacuum protocol of LHC components. Because of this, the number of crystal-frame samples produced at the INFN-Ferrara was greatly increased to statistically select the most stable of them.[119]

Quasi-mosaic (QM) effect is a 3D elastic reaction to the main curvature of crystal plate, discovered by Sumbaev at PNPI in the late 1950s.[120–122] A rectangular thin plate crystal, bent in cylindrical shape along its major axis by a C-shaped frame, will exhibit anticlastic reaction along its minor axis and quasi-mosaic reaction along its thinner faces that can be a few tenths of mm long or more, along the beam direction.[123] Silicon crystals of this type, with the thin faces parallel to (111) crystalline planes, produced at PNPI, were tested in the North Area and used in the SPS and in the LHC.[35,38,73,118]

Short crystals, optically or chemically polished, with constant curvature obtained through anticlastic or quasi-mosaic elastic reaction, schematically shown in Fig. A.2, were extensively tested in the extracted beam lines of the SPS North Area with 400 GeV protons. A subset of them, listed in Table A.1, was used for collimation tests with protons and heavy-ions in the SPS and LHC. Two multi-strip crystals, the MSTF13 and MSTF16, included in the table for the sake of completeness, could not yet be exploited in collimation mode. Their features are discussed in detail in Ref. 124. Short crystal conception and exploitation is one of the main legacy of the UA9 Collaboration, in the last decade.

Appendix B. Theory of Channeled Particle Motion

Theoretical aspects of particle motion along a crystal are synthetically presented hereafter. More details are discussed in Refs. 5, 6, 125, 126.

B.1. *Particle motion in a straight crystal*

Classical treatment of particle motion in the planar potential well of a crystal is fully adequate at high energy.[6] Large numbers of correlated collisions with crystal plane atoms leave nearly unchanged the wave packet of the progressing particles. Moreover, the quantum levels are so numerous and densely spaced to consider negligible the probability of quantum tunneling through the potential well.

From the classical viewpoint, the interaction of a particle with one crystal atom is governed by the electric potential

$$V(r) = \frac{Z_1 Z_2 e^2}{r} \Phi\left(\frac{r}{a_{\mathrm{TF}}}\right), \quad \Phi\left(\frac{r}{a_{\mathrm{TF}}}\right) = \sum_{i=1}^{3} \alpha_1 e^{-\frac{\beta_i r}{a_{FT}}}, \tag{B.1}$$

where $Z_1 e$ is the charge of incident particles, Z_2 is the crystal atomic number, $\Phi\left(\frac{r}{a_{\rm TF}}\right)$ is the screening function due to electron charge distribution, $a_{\rm TF} = \left(\frac{9\pi^2}{128}\right)^{\frac{1}{3}} \cdot \frac{a_0}{\left(Z_1^{\frac{1}{2}}\right)+\left(Z_2^{\frac{1}{2}}\right)^{\frac{2}{3}}}$ is the screening length in the Thomas–Fermi approximation, $a_0 = \frac{\hbar^2}{m_e e^2} = 0.53\,\text{Å}$ is the Bohr radius, α_i, β_i are the Molière potential coefficients,[127] with $\bar{\alpha} = (0.1, 0.55, 0.35)$ and $\bar{\beta} = (6.0, 1.2, 0.3)$. For proton beams $a_{\rm TF} = 0.8853 a_0 Z_2^{-1/3}$.

A positive particle traveling almost parallel to a plane of atoms is reflected by many consecutive correlated hits. As the trajectory is inclined more than a critical angle θ_c, the hits become uncorrelated and a single atomic collision may rapidly deflect the particle away from the plane. The potential of a single crystalline plane is

$$Y_1(x) = 2N d_p \int_0^\infty \int_0^\infty V\left(\sqrt{x^2+y^2+s^2}\right) dy\, dz\,, \tag{B.2}$$

where x and y are the transverse coordinates, s the longitudinal one, d_p is the inter-atomic distance and N is the average atom density. The continuous planar potential $Y(\bar{x})$, which governs, for $\theta < \theta_c$, the three-dimensional (3D) trajectory $\bar{x}(t)$, is periodic in the transverse direction and results from the combination of the static field of each plane $Y_1(x)$:

$$Y(x) = \sum_{n=-\infty}^{\infty} Y_1(x - n d_p)\,, \tag{B.3}$$

where we assume $\bar{x} = (x, y, s)$. When the potential expansion in Ref. 128 is applied, one has

$$Y(x) = 2\pi Z_1 Z_2 e^2 N\, d_p \sum_{i=1}^{3} \frac{\alpha_i}{\kappa_i} \frac{\cosh\left[\kappa_i (x-l)\right]}{\sinh\left(\kappa_i l\right)}\,, \tag{B.4}$$

where $l = d_p/2$ and $\kappa_i = \beta_i / a_{\rm TF}$.

Figure B.1 shows the (110) planar potential in a silicon crystal, resulting from the combined effect of the static potential (B.4), averaged over the thermal vibrations at room temperature 20°C, where $u_1 = 0.075\,\text{Å}$ is the 1D vibration RMS-amplitude computed using the Debye theory. The coordinate x origin is the channel center, l is the channel half-width, $x_c = l - r_c$ is the maximal oscillation amplitude for stable channeling of particles, $r_c = 2.5 \cdot u_1$ is the critical approach to the channel walls and for silicon (110) crystals $U_{\max} = Y(l) = 22.7$ eV, $Y(x_c) = 14$ eV.

For a relativistic particle, horizontal motion in the potential well is governed by

$$\frac{dp_x}{dt} = -\frac{dY(x)}{dx}\,, \tag{B.5}$$

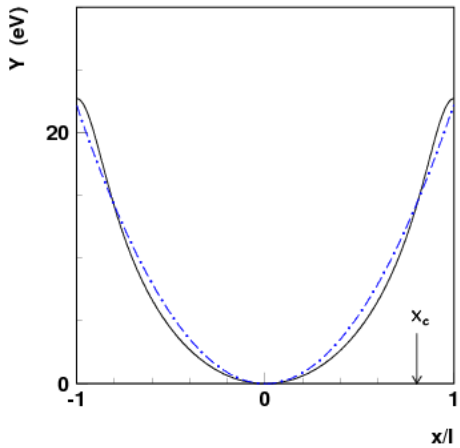

Fig. B.1. (Color online) Averaged potential of the (110) planar channel of a silicon crystal at room temperature in the Molière approximation for the atomic potential. The dotted-dashed line is the parabolic approximation for the potential. The coordinate x origin is the channel center, l is the channel half-width, $x_c = l - r_c$ is the maximal oscillation amplitude for stable channeling of particles, $r_c = 2.5 \cdot u_1$ is the critical approach to the channel walls. $U_{\max} = Y(l) = 22.7$ eV, $Y(x_c) = 14$ eV.

while vertical motion is free. Because of the low value of the transverse velocity, Eq. (B.5) reduces to

$$m\gamma\ddot{x} = -Y'(x)\,. \tag{B.6}$$

The transverse energy E_x is an integral of motion

$$E_x = \frac{m\gamma}{2}\dot{x}^2 + Y(x) = E^*\theta_x^2 + Y(x) = \text{const}\,, \tag{B.7}$$

where $\dot{x} = v\theta_x$, θ_x is the angle of the particle momentum with the crystal plane, $E^* = pv/2$, p and v are the particle momentum and velocity. $U_{\max} = Y(l)$ is the depth of the planar potential well. If $E_x < U_{\max}$, the transverse motion is bounded. The particle, trapped in channeling states, oscillates between two adjacent planes. For $E_x > U_{\max}$ the transverse motion is unbounded and the particle undergoes a so-called above barrier or quasi-channeled trajectory. The critical value θ_c of the incident angle θ_{x0}, for which $E_x = U_{\max}$, discriminates bounded and unbounded motion:

$$\hat{\theta}_{x0} = \theta_c = \sqrt{\frac{2U_{\max}}{pv}}\,. \tag{B.8}$$

Inside the critical distance r_c, the parabola approximating the potential well (blue curve in Fig. B.1) becomes

$$U(x) = U_{0s}\left(\frac{x}{x_c}\right)^2, \tag{B.9}$$

where $U_{0s} = Y(x_c)$ is the critical transverse energy for stable channeling. The harmonic solution of (B.6) becomes

$$x(s) = x_c\sqrt{\frac{E_x}{Y(x_c)}}\sin\left(\frac{2\pi s}{\lambda}+\phi_0\right), \tag{B.10}$$

$$\theta(s) = \sqrt{\frac{E_x}{E^*}}\cos\left(\frac{2\pi s}{\lambda}+\phi_0\right), \quad \lambda = 2\pi x_c\sqrt{\frac{E^*}{Y(x_c)}}. \tag{B.11}$$

As the particle progresses into the crystal, incoherent scattering by nuclei and electrons change the transverse energy. Dechanneling occurs as $\theta_x > \theta_c$. Single scattering at angles larger than θ_c is very unlikely. Cumulative effect of multiple scattering on electrons and nuclei is the main reason for dechanneling. A Fokker–Planck equation describes the evolution of the channeled particle density $f(E_x, s)$, along s[5,126]

$$\frac{\partial f}{\partial s} = -\frac{\partial}{\partial E_x}(Af) + \frac{\partial^2}{\partial E_x^2}(Bf), \tag{B.12}$$

where A and B are the friction and the diffusion coefficients, respectively, averaged over the electron and nuclear scattering cross-section, taking into account the equilibrium distribution of channeled particles averaged over one oscillation period along s. The averaged values of A and B are

$$A = \left\langle E\overline{\eta_s^2}\right\rangle, \tag{B.13}$$

$$B = \left\langle 2(E_x - U)E_2\overline{\eta_s^2}\right\rangle + \left\langle \frac{1}{2}E^2\overline{\eta_s^4}\right\rangle, \tag{B.14}$$

where $\eta = \theta\cos\varphi$ is the projection along x of the scattering angle θ, η_s means averaging η along s. By neglecting the second term of B and by assuming oscillation frequencies independent of oscillation amplitude, Eq. (B.12) becomes the diffusion equation

$$\frac{\partial f}{\partial z} = \frac{\partial}{\partial E_x}\left(B\frac{\partial f}{\partial E_x}\right) = A\frac{\partial x}{\partial E_x} + B\frac{\partial^2 f}{\partial E_x^2}, \tag{B.15}$$

with $A = \frac{\partial B}{\partial E_x}$. The first addendum of Eq. (B.15) leads to the monotonic growth of the E_x for large oscillation amplitudes. The second addendum describes the diffusion, important for the small oscillation amplitudes. Equation (B.15) was solved in Ref. 129, by assuming $B(E_x) = B_0E_x^m$, where m is a numerical exponent, with boundary and initial conditions

$$f(E_{xc}, s) = 0, \tag{B.16}$$

$$f(E_x, 0) = F_0(E_x), \tag{B.17}$$

where E_{xc} is the critical transverse energy and $F_0(E_x)$ is the initial distribution of the channeled particles. The boundary condition (B.16) excludes exchange between

stable and unstable fractions of the beam in the solution of (B.17), an assumption better fulfilled if the crystal is bent. According to Ref. 129, the solution of Eq. (B.15) is

$$F_{\rm ch}(s) = \sum_{n=1}^{\infty} q_n \exp\left(-\frac{s}{\lambda_n}\right). \tag{B.18}$$

Considering the valence electron density in the channel of semiconductors, such as silicon and germanium, as rather uniform up to x_c, that is $\rho_v = NZ_v$, where Z_v is the number of valence electrons per nucleus, we can assume $m = 1$ and $B(E_x) = B_0 E_x$. Since $\lambda_n \sim 1/\mu_n^2$, where μ_n are the zeros of the Bessel function J_0 for $m = 1$, the channeled fraction $F_{\rm ch}(s)$ is approximately determined by the first term of (B.14) and falls off exponentially. The experimental studies[30] also indicate exponential decrease of the channeled fraction with the penetration depth. The dechanneling length can be estimated as

$$S_{\rm dec}^0 \approx \lambda_1 = \frac{4E_{xc}}{\mu_{0,1}^2 A}, \quad A = E^* \left\langle \frac{\overline{\Delta\theta_x^2}}{\Delta s} \right\rangle, \tag{B.19}$$

where A, the friction coefficient, gives the average increase of the transverse energy per unit length along s.

The critical distance $r_c = l - x_c$ from the plane of atoms limits the region of applicability of the continuous approximation and determines the instability region with large nuclear density, the "nuclear corridor," where particles undergo strong multiple scattering by nuclei and can fast dechannel. The value of r_c is proportional to the thermal vibration amplitude u_1. For silicon crystal, a good estimate is $r_c = 2.5u_1$.

The dechanneling process consists of two stages, a long one induced by collision with the crystal electrons and a fast one due to collisions with the crystal nuclei. The latter applies to particles with $x_m > x_c$, where x_m is the peak oscillation amplitude in the channels. The critical transverse energy $E_{xc} = U(x_c)$ separates two stages of dechanneling.

The mean squared deflection of particles per unit path-length due to multiple scattering on nuclei can be calculated in the Ohtsuki–Kitagawa approximation[130]

$$\begin{aligned} \left(\frac{\overline{\Delta\theta^2}}{\Delta s}\right)_n(x) &= \left(\frac{\overline{\Delta\theta^2}}{\Delta s}\right)_R P_n(x), \\ \left(\frac{\overline{\Delta\theta^2}}{\Delta s}\right)_R &= \frac{1}{L_r}\left(\frac{E_s}{pv}\right)^2, \\ P_n(x) &= \frac{d_p}{(2\pi u_1^2)^{1/2}} \exp\left(-\frac{x^2}{2u_1^2}\right), \end{aligned} \tag{B.20}$$

where $\left(\frac{\overline{\Delta\theta^2}}{\Delta s}\right)_R$ is the corresponding value for an amorphous material, $P_n(x)$ is the transverse distribution of the crystal plane atoms due to thermal vibrations, $E_s = 21$ MeV, and L_r is the radiation length.

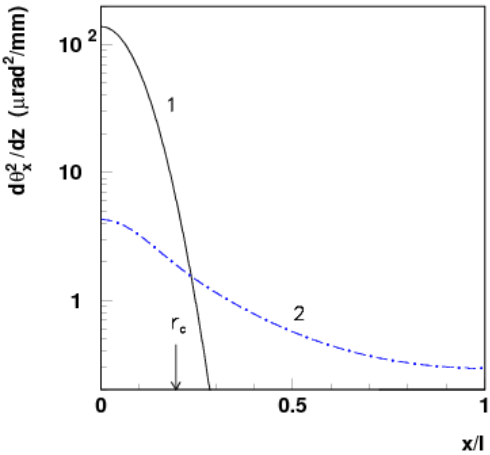

Fig. B.2. The mean squared deflection projection of 400 GeV/c protons per unit path length due to multiple scattering on nuclei (1) and electrons (2) in a silicon crystal as a function of the distance to the (110) channel wall. The x-axis origin corresponds to the position of a static atomic plane.

The mean squared deflection of particles per unit path-length due to multiple scattering on the crystal electrons can be calculated using the proportionality to the energy losses in close collisions[5]

$$\begin{aligned} \frac{\overline{\Delta\theta^2}}{\Delta s}_e(x) &= \frac{m_e}{p^2}\left(-\frac{dE}{ds}\right)\frac{\rho(x)}{NZ_2}\,, \\ -\frac{dE}{ds} &= \frac{4\pi Z_1^2 e^4}{m_e v^2} NZ_2\left[\ln\left(\frac{2m_e\gamma^2c^2\beta^2}{I}\right)-\beta^2\right], \end{aligned} \tag{B.21}$$

where $-(dE/ds)$ is the ionization energy losses per unit length, I is the ionization potential ($I = 165$ eV for Si) and $\rho(x)$ is the electron density into the channel, determined by the solution of the Poisson equation in presence of the planar potential of two neighboring planes. Detailed expression for $\rho(x)$ and corrective factors for (B.21) are discussed in Ref. 131. In close collisions with the electrons in the channel, the energy transfer is limited to $T_{\max} \simeq 2m_e c^2\beta^2\gamma^2$ by cinematic considerations. The expression (B.21) is computed by including all the allowed collisions, although the energy transfer for dechanneling $T(\theta_c)$ is smaller than $T_{\max}$. Motivations of this choice, discussed in Ref. 132, are related to the easier implementation of simulation code, without prejudice for result accuracy.

Figure B.2 shows the mean squared deflection projection of 400 GeV/c protons per unit length due to multiple scattering on the crystal nuclei and electrons as a function of the distance to the channel wall. In the latter plot the x-axis origin corresponds to the position of a static atomic plane. For $x < r_c$, the main contribution to the change of the particle transverse energy occurs from scattering on the atomic nuclei.

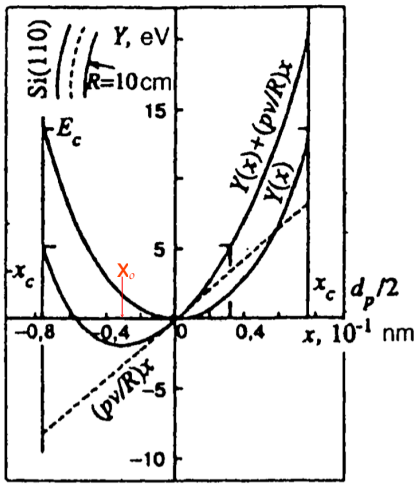

Fig. B.3. Effective potential of the (110) planar channel of a silicon crystal bent with $R_b = 10$ cm. $U_{\text{eff}} = Y(x) + \frac{pv}{R}x$ has a minimum at $x = x_0$.

B.2. *Particle motion in a bent crystal*

In a bent crystal of constant radius R, where $R_b(s) = R$, $\forall s \in (0, L)$, a centrifugal term is added to the potential well to explain the rotational motion of channeled particles around the center of curvature with azimuthal velocity v. The effective potential, shown in Fig. B.3, becomes

$$U_{\text{eff}}(x, F_c) = U(x) \pm F_c x + U_{\text{co}}(F_c)\,, \tag{B.22}$$

where $F_c = pv/R$ is the centrifugal force and $U_{\text{co}}(F_c)$ is a constant, such that $U(0) = 0$. The sign of the centrifugal term depends on the direction in which the transverse coordinate x is measured; it is minus in the direction of the bend radius. The particle trajectory is governed by the equation of motion:

$$\ddot{x}(t) = -\frac{1}{m\gamma}\frac{d}{dx}U_{\text{eff}}(x, F_c)\,. \tag{B.23}$$

The harmonic approximation provides useful analytical estimate of the particle kinematics as a function of E and R.[30] The effective harmonic potential, the equation of motion and the oscillatory solution are, respectively

$$\begin{gathered} U_{\text{eff}}(x, R) = U_{\text{os}}\left(\frac{x - x_0}{x_c}\right)^2, \quad x_0 = \frac{F_c}{2U_{\text{os}}}x_c^2\,, \\ x''(s) + \frac{1}{pv}U'(x) + \frac{1}{R} = 0\,, \quad x(s) = x_0 + x_c\sqrt{\frac{E_x}{Y(x_c)}}\sin\left(\frac{2\pi s}{\lambda} + \phi_0\right), \end{gathered} \tag{B.24}$$

where $x_0 = x_c\frac{R_c}{R}$ and $R_c = \frac{pv}{U'(x_c)}$. The abscissa of the U_{eff} minimum and that of the average trajectory are shifted to the outer side of the channel by a distance x_0. The particle confinement in the potential well of a bent crystal is less effective than

of a straight crystal. In particular, for $R = R_c$, $x_0 = x_c$ and the trajectory is no longer stable. The dependence of E_{xc} and θ_c on R and E is

$$\begin{aligned} E_{xc}(R) &= U_{\rm os}(1 - R_c/R)^2\,, \quad E_{xc}(E) = U_{\rm os}(1 - E/E_c)^2\,, \\ R_c(E) &= x_c\frac{E^*}{U_{\rm os}}\,, \qquad\qquad E_c^*(R) = U_{\rm os}\frac{R}{x_c}\,, \\ \theta_c(R) &= \theta_c \times (1 - R_c/R)\,, \quad \theta_c(E) = \theta_c \times (1 - E/E_c)\,, \end{aligned} \tag{B.25}$$

where the critical radius R_c for particles of energy E obeys to $x_0(R_c, E) = x_c$ and the critical energy E_c for crystals of radius R obeys to $x_0(R, E_c) = x_c$. For decreasing values of R, the decrease of θ_c and the simultaneous increase of x_0 contribute to reducing the range of oscillation amplitudes for stable motion and the probability of channeling. The reduction is very rapid for $R < 10R_c$. The channeling probability decreases with the increase of E, as well.

The approximate value of the dechanneling length is

$$\begin{aligned} S_{\rm dec}(R) &= S^0_{\rm dec}(1 - R_c/R)^2\,, \\ S_{\rm dec}(E) &= S^0_{\rm dec}(E)(1 - E/E_c)^2\,. \end{aligned} \tag{B.26}$$

From Eqs. (B.13) and (B.19), the dechanneling length in a straight crystal $S^0_{\rm dec}$ decreases with E. Therefore, according to (B.26), the dechanneling length in a bent crystal $S_{\rm dec}(E)$ should have a maximum at some energy value.[133] The beam deflection efficiency P_d can be estimated as

$$\begin{aligned} P_d(\theta_b, R) &= P_c(R)P_{\rm ch}(\theta_b, R)\,, \\ P_{\rm ch}(\theta_b, R) &= \exp\left[-\frac{\theta_b R}{S_{\rm dec}(R)}\right], \end{aligned} \tag{B.27}$$

where $P_c(R)$ is the capture probability of particles into the channeling regime, $P_{\rm ch}(\theta_b, R)$ is the probability to pass through the whole crystal in the channeling regime. There are optimal values of R and L that maximize the deflection yield at a given crystal bending angle θ_b.[133]

For parabolic potential and uniform angular distribution of the incident beam, the deflection efficiency is:[134]

$$P_d(\theta_b, \rho) = P_c^o(1 - \rho)^2 \exp\left(-\frac{\theta_b/\theta_D}{\rho(1 - \rho)^2}\right), \tag{B.28}$$

where $\rho = R_c/R$ and P_c^o is the capture probability in a straight crystal. The capture probability in a bent crystal $P_c(R)$ decreases in the same way as the dechanneling length. The optimal crystal bend is determined by the condition[134]

$$\frac{\theta_b}{\theta_D} = \frac{2\rho^2(1 - \rho)^2}{1 - 3\rho}\,, \quad \theta_D = \frac{S^0_{\rm dec}}{R_c}\,, \tag{B.29}$$

where θ_D is a deflection angle close to the maximum possible one. The optimal bend radius is always larger than $3R_c$ according to (B.29).

Volume capture is the process by which a particle, initially unbound, loses transverse energy to become bound in the channel. Such an effect, relying on transverse energy loss due to multiple scattering, is the opposite of dechanneling. In a bent crystal, volume capture and dechanneling are reversible processes that may happen with the same probability all along the crystal length.[135] This consideration suggests a way of evaluating the volume capture probability over a length $ds = R\theta_c$ along which a particle in quasi-channeling state becomes disoriented with respect to the crystal planes and loses the possibility of being captured in channeling state. One find:

$$P_{\rm dec} = P_{\rm VC} = \frac{ds}{S_{\rm dec}(R)} \Rightarrow P_{\rm VC} \simeq \frac{R\theta_c}{S_{\rm dec}(R)} \sim \frac{R}{E^{3/2}}\,. \tag{B.30}$$

Equation (B.30) is valid for R not too large and for particle capture into deep levels in the channel potential, i.e. for $R\theta_c \ll S_{\rm dec}$. More details can be found in Ref. 61.

Polar coordinates (r, φ) are used to describe the particle motion in a bent crystal. The equations of motion become:[92,136]

$$\begin{aligned} \frac{d}{dt}(m\gamma\dot{r}) &= m\gamma r\dot{\varphi}^2 - \frac{dU}{dr}\,, \\ \frac{d}{dt}(m\gamma r^2\dot{\varphi}) &= 0\,, \\ \frac{d}{dt}(m\gamma c^2) &= -\dot{r}^2\frac{dU}{dr}\,. \end{aligned} \tag{B.31}$$

The total energy W and angular momentum M are integrals of motion

$$W = m\gamma c^2 + U(r)\,, \tag{B.32}$$

$$M = m\gamma r^2\dot{\varphi}\,. \tag{B.33}$$

The trajectory equation in polar coordinates is

$$\varphi(r) = \pm M \int \frac{r^{-2}dr}{\left[\frac{(W-U(r))^2}{c^2} - \frac{M^2}{r^2} - m^2c^2\right]^{\frac{1}{2}}} + \varphi_0\,, \tag{B.34}$$

where φ_0 is a constant. For the initial conditions r_0 and $v_0 = \beta_0 c$ at the crystal entry point, the integrals of motion become $W = E_0 + U(r_0)$, $M = r_0 E_0 \beta_0 c^{-1}\cos\theta_{\rm in}$, where $E_0 = m\gamma c^2$ and $\theta_{\rm in}$ is the horizontal projection of the angle between the particle momentum and the atomic planes. The radial energy $E_r = E^*\sin^2\theta_{\rm in} + U_{\rm eff}(r, R)$ is an integral of motion for high-energy particles with $E_0 \gg U(r)$, traveling along a crystal of small radial size $\Delta r \ll R$, inside the effective potential well $U_{\rm eff}(r, R) = U(r) - \frac{2E^*}{R}r$. Using the centrifugal force $F_c = \frac{2E^*}{R}$ to characterize the crystal curvature and measuring the angles in units of θ_c, the trajectory equation

can be written in a form independent of the particle energy

$$\bar{\varphi}(r, F_c) = \frac{F_c}{2U_0^{\frac{1}{2}}} \int_{r_0}^{r} \frac{dr}{\left[U_0\bar{\theta}_{\rm in}^2 + U_{\rm eff}(r_0, F_c) - U_{\rm eff}(r, F_c)\right]^{\frac{1}{2}}}\,, \tag{B.35}$$

where $\bar{\varphi} = \varphi/\theta_c$, $\bar{\theta}_{\rm in} = \theta_{\rm in}/\theta_c$. More details are given in Ref. 136.

Volume reflection is the process by which quasi-channeled particles entering a crystal with $\theta_{\rm in} > \theta_c$, are deflected by $\Delta\theta \simeq -1.6\theta_c(R)$ in the outer bend side, with a narrow angular spread. Quasi-channeled particles with $\theta_{\rm in} = 0$, instead, undergo a deflection angle $\Delta\theta \simeq -0.8\theta_c(R)$. Volume reflection, that holds for bent crystals with $R \gg R_c$, was discovered by investigating numerically the equation on motion (B.35).[136] Quasi-channeled particles cross several crystal planes and undergo strong multiple scattering on the way to the turn-over point. This induces a considerable broadening of the angular dispersion at the entry of the volume reflection region and the capture in channeling regime of a small beam fraction. The size of the volume reflection region is the same as the one of volume capture, $S_{\rm VR} \sim R\theta_c \sim E^{1/2}$. The beam broadening over a length $S_{\rm VR}$ can be estimated assuming that multiple scattering is the same as in an amorphous case

$$\overline{\Delta\theta^2}_{\rm VR} = S_{\rm VR} \cdot \frac{\overline{\Delta\theta^2}}{\Delta s}_{R} \sim E^{-\frac{3}{2}}\,, \quad \frac{\langle\overline{\Delta\theta^2}_{\rm VR}\rangle^{\frac{1}{2}}}{\theta_c} \sim E^{-\frac{1}{4}}\,. \tag{B.36}$$

The relative angular spread of the particles volume reflected in the crystal decreases with increasing particle energy as $E^{-1/4}$. Therefore, volume reflection should be better observed for high-energy particles in short crystals.

B.3. *Particle tracking in a bent crystal*[126]

Binary collision model, conceived to track particle trajectory in a crystal resulting from the interactions with each atom, is inapplicable, even to short crystals of millimetric length, because of the too large computing resources required.

Computational tracking is usually performed by segmenting the particle trajectory and by evaluating the transition of the phase space probability density through each crystal segment.

In channeling orientation, the numerical solution of the equation of motion (B.24) in Cartesian coordinates, or (B.31) in polar coordinates provides an approximate particle trajectory. The longitudinal velocity v is assumed constant. The integration time step Δt is small enough that $\Delta s = v\Delta t \ll \lambda$, the energy loss can be neglected and the transverse energy E_x is conserved. The change of transverse velocity due to multiple scattering is applied in steps of duration $\Delta t_{\rm ms}$, where $\Delta t \leq \Delta t_{\rm ms}$. The corresponding distance step $\Delta s_{\rm ms} = v\Delta t_{\rm ms}$, is limited by lower and upper bounds fulfilling the requirements that the multiple scattering formula is still valid and that the particle energy loss is negligible, respectively. The effect of multiple scattering is decomposed into a coherent part, in which the average change of momentum is induced by the continuous planar potential well and an incoherent part in which momentum changes because of the hits on electrons and on

nuclei, taking into account the continuous thermal vibrations of the crystal planes. Oscillatory motion in the potential well brings the particle through a region with highly nonuniform density of electrons and nuclei, where very strong dependence of multiple scattering probability on the transverse position x occurs. The condition $\Delta s_{\rm ms} \ll \lambda$ allows to correctly take this effect into account. Multiple scattering on nuclei and on electrons is described by Eqs. (B.20) and (B.21), respectively. Accordingly to Ref. 5, the stopping power on traveling particle is proportional to the local electron density $\rho_e(x)$:

$$\mu(x) = \mu_{\rm am} \left[(1-\alpha) + \frac{\alpha \rho_e(x)}{N Z_2} \right], \tag{B.37}$$

where $\alpha \simeq 1/2$ is a separation constant, NZ_2 is the average electron density far from channeling orientation and $\mu_{\rm am}$ is the stopping power in amorphous matter. For particles moving close to the channel axis, the stopping power is $\mu(0) \simeq 0.5\mu_{\rm am}$ and the ionization loss is neglected. For over-barrier particles, energy loss is fully accounted for (B.37).

Multiple scattering in non-channeled orientation is evaluated as in amorphous matter. Over-barrier particles are identified by a threshold in the transverse energy $E_x > E_{xr}$. For protons crossing (110) planes of silicon crystal, the threshold $E_{xr} =$ 400 eV is chosen. The integration step of over-barrier trajectories is increased, with the constraint that it is shortened again if $E_x < E_{xr}$.

In each trajectory segment of length $\Delta z_{\rm ms}$, in addition to the multiple scattering, the probability of inelastic nuclear interaction (INI) is also computed using

$$P_{\rm INI} = 1 - e^{-\frac{\Delta z_{\rm ms}}{L_{\rm INI}}} \simeq \frac{\Delta z_{\rm ms}}{L_{\rm INI}}, \quad L_{\rm INI} = \frac{L_n}{\langle P_n \rangle}, \tag{B.38}$$

where $L_{\rm INI}$ is the mean free path between inelastic nuclear interactions for the average nuclear density $N \times \langle P_n \rangle$ per crystal plane and $L_n = 45$ cm is the mean free path between interactions in amorphous silicon. The fraction of particles having nuclear interactions along their paths is considered lost and their trajectory is no longer computed.

At each integration step, the transverse angle θ with the crystal planes is inspected to evaluate the status of the particle and to identify the formula to compute the transition of phase space probability density, in the successive step. Moreover, the code takes into account the crystal geometry to evaluate special interaction features induced by possible entrance/escape of particles through the crystal lateral surface, crossing of amorphous surface layer and crystal plane misalignment with the crystal faces due to miscut angle. By iterating the algorithm over the entire set of crystal segments, the final phase space probability density for the fraction of particles channeled, dechanneled, volume reflected, volume captured, deflected by a single very large nuclear scattering event, traveling over barrier in amorphous regime, lost by inelastic nuclear interactions and having lost energy in a diffractive scattering, during crystal traversal, is computed.

Appendix C. List of Abbreviations

LHC	Large Hadron Collider
HL–LHC	High Luminosity – Large Hadron Collider
B1	Beam 1
B2	Beam 2
SM	Standard Model
CERN	Conseil Européen pour la Recherche Nucléaire
ISR	Intersecting Storage Ring
SPS	Super Proton Synchrotron
SPPbarS	Super Proton anti-Proton Synchrotron
LEP	Large Electron Positron collider
RHIC	Relativistic Heavy Ion Collider
BNL	Brookhaven National Laboratory
FNAL	Fermi National Accelerator Laboratory
RF	Radio Frequency
FODO	Focus (O) drift Defocus (O) drift
MCS	Multiple Coulomb Scattering
IR	Interaction Region
IP	Interaction Point
DS	Dispersion Suppressor
LM	Loss Map
BLM	Beam Loss Monitor
LSS	Long Straight Section
TCP	Target Collimator Primary
TCSG	Target Collimator Secondary Graphite
TCLA	Target Collimator auxiLiary Absorber
TCT	Target Collimator Tertiary
CFC	Carbon Fiber Composite
TCPC	Target Collimator Primary Crystal
INI	Inelastic Nuclear Interaction
CH	planar CHanneling
AC	Axial Channeling
DC	DeChanneling
VR	Volume Reflection
VC	Volume Capture
BCC	Body-Centered Cubic
FCC	Face-Centered Cubic
ST	STrip crystals
QM	Quasi-Mosaic crystals
Run #	LHC Run Number
EYETS	Extended Year-End Technical Stop
VSC	Vacuum Surface and Coating
BIS	Beam Interlock System
UA9	Underground Area 9 Experiment
NA	SPS North Area
ADT	Acceleration Transverse Damper
(F)BCT	(Fast) Beam Current Transformer
MD	Machine Development
Q#	LHC Quadrupole # cell
Cfg#	LHC Configuration
CpFM	Cherenkov-radiator quartz bar

Appendix D. List of Symbols

p, $\vec{p}$	particle momentum	eV c_0^{-1}
v, $\vec{v}$	particle velocity	m s^{-1}
s, $\vec{s}$	particle longitudinal coordinate	m
(x, y)	particle transverse coordinates	m
$(x', y') = (dx/ds, dy/ds)$	derivative of the transverse coordinates	rad
$(\dot{x}, \dot{y}) = v \cdot (x', y')$	transverse velocities	m s^{-1}
$(\ddot{x}, \ddot{y})$	transverse accelerations	m s^{-2}
B, $\vec{B}$	magnetic field	T
$\alpha(s)$, $\beta(s)$, $\gamma(s)$	Twiss functions ($\alpha = -1/2\beta', \gamma = (1+\alpha^2)/\beta$)	rad, m, m^{-1}
γ	Lorentz factor	—
$\Phi(s)$, $\Delta\Phi(s)$	phase advance	rad
$D(s)$, $D_x(s)$	dispersion function	m
$D'(s)$, $D'_x(s)$	derivative of the dispersion function	—
ε	beam emittance	m rad
$\sigma(s)$	beam size (σ_x, σ_y horizontal and vertical)	m
$\sigma'(s)$	beam divergence (σ'_x, σ'_y horizontal and vertical)	rad
η_c	collimation cleaning inefficiency	
Q	tune (Q_x, Q_y horizontal and vertical)	—
p_0	momentum of a synchronous particle in a circular accelerator	eV $c_0{}^{-1}$
E_0	energy of a synchronous particle in a circular accelerator	eV
$\delta = p/p_0 - 1$	relative momentum spread of a nonsynchronous particle	—
ℓ	longitudinal deviation of a particle in a bunch	m
(ℓ, δ)	coordinates of the longitudinal motion	m, —
δ_0	initial relative momentum spread of a nonsynchronous particle	—
$x_\delta = \delta \cdot D_x$	orbit deviation of a nonsynchronous particle in a dispersive region	m
C_0	orbit length in the accelerator circumference	m
V_{RF}	amplitude of the accelerating voltage of a radio-frequency cavity	m
h	harmonic number of the voltage of a radio-frequency cavity	—
σ_ℓ	spread of the longitudinal deviation of the particles in a bunch	m
σ_δ	spread of the relative momentum of the particles in a bunch	—
Q_s	synchrotron motion tune	—
ω_{rev}	angular revolution frequency	Hz
T_{rev}	revolution period	s
T_s	synchrotron period	s
L	crystal length in the beam direction	m
R_b, R	crystal bending radius	m

θ_b	crystal bending angle	rad
θ_c	critical angle for a straight crystal	rad
$\theta_c(R)$	critical angle for a bent crystal of radius R	rad
R_c	critical radius	m
d_p	crystalline inter-planar distance	Å
l	crystalline inter-planar half-distance	Å
$r = \sqrt{x^2 + y^2 + s^2}$	distance from a nucleus	m
Z	atomic number	—
p/Z	ion momentum per unit charge	eV $c_0{}^{-1}$
$a_{\rm TF}$	screening length in the Thomas–Fermi approximation	m
a_0	Bohr radius	m
$\Phi(r/a_{\rm TF})$	screening function due to electron charge distribution	m
$\vec{\alpha}$, $\vec{\beta}$, α_i, β_i	Moliere potential coefficients	—
u_1	1D vibration RMS-amplitude of the nuclei in a crystal	Å
r_c	critical approach distance from the channel walls	Å
$x_c = l - r_c$	maximal oscillation amplitude for stable channeling	Å
$V(r)$	electric potential of a nucleus	eV
$Y_1(x)$	electric potential of the nuclei in a single crystalline plane	eV
$Y(x)$	electric potential of all the crystalline planes in a crystal	eV
$U_{\max} = Y(l)$	crystalline inter-planar maximum potential	eV
$U_{0s} = Y(x_c)$	critical transverse potential for stable channeling	eV
$U(x) = U_{0s}(x/x_c)^2$	potential well in the harmonic approximation	eV
E	beam energy	eV
$E_x = E^*\theta_x^2 + Y(x)$	transverse energy (constant of the motion in channeling modes)	eV
$E^* = pv/2$		eV
E_{xc}	critical energy for channeling	eV
$d_{0,x}$, $d_{0,y}$, $\vec{d_0}$	entry point of the particle into the crystal	meter
b	particle impact parameter with a crystal (distance from the crystal face)	m
λ	wavelength of the channeling oscillation	m
$F_c = pv/R$	centrifugal force in a bent crystal	kg m s^{-2}
$U_{\rm eff}(x, R)$	effective harmonic potential in a bent crystal	eV
$x_0 = x_c \cdot R_c/R$	oscillation center in a bent crystal ($U_{\rm eff}(x_0)$ is a minimum)	m
$E_{xc}(R)$	critical energy for channeling in a bent crystal	eV
$P_{\rm CH}$	probability of channeling	—
$P_{\rm VR}$	probability of volume reflection	—
$P_{\rm VC}$	probability of volume capture	—
$P_{\rm dec}$	probability of dechanneling	—
$P_{\rm in}$	probability of nuclear inelastic interactions	—
$P_d(\theta_b, R)$	probability of deflection in a bent crystal	—
$S^n_{\rm dec}$	dechanneling length due to interactions with nuclei	m
$S^e_{\rm dec}$	dechanneling length due to interactions with electrons	m
$S^0_{\rm dec}$	dechanneling length in a straight crystal due to interactions with electrons and nuclei	m
$S_{\rm dec}(R)$	dechanneling length in a bent crystal due to interactions with electrons and nuclei	m
$S_{\rm in}$	nuclear inelastic interaction length	m

L_r	radiation length	m
dE/dx	beam energy loss per unit length of material	eV m^{-1}
$\dot{N}_{\rm AM}$	loss rate in amorphous orientation	particles/s
$\dot{N}_{\rm CH}$	loss rate in channeling states	particles/s
$R_{\rm loss} = \dot{N}_{\rm AM}/\dot{N}_{\rm CH}$	loss reduction factor from channeling to amorphous orientation	—
$X_{\rm cr}$	crystal distance from the center line	m
$X_{\rm asb}$	absorber distance from the center line	m
$\sigma_{\rm tot}$	total cross section	cm^2 (b)
$\sigma_{\rm in}$	nuclear inelastric cross section	cm^2 (b)
$\theta_{\rm VR}$	Volume Reflection angle	rad
$\Delta\theta_{\rm VR}$	spread of the Volume Reflection angle	rad
$\theta_{\rm in}$	angle of the incoming particle with crystal planes	rad
$\theta_{x,{\rm in}}$, $\theta_{y,{\rm in}}$	horizontal and vertical angles of the incoming particle with crystal planes	rad
$k = \theta_{\rm in}/\theta_c$	ratio of the initial to the critical angle	—
$\theta_{\rm out}$	angle of the outgoing particle with crystal planes	rad
$\Delta\theta = \theta_{\rm in} - \theta_{\rm out}$	particle deflection angle	rad
$\Delta\theta_x$, $\Delta\theta_y$	horizontal and vertical deflection angle	rad
$\delta\theta_b$	spread of the channeled particle deflection angle	rad
$\eta_{\rm ch}$	channeling efficiency	m
$\eta_{\rm VR}$	Volume Reflection efficiency	m
$\theta_{\rm ms}$	RMS deflection due to CMS	rad
θ_m	crystal miscut angle	rad

References

1. E. Tsyganov, Some aspects of the mechanism of a charge particle penetration through a monocrystal, Fermilab TM-682, Batavia, Illinois 60520, USA (1976), https://lss.fnal.gov/archive/test-tm/0000/fermilab-tm-0682.pdf.
2. W. Scandale, *Mod. Phys. Lett. A* **27**, 1230007 (2012).
3. W. Scandale *et al.*, *Nucl. Instrum. Methods Phys. Res. B* **268**, 2655 (2010).
4. W. Scandale *et al.*, *Eur. Phys. J. C* **80**, 27 (2020).
5. J. Lindhard, *Kongel. Dan. Vidensk. Selsk., Mat.-Fys. Medd.* **34**(14) (1965).
6. D. Gemmell, *Rev. Mod. Phys.* **46**, 129 (1974).
7. V. Biryukov, Y. Chesnokov and V. Kotov, *Crystal Channeling and Its Application at High Energy Accelerators* (Springer, 1996).
8. D. Trbojevic *et al.*, A study of RHIC crystal collimation, in *6th European Particle Accelerator Conference* (*EPAC 98*) (1998), pp. 2146–2148, arXiv:hep-ex/0111021.
9. R. Fliller *et al.*, *Nucl. Instrum. Methods Phys. Res. B* **234**, 47 (2005).
10. R. P. Fliller *et al.*, *Phys. Rev. ST Accel. Beams* **9**, 013501 (2006).
11. N. Mokhov *et al.*, *Int. J. Mod. Phys. A* **25**, 98 (2010).
12. V. Zvoda *et al.*, Advanced bent crystal collimation studies at the Tevatron (T-980), FERMILAB-CONF-11-127-APC (2012), arXiv:1203.1648.
13. D. Still *et al.*, *Conf. Proc.* **C1205201**, 559 (2012).
14. N. Mokhov and D. Still, T980 crystal collimation (2011), https://fdocuments.in/document/t980-crystal-collimation.html.
15. H. Akbari *et al.*, *Phys. Lett. B* **313**, 491 (1993).
16. X. Altuna *et al.*, *Phys. Lett. B* **357**, 671 (1995).

17. A. A. Aseev *et al.*, First observation of luminosity driven extraction using channeling with a bent crystal, Tech. Rep. FERMILAB-PUB-97-300-E, FERMILAB, Batavia, IL 60520, USA (1997), http://cds.cern.ch/record/421594.
18. C. Thornton Murphy, Crystal extraction of beam from high energy hadron accelerators, FERMILAB-CONF-99-005-E (1998), http://cds.cern.ch/record/386236.
19. R. A. Carrigan Jr. *et al.*, *Phys. Rev. ST Accel. Beams* **5**, 043501 (2002).
20. V. Biryukov *et al.*, *Rev. Sci. Instrum.* **73**, 3170 (2002).
21. A. Afonin *et al.*, *J. Exp. Theor. Phys. Lett.* **67**, 781 (1998).
22. A. G. Afonin *et al.*, *Phys. Rev. Lett.* **87**, 94802 (2001), http://cds.cern.ch/record/977715.
23. W. Scandale, *Int. J. Mod. Phys. A* **25**, 70 (2010).
24. W. Scandale *et al.*, *Phys. Lett. B* **692**, 78 (2010).
25. W. Scandale *et al.*, *Phys. Lett. B* **703**, 547 (2011).
26. W. Scandale *et al.*, *Phys. Lett. B* **714**, 231 (2012).
27. W. Scandale *et al.*, *Phys. Lett. B* **726**, 182 (2013).
28. W. Scandale *et al.*, *Phys. Lett. B* **748**, 451 (2015).
29. W. Scandale *et al.*, *Phys. Lett. B* **758**, 129 (2016).
30. W. Scandale and A. M. Taratin, *Phys. Rep.* **815**, 1 (2019), http://cds.cern.ch/record/2689810.
31. W. Scandale *et al.*, *Rev. Sci. Instrum.* **79**, 023303 (2008).
32. S. Hasan, Experimental techniques for deflection and radiation studies with bent crystals, presented 10 May 2011, https://cds.cern.ch/record/1353904.
33. M. Pesaresi *et al.*, *J. Instrum.* **6**, P04006 (2011).
34. R. Rossi *et al.*, *Nucl. Instrum. Methods Phys. Res. B* **355**, 369 (2015).
35. M. Garattini, Overview of the crystal performance at the SPS-H8 (2017), https://indico.cern.ch/event/752062/contributions/3114845/attachments/1737304/2810539/Garattini_CrystalSPS_H8.pdf.
36. R. Rossi, Misure di fenomeni di interazione coerente di protoni a 400 GeV con cristalli curvi per l'LHC (in Italian), Master thesis, Università degli Studi di Roma 1 (2014), https://cds.cern.ch/record/1973372.
37. W. Scandale *et al.*, *Phys. Lett. B* **680**, 129 (2009).
38. W. Scandale *et al.*, *J. Instrum.* **6**, T10002 (2011).
39. W. Scandale *et al.*, *Nucl. Instrum. Methods Phys. Res. A* **975**, 164175 (2020).
40. W. Scandale *et al.*, *Nucl. Instrum. Methods Phys. Res. A* **1015**, 165747 (2021), https://www.sciencedirect.com/science/article/pii/S0168900221007324.
41. G. Arduini *et al.*, *J. Instrum.* **11**, C12081 (2016), http://cds.cern.ch/record/2255815.
42. G. Valentino *et al.*, *Phys. Rev. Accel. Beams* **20**, 081002 (2017).
43. Medipix Project website: https://medipix.web.cern.ch/collaboration/medipix2-collaboration.
44. M. Esposito *et al.*, *Nucl. Instrum. Methods Phys. Res. A* **652**, 458 (2011).
45. L. Burmistrov *et al.*, *Nucl. Instrum. Methods Phys. Res. A* **787**, 173 (2015).
46. F. M. Addesa *et al.*, The SE-CpFM detector for the crystal-assisted extraction at CERN-SPS, in *Proc. 6th Int. Beam Instrumentation Conf.* (*IBIC '17*), Grand Rapids, MI, USA, August 2017 (2017), pp. 419–422.
47. F. M. Addesa, In-vacuum Cherenkov light detectors for crystal-assisted beam manipulations, Ph.D. thesis, Università degli Studi di Roma 1 (2018), https://cds.cern.ch/record/2661725.
48. F. M. Addesa *et al.*, *Nucl. Instrum. Methods Phys. Res. A* **946**, 162513 (2019).

49. S. Petrucci, Advanced crystal collimation studies at the SPS, Master thesis, Università degli Studi di Roma 1 (2017), http://www.infn.it/thesis/thesis_dettaglio.php?tid=11933.
50. C. Hadjidakis *et al.*, A fixed-target programme at the LHC: Physics case and projected performances for heavy-ion, hadron, spin and astroparticle studies, http://cds.cern.ch/record/2628419.
51. L. Burmistrov *et al.*, Measurement of short living baryon magnetic moment using bent crystals at SPS and LHC, CERN-SPSC-2016-030/SPSC-EOI-012 (2016), https://cds.cern.ch/record/2194564/files/SPSC-EOI-012.pdf.
52. V. Previtali, Performance evaluation of a crystal-enhanced collimation system for the LHC, Ph.D. thesis, EPFL Thesis, N. 4794, CERN-THESIS-2010-133 (2010), p. 219, http://infoscience.epfl.ch/record/149810.
53. J. M. Cesaratto *et al.*, SPS wideband transverse feedback kicker: Design Report, Tech. Rep., CERN-ACC-NOTE-2013-0047 (2013), http://cds.cern.ch/record/1639553.
54. S. G. Peggs and V. Previtali, *Phys. Rev. ST Accel. Beams* **12**, 114001 (2009).
55. D. Mirarchi, Collimazione di fasci di adroni con cristalli piegati in UA9, Master's thesis (in Italian) (2011), http://cds.cern.ch/record/1392679.
56. W. Scandale and A. Taratin, Simulation of CRYSTAL, the bent crystal based collimation experiment in the SPS, Tech. Rep. CERN-AT-2008-021, CERN, Geneva, support of the European Community Research Infrastructure Activity under the FP6 "Structuring the European Research Area" programme (CARE, contract number RII3-CT-2003-506395) Collaboration (2008), http://cds.cern.ch/record/1122960.
57. V. Uzhinsky and A. Galoyan, *Phys. Lett. B* **721**, 68 (2013).
58. A. Taratin and W. Scandale, *Nucl. Instrum. Methods Phys. Res. B* **313**, 26 (2013), http://www.sciencedirect.com/science/article/pii/S0168583X13008148.
59. D. Mirarchi *et al.*, *Nucl. Instrum. Methods Phys. Res. B* **355**, 378 (2015).
60. Y. A. Chesnokov *et al.*, The results on experimental investigation of possibility to use bent crystals in intense high energy beams, in *Proc. XV Int. Conf. on High Energy Accelerators*, Hamburg (1992), pp. 173–175.
61. A. Taratin and S. Vorobiev, *Nucl. Instrum. Methods Phys. Res. B* **47**, 247 (1990).
62. S. Baker *et al.*, *Nucl. Instrum. Methods B* **90**, 119 (1994).
63. G. Smirnov *et al.*, *Nucl. Instrum. Methods Phys. Res. B* **309**, 141 (2013), http://cds.cern.ch/record/1709905.
64. S. Møller *et al.*, *Nucl. Instrum. Methods Phys. Res. B* **84**, 434 (1994), http://www.sciencedirect.com/science/article/pii/0168583X94953384.
65. C. Biino *et al.*, The influence of radiation damage on the deflection of high-energy beams in bent silicon crystals, Tech. Rep. CERN-SL-96-030-EA (1996), http://cds.cern.ch/record/308375.
66. F. Harden *et al.*, Hiradmat: A facility beyond the realms of materials testing, in *10th Int. Particle Accelerator Conf.* (*IPAC '19*), Melbourne, Australia, 19–24 May 2019 (JACOW Publishing, Geneva, 2019), pp. 4016–4019.
67. A. Lechner *et al.*, *Conf. Proc.* **C130512**, THPFI059 (2013), http://cds.cern.ch/record/1635963.
68. W. Scandale *et al.*, *Eur. Phys. J. C* **79**, 933 (2019), http://cds.cern.ch/record/2702843.
69. W. Scandale, A. D. Kovalenko and A. M. Taratin, *Nucl. Instrum. Methods Phys. Res. A* **848**, 166 (2017).

70. G. Hall *et al.*, *Nucl. Instrum. Methods Phys. Res. A* **924**, 394 (2019).
71. W. Scandale *et al.*, *J. Instrum.* **16**, P08015 (2021), https://cds.cern.ch/record/2778809.
72. O. S. Brüning, P. Collier, P. Lebrun, S. Myers, R. Ostojic, J. Poole and P. Proudlock, LHC Design Report, CERN Yellow Reports: Monographs, CERN, Geneva (2004), https://cds.cern.ch/record/782076.
73. D. Mirarchi *et al.*, *Eur. Phys. J. C* **77**, 424 (2017).
74. M. Butcher, A. Giustiniani, R. Losito and A. Masi, Controller design and verification for a rotational piezo-based actuator for accurate positioning applications in noisy environments, in *IECON 2015 — 41st Annual Conference of the IEEE Industrial Electronics Society* (2015), pp. 003887–003892.
75. R. W. Assmann *et al.*, The final collimation system for the LHC, LHC-PROJECT-Report-919, CERN-LHC-Project-Report-919 (2006) http://cds.cern.ch/record/972336.
76. R. Rossi, Experimental assessment of crystal collimation at the Large Hadron Collider, Ph.D. thesis, presented 26 Jan 2018, https://cds.cern.ch/record/2644175.
77. D. Mirarchi, Vol. 31 — Crystal collimation for LHC, Ph.D. thesis, Imperial College, London (2015), http://inspirehep.net/record/1429402/files/fulltext_U_6hB.pdf.
78. W. Scandale *et al.*, *Phys. Lett. B* **758**, 129 (2016).
79. S. Redaelli *et al.*, *Eur. Phys. J. C* **81**, 1 (2021).
80. R. Rossi *et al.*, Dechanneling population at extreme crystal bending with 6.5 TeV proton beam, unpublished (2019).
81. E. B. Holzer *et al.*, *Phys. Procedia* **37**, 2055 (2012), https://cds.cern.ch/record/2103398.
82. W. Hofle, Progress in transverse feedbacks and related diagnostics for hadron machines, Tech. Rep. CERN-ACC-2013-0193, CERN-ATS-2013-0193 (2013).
83. F. Schmidt, Sixtrack, User's Reference Manual, CERN, Geneva, Switzerland, Rep. CERN/SL/94-56-AP (1994).
84. Mad-X website: https://madx.web.cern.ch/madx/.
85. R. Rossi *et al.*, Crystal collimation cleaning measurements with 6.5 TeV protons in the LHC, unpublished (2019).
86. R. Rossi *et al.*, Crystal collimation cleaning performance with multi-TeV xenon ion beams, unpublished (2019).
87. M. D'Andrea *et al.*, Crystal collimation of 20 MJ heavy-ion beams at the HL-LHC, in *Proc. 12th Int. Particle Accelerator Conference* (2021), pp. 2644–2647, https://cds.cern.ch/record/2783802.
88. R. Rossi *et al.*, Status of crystal collimation studies at the LHC, in *8th Int. Particle Accelerator Conf.* (*IPAC'17*), Copenhagen, Denmark, 14–19 May, 2017 (JACOW, Geneva, 2017), pp. 84–87.
89. D. Mirarchi *et al.*, *Phys. Rev. Applied* **14**, 064066 (2020).
90. S. Abdel Khalek *et al.*, *J. Instrum.* **11**, P11013 (2016), arXiv:1609.00249, https://cds.cern.ch/record/2212402.
91. TOTEM Collab. (G. Anelli *et al.*), *J. Instrum.* **3**, S08007 (2008).
92. A. Taratin and S. Vorobiev, *Phys. Lett. A* **119**, 425 (1987).
93. V. Previtali, R. Assmann, S. Redaelli and I. Yazinin, Beam loss predictions for the UA9 crystal collimation experiment, in *Proceedings PAC09*, Vancouver, Canada (2009).
94. SixTrack Project website: http://sixtrack.web.cern.ch/SixTrack/.
95. S. Dabagov, *Nucl. Instrum. Methods Phys. Res. B* **355**, 1 (2015).

96. P. Schoofs, F. Cerutti, A. Ferrari and G. Smirnov, *Nucl. Instrum. Methods Phys. Res. B* **309**, 115 (2013).
97. E. Bagli *et al.*, *Eur. Phys. J. C* **74**, 2996 (2014).
98. E. Bagli and V. Guidi, *Nucl. Instrum. Methods Phys. Res. B* **309**, 124 (2013), http://www.sciencedirect.com/science/article/pii/S0168583X1300308X.
99. D. Mirarchi *et al.*, Improvements of the crystal routine for collimation studies, CERN-ACC-2014-0137 (2014), http://cds.cern.ch/record/1742258.
100. Y. A. Chesnokov, V. Maisheev and I. Yazynin, Volume capture and volume reflection of ultrarelativistic particles in bent single crystals, arXiv:0808.1486.
101. C. Ahdida *et al.*, *Front. Phys.* **9** (2022).
102. E. D. Courant and H. S. Snyder, *Ann. Phys.* **3**, 1 (1958).
103. M. Fjellstrom, Particle tracking in circular accelerators using the exact Hamiltonian in sixtrack, Ph.D. thesis, Lulea University (2013).
104. R. De Maria *et al.*, SixTrack Version 5: Status and new developments, in *Proc. 10th Int. Particle Accelerator Conference* (2019), pp. 3200–3203.
105. L. Schachinger and R. Talman, *Part. Accel.* **22**, 35 (1985).
106. W. Hardt, J. Jäger and D. Möhl, A general analytical expression for the chromaticity of accelerator rings, Tech. rep., CM-P00065010 (1982).
107. F. Ferroni *et al.*, *Nucl. Instrum. Methods A* **351**, 183 (1994).
108. R. A. J. Carrigan *et al.*, Extraction from TeV range accelerators using bent crystal channeling, Tech. Rep. FERMILAB-PUB-94-056, FERMILAB, Batavia, IL (1994), http://cds.cern.ch/record/422536.
109. Z. Tang, Silicon crystal under bending, Tech. Rep. FERMILAB-TM-1827, Fermi National Accelerator Lab., Batavia, IL (USA) (1993).
110. J. T. Klem and U. Mikkelsen, Study of the crystal surface and bending for the crystal extraction experiment, Tech. Rep. SL-MD-Note-171, CERN, Geneva (1995), https://cds.cern.ch/record/702955.
111. J. T. Klem, Proton extraction from a high-energy beam with bent crystals, CERN-THESIS-98-018, presented on 21 Aug 1998, http://cds.cern.ch/record/366497.
112. A. Taratin *et al.*, *Nucl. Instrum. Methods Phys. Res. B* **58**, 103 (1991).
113. A. G. Afonin *et al.*, High-efficiency multipass extraction of 70 GeV protons from accelerator with a short bent crystal, Tech. Rep. IHEP-98-34, Protvino Inst. High Energy Physics, Protvino (1998), http://cds.cern.ch/record/412014.
114. E. F. Troyanov *et al.*, Progress in study of efficient crystal extraction and collimation at IHEP, arXiv:hep-ex/0111042, http://cds.cern.ch/record/555908.
115. A. Mazzolari *et al.*, Fabrication of crystals for channeling of particles in accelerators, in *Charged and Neutral Particles Channeling Phenomena*: *Channeling 2008* (World Scientific, 2010), pp. 180–186.
116. W. I. Kordonski, Magnetorheological fluid-based high precision finishing technology, in *Magnetorheology*: *Advances and Applications* (The Royal Society of Chemistry, 2014), pp. 261–277.
117. G. Germogli *et al.*, *Nucl. Instrum. Methods Phys. Res. B* **402**, 308 (2017).
118. Yu. M. Ivanov, Crystal technology at PNPI (2017), https://indico.cern.ch/event/752062/contributions/3114840/attachments/1737492/2810742/Crystal_technology_at_PNPI.pdf.
119. V. Guidi and A. Mazzolari, Crystal technology at INFN (2017), https://indico.cern.ch/event/752062/contributions/3114838/attachments/1737441/2810616/0_HL-LHC-19-10-2018_mazzolari.pdf.
120. O. Sumbaev, *Sov. Phys. JETP* **5**, 1042 (1957).

121. O. Sumbaev, *Sov. Phys. JETP* **27**, 724 (1968).
122. V. Samsonov and E. Lapin, On some possibilities and peculiarities of a curved crystal use in crystal diffraction instruments, Tech. Rep. EuCARD-REP-2013-002, lIYaF an SSSR preprint No. 587 (1980).
123. Yu. M. Ivanov *et al.*, *Phys. Rev. Lett.* **97**, 144801 (2006).
124. W. Scandale *et al.*, *Nucl. Instrum. Methods Phys. Res. B* **338**, 108 (2014).
125. V. Biryukov, V. I. Kotov and Y. A. Chesnokov, *Phys. Usp.* **37**, 937 (1994).
126. A. Taratin, *Phys. Part. Nucl.* **29**, 437 (1998).
127. G. Moliere, *Z. Naturforschr. A* **2**, 133 (1947).
128. Y. L. Pivovarov and S. Vorob'ev, *Dokl. Akad. Nauk SSSR* **256**, 837 (1981).
129. T. Waho, *Phys. Rev. B* **14**, 4830 (1976).
130. M. Kitagawa and Y. H. Ohtsuki, *Phys. Rev. B* **8**, 3117 (1973).
131. A. Taratin, *Nucl. Instrum. Methods Phys. Res. B* **119**, 156 (1996).
132. V. M. Biryukov, Y. A. Chesnokov and V. I. Kotov, *Crystal Channeling and its Application at High-Energy Accelerators* (Springer Science & Business Media, 2013).
133. A. M. Taratin and S. A. Vorobiev, *Phys. Stat. Solidi B* **107**, 521 (1981).
134. M. Bavizhev, V. Biryukov, Y. G. Gavrilov and D. McNeil, *Sov. Phys. Tech. Phys.* **36**, 203 (1991).
135. V. Biryukov, Y. Chesnokov, N. Galyaev, V. Kotov, S. Tsarik and V. Zapolsky, *Nucl. Instrum. Methods Phys. Res. B* **73**, 153 (1993), http://www.sciencedirect.com/science/article/pii/0168583X9395729O.
136. A. Taratin and S. Vorobiev, *Nucl. Instrum. Methods Phys. Res. B* **26**, 512 (1987).